Towards the geometrical structure of supported size-selected clusters and nanoparticles by X-ray scattering

Dissertation
zur Erlangung des Doktorgrades
an der Fakultät für Mathematik, Informatik und Naturwissenschaften
Fachbereich Physik
der Universität Hamburg

vorgelegt von
Deniza Chekrygina
aus Tscheboksary

Hamburg
2018

Gutachter/innen der Dissertation:	PD Dr. Michael Martins Prof. Dr. Andreas Stierle
Zusammensetzung der Prüfungskommission:	PD Dr. Michael Martins Prof. Dr. Andreas Stierle Prof. Dr. Daniela Pfannkuche Prof. Dr .Gerhard Grübel Prof. Dr. Michael A. Rübhausen
Vorsitzende/r der Prüfungskommission:	Prof. Dr. Michael A. Rübhausen
Datum der Disputation:	18.01.2019
Vorsitzender Fach-Promotionsausschusses PHYSIK:	Prof. Dr. Wolfgang Hansen
Leiter des Fachbereichs PHYSIK:	Prof. Dr. Michael Potthoff
Dekan der Fakultät MIN:	Prof. Dr. Heinrich Graener

Abstract

Nanostructures are known to be promising candidates for investigation due to their unique size-dependent properties. In particular, nanoclusters of noble metals have generated a lot of interest from the scientific community, as well as from industry, due to their possible applications in medicine, ecology, and nanoelectronics. The exhibited physical and chemical properties of such clusters are strongly influenced by their size and morphology, therefore the investigation of the geometrical structure is of high importance.

This thesis describes the investigation of the geometrical structure of deposited bimetallic Au/Ag clusters (consisting of several thousand atoms per cluster) and ultrasmall size-selected Au_n clusters (n=5, 7, 9, 11). Both of these systems were studied experimentally, using as the main method Grazing Incidence Small-Angle X-ray Scattering (GISAXS) at the beamline P03, PETRA III, DESY.

Bimetallic clusters of Au/Ag were investigated in real time and compared with pure metals in similar conditions demonstrated differences from both. At 10 nm effective thickness the radius of the bimetallic clusters was shown to be close to that of Au, while the shape tends to flatten similarly to Ag. The percolation threshold was determined to be 3 nm, which was at a much earlier stage than of pure metals. The bimetallic clusters demonstrate a higher reflectance at the 400-800 nm wavelength range than pure materials, which shows that tuning the material ratio in a compound material can exhibit useful properties for possible applications.

Ultrasmall size-selected Au_n clusters were prepared using a soft-landing scheme and capped with a protective Al layer, which allowed for *ex situ* investigation by GISAXS in combination with X-ray Fluorescence (XRF). Radii and possible shapes of Au_9 and Au_{11} could be estimated using a model-based approach together with X-ray experimental techniques.

Kurzfassung

Nanostrukturierte Materialien gelten aufgrund ihrer einzigartigen, größenabhängigen Eigenschaften als vielversprechende Objekte in der Grundlagenforschung. Insbesondere Nanocluster von Edelmetallen haben aufgrund ihrer Anwendungsmöglichkeiten in der Medizin, Ökologie und Nanoelektronik großes Interesse in der Wissenschaft und in der Industrie geweckt. Die spezifischen physikalischen und chemischen Eigenschaften von Nanoclustern werden stark von ihrer Größe und Morphologie beeinflusst, daher ist insbesondere die Untersuchung der geometrischen Struktur von großer Bedeutung.

Die vorliegende Arbeit beschreibt die Untersuchung der geometrischen Struktur von abgeschiedenen bimetallischen Au/Ag-Clustern (bestehend aus mehreren tausend Atomen pro Cluster) und ultrakleinen Au_n-Clustern (n=5, 7, 9, 11). Beide Systeme wurden experimentell untersucht, wobei als Hauptmethode die Grazing Incidence Small-Angle X-ray Scattering (GISAXS) am Strahlrohr P03, PETRA III, DESY verwendet wurde.

Die geometriche Struktur von bimetallische Cluster von Au/Ag wurden im Vergleich zu reinen Metallen in Echtzeit unter ähnlichen Bedingungen untersucht und zeigten speifische Unterschiede. Bei einer effektiven Dicke von 10nm zeigte sich, dass der Radius der bimetallischen Cluster nahe an dem von Au liegt, während die Form dazu neigt, sich ähnlich wie bei Ag zu verflachen. Die Perkolationsschwelle wurde auf 3nm bestimmt.

Diese Schwelle liegt bei kleineren Abständen als bei reinen Metallen. Die bimetallischen Cluster weisen im Wellenlängenbereich von 400-800 nm eine höhere Reflexion auf als reine Materialien. Dies zeigt, dass über die Wahl des Materialverhältnisses in einem Verbundmaterial seine Eigenschaften für mögliche Anwendungen in einem bestimmten Rahmen gewählt werden können.

Au_n Nanocluster mit definierter Größe n wurden nach einem Soft-Landing-Schema hergestellt und mit einer schützenden Al-Schicht versehen, was eine *Ex situ*-Untersuchung durch GISAXS in Kombination mit Röntgenfluoreszenz (XRF) ermöglichte. Radien und mögliche Formen von Au_9 und Au_{11} konnten mit einem modellbasierten Ansatz in Verbindung mit röntgentechnischen Experimentiertechniken bestimmt werden.

Acknowledgements

I am very grateful for the opportunity to express my gratitude to everyone who was providing a lot of support during my PhD studies. Unfortunately, it was impossible to list everything and everybody I am appreciative for.

I would like to acknowledge my supervisors PD Dr. Michael Martins and Prof. Dr. Wilfried Wurth from Hamburg University for their guidance and support during my PhD studies. I would also like to acknowledge my former supervisors from the Institute of Crystallography of Russian Academy of Science Prof. Dr. Vladimir Volkov and Prof. Dr. Eleonora Shtykova, who inspired me to stay in science and their encouragement for starting the study abroad. I am grateful to the PIER Helmholtz Graduate School, which helped me and supported in developing new skills important for a researcher.

I am grateful for the help of my research group AG Wurth with my studies in the last years, especially Dr. Ivan Baev, Dr. Torbeen Beeck, Fridtjof Kielgast, and Dr. Lukas Wenthaus for their help with measurements and sample preparation, and Karolin Mertens, Dr. Steffen Palutke and Marlis Foelck for their support. I also want to acknowledge beamline scientists from P03 and P04 (PETRA III, DESY), the brilliant work of whom allowed for making these complicated studies. Especially, Prof. Dr. Stephan Roth, Dr. Matthias Schwartzkopf, Jan Rubeck, Dr. Wiebke Ohm and Dr. Anton Davydok.

I was very lucky to get a lot of help and encouragement during these years from Dr. André Rothkirch and Dr. Stephan Klumpp. I was happy to work with Dr. Pallavi Pandit, who not only became my close friend here but also gave a lot of support.

I am grateful for the immense support from my parents Igor Chekrygin, Svetlana Chekrygina and reinforced encouragement of my grandmother Dr. Anastasia Pavlova. My husband Dr. Graham Appleby gave me a lot of emotional and scientific support as well as proofread my thesis and other scientific papers. I also appreciate input of Maxwell and Nuala for always being there for me.

Contents

List of Figures

List of Tables

List of Abbreviations

The following is a list of repeatedly used symbols and their definitions. Less frequent terms are defined in the text where required.

2D	Two dimensional
3D	Three dimensional
GISAXS	Grazing Incidence Small-Angle X-ray Scattering
GIWAXS	Grazing Incidence Wide-Angle X-ray Scattering
ML	Monolayer
PCA	Principal Component Analysis
UV/Vis	Ultra-Violet Visible Spectroscopy
UHV	Ultra High Vacuum
XRF	X-ray Fluorescence spectroscopy
XRR	X-ray Reflectivity
δ	Effective thickness
D	Interparticle distance
$\mathbf{q}$	Momentum transfer vector
R	Radius of a nanoparticle
Ref	Reflectance

Introduction

The prospering field of nanotechnology has become an innovation motor in science and industry in recent decades. The 2016 Nobel Prize in chemistry was awarded to J-P. Sauvage, Sir J. F. Stoddart and B. L. Feringa for their design and production of molecular nanomachines. In medicine, nanoscale technologies also have a great impact, which is now utilised on a par with micro-technologies in drug delivery, tissue engineering, and pharmaceutical development/testing[1]. The positive impact nanotechnology has on the development of society is actively discussed in scientific literature[2]. This demonstrates the importance of research in the area of nanotechnologies, which steadily increases with time.

This was reflected in the European Commission's latest Horizon 2020 Work Program, which stated that the EC would provide 1.5 billion euros to funding nanotechnological research during 2018 – 2020[3]. Several areas in nanoscience are of the most importance for the European Union, for example, nano-enabled compound materials, bio- and medical-nanotechnologies and environmental applications. In the latter, catalytical properties of nanomaterials will continue to play an important role.

The noble metals Au, Ag, and Cu are known for their unique qualities in the nanoscale regime[4]. Between them, these copper subgroup metals are of great interest due to their fascinating properties[5–7]. This work describes the production of and characterisation of both Au and Ag nanoparticles discussed, which are proved to be extremely appealing for research, due to their possible present and future applications in medicine (Ag[8–10], Au[11–13]). They are also known for their optical properties, therefore their application in solar cells and sensors seems very promising[14,15]. Even more control over the catalytical and optical properties can be achieved by using bimetallic nanoparticles of Au and Ag, which is done by varying their ratio[16,17]. For example, tuning of the surface plasmon resonance was demonstrated on the example of Au/Ag nanoclusters[18]. There is still a lack of understanding of the chemical and physical processes which take place during production of these systems. Consequently, real-time investigation of Au/Ag geometrical structures can help to get better knowledge and, thus, better control over properties and fabrication.

Another interesting question is the morphology and properties of noble metals in the sub-nanometer regime. Deposited small gold clusters (<5 nm) were reported to be promising candidates as catalytic agents in chemical industries, environmental protection etc., since their activity increases with the decrease of the size[19]. For such systems geometrical structure is directly connected to the properties and one atom difference can affect the behaviour[20]. Physical[11,12,21,22] and chemical[20,23,24] properties can be tailored up to some extent by controlling their size and geometrical structure. Studies have shown cluster size effects on the catalytic activity[25–28], plasmonic properties[29–32] and magnetic properties[33]. This work describes ultrasmall gold clusters which are known to be potential catalytic agents, with catalytic activity

highly dependent on the number of atoms in a cluster. For example, Au_8 on an oxide surface is much more reactive in CO combustion than clusters with seven atoms or less, while Au_{11} has the same reactivity[34]. At the same time, they are both more reactive than Au_9 and Au_{10}. Furthermore, in the reaction of bromination of 1,4-dimethoxybenzene, Au_5 and Au_7 on TiO_2 are more reactive than Au_8 and Au_9[23]. To understand the process of size-dependent reactivity in such catalysts, it is important to know the geometrical structure of ultrasmall Au clusters deposited on oxide surfaces.

The aim of this work is to investigate the geometrical structure of two different gold nanosystems deposited on Si/SiO_2. The first system is Au/Ag bimetallic clusters during deposition in the radio frequency (RF) chamber. The second system is ultrasmall size-selected Au_n clusters (n=5, 7, 9, 11) and adatoms, synthesised via soft-landing deposition by ion source. Both of the aforementioned systems impose certain restrictions to the possible investigation method. Since they were both deposited, surface sensitivity was important. Another constraint was the low amount of the material (in case of ultrasmall clusters- 10% mono layer), which implied necessity of synchrotron radiation. Ultrasmall clusters had an Al protective capping layer, hence penetration ability was required. The experimental technique which satisfies each of these conditions is Grazing Incidence Small-Angle X-ray Scattering (GISAXS) using microfocused synchrotron radiation. In grazing incidence geometry the X-ray penetration depth is restricted to the surface layer which is extremely important for investigation of the nanostructure on the surface[35]. GISAXS provides the physical properties averaged over the whole sample. It can give complete structural information such as size, shape and interparticle distances. Additionally, this method provides good geometrical resolution in real-time investigation of growing nanostructures[31,36].

Chapter 1 of this thesis introduces fundamental aspects about the two cluster types studied and the sample preparation methods. In Chapter 2 detailed descriptions of the experimental setups for sample preparation, sample characterisation as well as a description of the analytical methods is provided. Experimental results for each system studied and discussions are presented in Chapter 3. Finally the main conclusions are presented, and an outlook for future development is given.

1. Fundamental aspects

This chapter contains a literature review introducing fundamentals most relevant to the research. Firstly, nanoscience and cluster concept are discussed. Secondly, properties of interest of nanosized gold, silver and their mixture are depicted. In particular, preparation methods, properties and predicted structures of ultrasmall size-selected gold clusters are discussed. Thirdly, an overview of the most popular cluster preparation methods and possible investigation approaches is provided.

This work concentrates on the morphology of two groups of samples: mixed deposited Au/Ag clusters and ultrasmall Au_n (n=5, 7, 9, 11) size-selected clusters. To demonstrate that such clusters, when properly understood, will be of use in many future applications, properties of such systems are also addressed.

In this work, several most important reviews and books that are helpful for understanding of the phenomena and methods were used. Discussion about the properties and production of metallic clusters and nanolayers was influenced by O. Milton[37], P. Jensen[38] and W. de Heer[4]. The part about the X-ray methods of investigation and synchrotron radiation was affected by G.V. Fetisov[39]. The theory and analysis routines of the main method of investigation (GISAXS) was inspired by P. Müller-Buschbaum[35], L. A. Feigin and D. I. Svergun.[40] and G. Santoro and Sh. Yu[36].

1.1. Nanoscience

The notion "nanoscience" embraces investigation, production and manipulation of matter on the nanoscale (10^{-9} m). This is a multidisciplinary field where physics, chemistry, biology and engineering are interconnected. Although some nanoscience phenomena were already observed several centuries ago, systematic and extensive research in this field started after 1959. Then Richard Feynman predicted that it will be possible to manipulate and control things of infinitesimal size. During the 1980s, when scanning tunnelling and atomic force microscopes were invented it accelerated the development of nanoscience. Presently almost everything that was predicted by Feynman came true, but there is still "plenty of room at the bottom"[41].

Clusters

Cluster by a common definition means objects positioned or occurring closely together. In nanoscience, this term is used to refer to a nanosized ensemble of several atoms bound together, ranging from three to several hundreds of thousands.

Clusters can be considered an intermediate stage between single atoms and bulk materials. Their production and investigation is a key topic of nanoscience, since they exhibit properties different from

both the material in bulk and single atoms[42]. There exist plenty of possible applications of using clusters for example in industrial catalysis or nanoelectronics[43,44] as well as in medical applications such as cancer diagnostics and therapy[45,13]. Indeed, all the possible applications are not exhausted by the ones mentioned above, but the potential is too overwhelming to be fully described here.

1.1.1. Au nanoclusters

Gold has been a well-known metal since at least the 4th century B.C[46]. This noble metal is valued not only for the economic versatility but also for the unique physical and chemical properties. For many centuries it has been a subject of scrutiny for possible unique applications, and today the interest is its characteristics in the nanoscale regime and smaller. The development of modern experimental capabilities allows this metal to be chemically or physically synthesised from single atoms. This opens a wide range of possibilities to control the size of the system from a few to many thousands of atoms. It is now possible to detect and investigate properties of gold in the gas phase, but for future technological applications, it is crucial to deposit or embed such structures into solid substrates. Since the geometrical structure interrelates with chemical and physical properties, this work is primarily concentrated on morphological analysis. This work focuses on the geometry of embedded mass-selected ultrasmall Au_n clusters ($n<12$) and of larger Au_m clusters ($m>100$) compared to bimetallic Au/Ag.

Basic properties of nanostructured gold.

One of the earliest uses of nanostructured gold dates back to around the 4th century C.E. when the famous Lycurgus cup was created. From the scientific point of view however only in the middle of the 19th century so called gold "colloids" were studied[46] when they were chemically generated by Michael Faraday[47]. His main follower was Wilhelm Ostwald who developed the science of colloids[48] by stating that particles in the nanometer regime demonstrate novel properties which differ from the bulk[46] (here it is important to point out that with the development of nanotechnology, the term "colloid" was replaced with "nanoparticle" or "nanocluster"). Later, investigations also showed significant changes in gold properties, depending on the size in the nanometer range, as was shown by Castro *et al* where he demonstrated the relationship between the melting point and the particle size[49]. Reviews of Schwerdtfeger and Pyykkö described divergent relativistic effects of pure gold from other Group 11 metals[28,50] as well as of its mixed compounds[51]. Gold is also well known for its quantum size effects, the most famous of which is surface plasmon resonance. This gives the red colour in glass to the Lycurgus cup, in nanoporous alumina membrane[52] and changes the colour from violet to orange on the surface of polystyrene during deposition[32].

1.1.2. Ag nanoclusters

Similarly to gold, silver is widely used since ancient times and not only as a form of currency. Contrary to gold, silver has been valued for its medical rather than optical properties. Ancient Greeks, Romans and Persians used silver to protect food from spoiling and to control infections. Silver has been

investigated in bulk form mainly because of its antibacterial properties, and more recently nanoparticles and nanoclusters of Ag became of great interest for their toxicity, surface plasmon resonance and electrical resistance[53]. Therefore, the production methods of nanosized Ag are also of significant interest[10,53].

Basic properties of nanostructured silver.

Historically, the primary interest in silver has been in its medical application, and now, being nanosized silver is still of great interest to modern science as antibacterial, antifungal, antiviral, anti-inflammatory, anti-angiogenic, and anti-cancer agents[10]. Conversely, silver nanoclusters have been reported hazardous not only for the wildlife but for humans, when mishandled[9]. Their shape and size can dramatically affect the physical and chemical properties, for example the toxic potential of silver clusters is inversely dependent on their size[9]. Furthermore, the method of preparation plays a role in the properties of silver nanoclusters. This applies to optical features too, for example there is a different maximum of surface plasmon resonance, in nanoclusters prepared by glucose reduction rather than by NaOH reduction[53]. In general, silver nanoclusters can be used as real-time sensors, as plasmonic solar cells, as building blocks for light-energy guiding devices, and as metamaterials with unique optical properties[15]. For these applications, the stability of the system is extremely important and can depend on the preparation method. The physical method of preparation of such nanoclusters was reported to be five times more stable than the chemical method[15]. Another interesting area of research is the thermal behaviour of silver nanoclusters. While at 100 °C the thermal properties of nanoparticles and bulk materials do not differ, at 150 – 200 °C the size of Ag nanoparticles of 3 to 6 nm size progressively increases[53]

1.1.3. Bimetallic Au/Ag clusters

Bimetallic nanostructures have become of a great interest in the last two decades, due to their fascinating qualities allowing the tuning physical and chemical properties in a system, for example by controlling the ratio of one material to another. This has been made possible by the development of cluster sources and chemical synthesis. There exist numerous methods to produce bimetallic clusters, which can be divided in two groups of regular cluster production: chemico-biological synthesis[54,55,56,17,57] and physical methods of deposition [58–60].

Recently most attention in this field is focussed on the optical properties and structure of Au/Ag[57,61–64]. A good example of Au/Ag versatility is shown in the work of Faupel's group, where they demonstrated how the plasmon resonance frequency was tuned by changing the material composition[18]. The performance of polymer solar cells was enhanced by adding Au/Ag nanoparticles[65]. It was also reported that optical constants of the Au/Ag alloy (at a 50% Au/Ag mole fraction) differ from the arithmetic average of the refractive indices of Au and Ag, especially in near-IR wavelength region, and scattering is reduced (light enhancement was also increased) at near-IR wavelengths[66]. One of the interesting applications of the optical properties of Au/Ag nanoparticles is the sensing of chirality and circular

dichroism of enantiomers[61]. Although, all the above mentioned studies concentrate on the optical properties, other physical and chemical properties can be of interest. The electronic and geometrical structures of ultrasmall bimetallic Au/Ag clusters experience changes depending on the increased concentration of one of the metals, for example binding energy decreases with a lower fraction of Au while the formation energy increases[67]. Nanoelectronics can vary the performance of pure Au by adding Cu to increase strength of contacts or when adding Ag – maximum interatomic distances[68]. Bimetallic nanoparticles can also be useful as electrocatalysts for direct methanol fuel cells [56].

Bimetallic nanoparticles can form various structures depending on the method of preparation, conditions during the experiment (temperature, vacuum, pH), and the relative amount of material. It was also proposed by Fan *et al* that the atomic radius, bond dissociation energy, electronegativity of the core and shell metals, and growth rate could play key roles in determining the growth mode[69]. In a recent study of clusters prepared by laser ablation it was shown that the preferred structure of bimetallic clusters mostly depends on their composition[60]. Liao *et al* demonstrated that the minority element in Au/Ag clusters prefers core position, while the majority element is located in the shell. When having equal concentrations in $Au_{0.5}/Ag_{0.5}$ they tend to intermix. However, it was also reported that that the structures can be more complicated, forming Au/Ag Janus core and a Ag shell. This development in initially fully and homogeneously alloyed Au/Ag happened after a period of time due to oxidation[70]. For the cases when the structure was initially a core-shell due to the higher fraction of either Au or Ag, samples with a thick shell of Au showed the best long-term stability[71]. It was also confirmed that even 25% addition of Au to Ag increases the system stability against oxidation[66]. It has been found that when using chemical methods it is easier to create more complicated shapes of Au/Ag, such rings or hollow core-shell structures[72], nanoshuttles with tips[73], nanocubes[74] or Janus nanoparticles[75]. However, chemically prepared structures can be much less stable than of a physically prepared structure, as was shown on the example of Ag nanoclusters[15].

It is also of interest that the shape of annealed clusters, even at moderate temperatures below melting temperature of Au and Ag, results in the formation of more spherical Au/Ag nanoparticles[76]. Higher temperatures (300 °C) during deposition also makes local surface plasmon resonance more pronounced than when it occurs at room temperature[77].

In the physical methods of Au/Ag cluster preparation, one may install one[62] or two targets foreseen for deposition on a substrate inside a sputter chamber, as proposed by Döhrmann *et al*[78]. The present work is concentrated on the latter method due to the simpler and better control over the ratio of Au and Ag and also the possibility of using the exactly the targets during the whole experiment. Overall, previous works show that the detailed *in situ* study of bimetallic clusters in comparison with pure is of high importance.

1.1.4. Ultrasmall size-selected clusters.

Currently, it is well known that nanoclusters (1 – 100 nm) are an intermediate form between a single atom and bulk material. There properties usually scale roughly with their size. For small clusters with the radius of less than 5 nm interesting effects can be observed. It was found by Haruta that the catalytic activity of gold clusters of size less than 5 nm increases with a decrease in size[19]. It was also confirmed that there is an increased reactivity of low coordinated gold atoms when the size is less than 3– 5 nm[79]. The geometrical and electronic structure depends strongly on the cluster size. The charge or the neutrality of a cluster also has an impact on its shape, which is especially noticeable in the example of ultrasmall clusters[6,28,80]. Generally, not only chemical[23,20,24] but physical[12,21,11,22] properties of ultrasmall clusters can be tailored, up to some extent, by controlling their size and geometrical structure. There exists a particular interest in catalytic activity[25–28,81] of clusters, but plasmonic[29–32,82] and magnetic[33] properties are also strenuously being studied. By means of XMCD it was found that both spin and orbital moments depend on the quantity of atoms in the system[33]. In the case of ultrasmall clusters "every atom counts"[23,20] and for example, clusters consisting of eight atoms can exhibit significantly different properties (e.g. catalytic) than those with nine. The reason for this behaviour is that quantum size effects start to dominate the properties of the clusters. This might open completely new properties[83,14,84,44] of the clusters depending on their size, however, this implies also that a precise size selection is mandatory[20]. Size selected gold clusters can be also used for the synthesis of nanostructures, for example as an effective catalyst in synthesis of nanostructures, such as ZnO nanowires[85]. Such clusters were also proven to be a promising candidate in environmental applications, for example as sensors for toxic chemicals[14].

Similarly to the bimetallic clusters mentioned in Section 3.1.3, ultrasmall clusters such as gold (Au_n) ($3 < n < 20$) can be prepared by chemical synthesis[86,87,45] or by physical methods[88,89]. Due to with the difficult nature of preparation of size-selected gold clusters, their synthesis is discussed more thouroughly in the following. Chemical preparation of size-selected clusters usually employs thiolate or phosphine. Using chemical agents for stabilisation gives the opportunity to investigate larger size-selected clusters[44] as well as ultrasmall ones[90,91,86,87]. One of the more popular production methods is to use phosphate ligand to obtain stabilised $Au_9(PPh_3)_8(NO_3)_3$ as described by Wen *et al.*[92] This has proven to be more efficient and resulted in reduced structural distortion, compared the use of thiolates, as reviewed by Johnson and Laskin[93]. Phosphine preparation also allows relatively good control of the shape, which was demonstrated by Zhang *et al*. when they prepared heart-shaped Au_8 and open-icosahedral Au_{13}[90]. In all cases, the synthesis is usually followed by the process of deposition and drying[94], which can further affect the configuration of the clusters obtained.

Physical synthesis methods usually involve the use of an ion (RF) source[95,80] or a magnetron sputter source[96,97]. In both of these methods, a beam of atoms and self-assembled clusters is created after

bombarding the metal target with gas ions. Being a bottom-up method, this is highly controllable due to the tuneable deposition rate, and the clusters produced are initially in their most natural conformation[33,98]. Afterwards size-selection can be carried out, if clusters are charged as a result of the production process, or by placing an ioniser in the beam. Charging the clusters enables a number of techniques to select them by their mass over charge ratio[26]: RF quadrupole, Wien filter, cyclotron resonance, time-of-flight mass spectrometer, pulsed field mass selector etc. In the case of neutral clusters, a velocity selector can be applied[26].

1.1.4.1. Structures of Au ultrasmall clusters, predicted theoretically (n≤11).

Until now a significant amount of theoretical investigation has been carried out on ultrasmall clusters, especially on the noble metals. Due to relativistic effects, gold is the interesting object for theoretical investigation , and is extensively discussed in the reviews by Pyykko[28] and Schwerdtfeger[50,51]. Although as exciting as this is, the present work concentrates mainly on the geometrical structure of ultrasmall clusters. The usual approach to predict possible conformations of ultrasmall clusters depending on charge and amount of atoms in a cluster is density functional theory (DFT)[28,99–102,80,103]. This method determines properties of the whole system as a function of the electron density; therefore when solving many-body problem it replaces electron wave function and the corresponding Schrödinger equation by electron density. Simulations made with DFT show that charged clusters have a different structure than neutral clusters, and also anions differ from cations[104]. One of the most prominent dissimilarities is in the 2D transition which happens at bigger sizes of anions than cations. Figure 1 shows which configurations gold anions, cations and neutral clusters of sizes 5,7,9, and 11 are expected to have in the gas phase [6].

Theory shows that the fascinating 2D → 3D transition can be observed on the example of neutral Au_{11} cluster, for odd-numbered clusters[6]. At the same time, the calculated lowest-energy structures show that the smallest gold clusters are planar and a transition to a 3D structure takes place at a size of seven atoms[100].

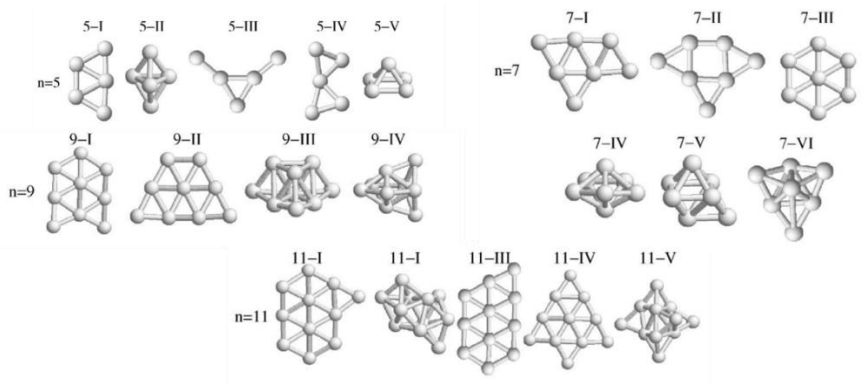

Figure 1: Sketch [6]. Equilibrium geometries of lowest energy isomers of anionic, cationic and neutral Au_n (n=5, 7, 9, 11) in the gas phase, predicted theoretically.

In the case of Au_9, calculations show that such clusters may form a planar quasi two-dimensional (2D) structure as well as a three-dimensional (3D) structure[28,83]. In one recent publication, Au_9 occurs in both conformations[87] for clusters prepared by the chemical route and stabilised with ligands. This behaviour was also observed in a ligand-free cation[105] in the gas phase.

1.2. Cluster preparation methods.

A large variety of preparation methods currently exists; however in this work only preparation methods for metal clusters are discussed. Methods can be categorised as chemical or physical, and a different classification of top-down and bottom-up approaches can be applied. When top-down is used, nanostructures are created from the bulk, e.g. using chemical or lithography etching. When bottom-up approach is applied–the building block is a single atom or a cluster, therefore in most of the cases it gives precision and control over the resulting structure. Although both chemical and physical methods can belong to either top-down or bottom-up approach, chemical methods typically classify as bottom-up. One of the most common chemical approaches is a salt-reduction technique, typically used with ligand stabilisation for production of metal clusters[106,46]. There are also such whimsical methods as using bacteria for the synthesis of silver nanostructures[107] or plant extracts for bimetallic particles[17].

Physical bottom–up methods typically employ high or ultrahigh vacuum, and high energies or temperatures applied to the metal targets[26]. Different types of cluster formation sources can be used: seeded supersonic nozzle sources, laser vaporisation sources, gas-aggregation sources, pulsed-arc cluster-ion sources, ion sputtering sources, liquid-metal ion sources[4]. All of these are able to produce beams of clusters or atoms, which can be investigated prior to the deposition (in the gas phase) or after deposition.

Sputtering is a process by which atoms are removed from a surface and it usually means that the energetic particle (usually an ion) transfers momentum to the target material. This creates a displacement on its surface and if the target atoms have enough energy they can be ejected. From this it follows that the yield depends on the relative masses of target atom and ion due to the momentum transfer process[108]. Usually as a source of ions, Ar or other noble gases are used and they are ionised by applying a potential to the target. The substrate is negatively charged, so the plasma is created due to the momentum transfer from Ar and atoms from the target surface are deposited on the substrate where they lose their charge.

1.2.1. Classical atomic growth models

Deposited clusters can form nanolayers or islands. The formation depends on the amount of the material, substrate and the conditions during the deposition.

Basic elementary processes of the supported cluster growth are shown in Figure 2 and Figure 3. All of the described processes like diffusion, adsorption and nucleation are presented for the case of an ideally smooth surface, however defects can alter it. The temperature also influences the probability of nucleation versus coalescence - whereas higher temperatures accelerate the coalescence, lower temperatures makes nucleation more preferable. In this elementary model, Jensen[38] considers nucleation occurring only on the surface, although nucleation can happen prior to the deposition[60].

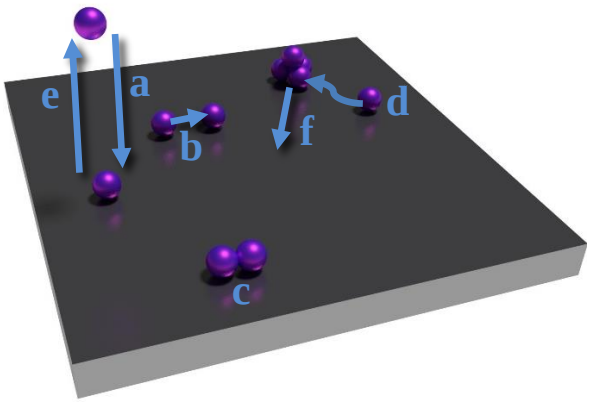

Figure 2: Main elementary processes for the growth of films in cluster deposition. a) adsorption of a cluster by deposition; b) and d) diffusion of the isolated clusters on the substrate; c) formation of an island from two clusters by nucleation; d) growth of a supported island by incorporation of a diffusing cluster; e) evaporation of an adsorbed cluster; f) island diffusion. Redrawn from [38]

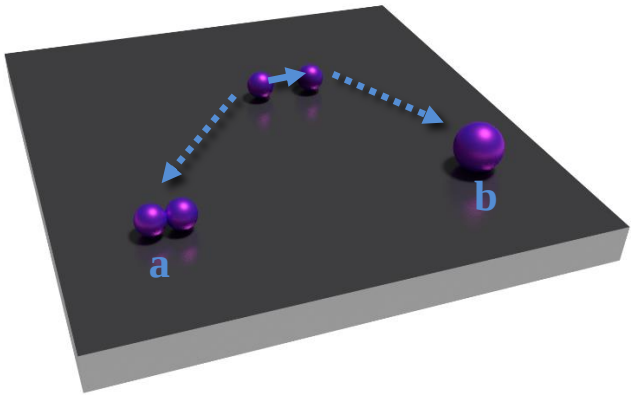

Figure 3: Redrawn from [38]. Possible interaction of two clusters touching the surface. a) Nucleation; b) total coalescence.

After coalescence or nucleation occurs, the next stage can be a thin film formation. There are three main models describing this process: Volmer-Weber, Frank-van der Merwe and Stranski-Krastanov.

The stages of the former are presented in Figure 4. The Volmer-Weber model can also be called island growth. When clusters are nucleated on the substrate, they start to grow in three dimensions. This happens when the binding between clusters (atoms) is higher than with the substrate[37].

The Frank-van der Merwe model (or the layer model) is illustrated in Figure 5. It depicts the case when atoms or clusters bind stronger to the substrate and the growth only takes place in two dimensions.

The third case initially looks similar to the layer growth, but later switches to the island growth. This growth mode was suggested by Stranski and Krastanov. It is considered to be a mixture of the two models as sketched in Figure 6.

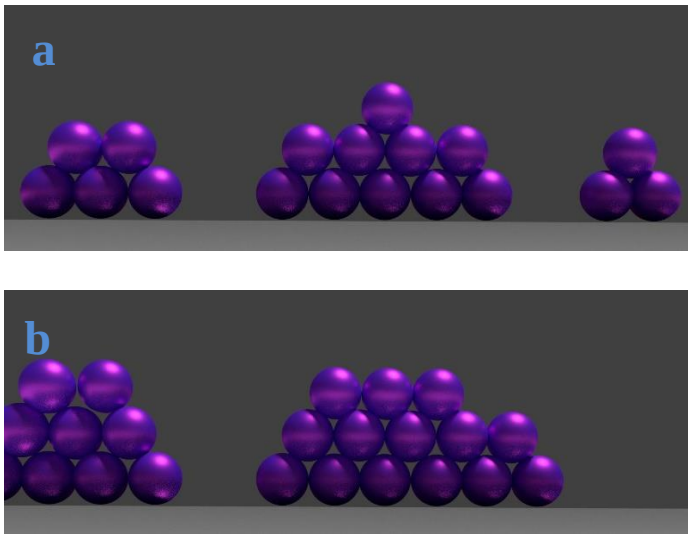

Figure 4: Volmer-Weber growth mode. a) Surface with deposited material < 1ML (monolayer) thickness. b) Surface with deposited material > than 1 ML.

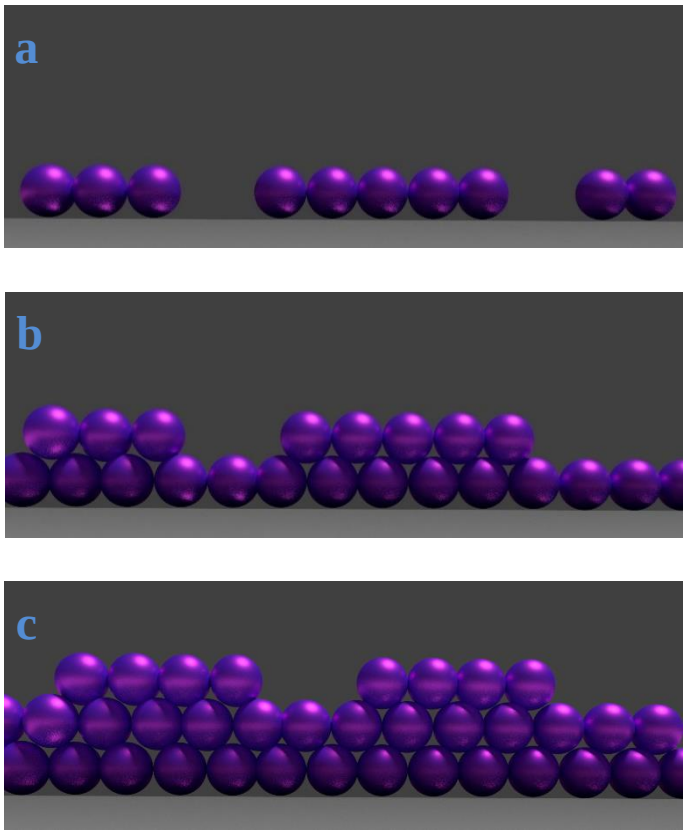

Figure 5: Frank van Merve growth mode. a) Surface with deposited material < 1ML (monolayer) thickness. (b) Surface with deposited material > than 1 ML. c) Surface with deposited material » than 1 ML.

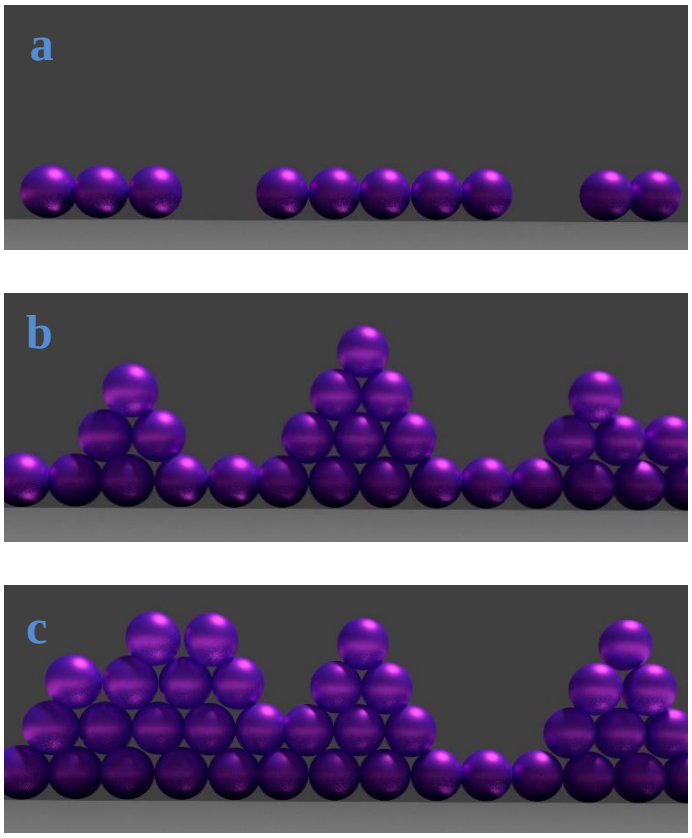

Figure 6: Stranski-Krastanov growth. a) Surface with deposited material < 1ML (monolayer) thickness. b) Surface with deposited material > than 1 ML. c) Surface with deposited material » than 1 ML.

1.3. Structural investigation methods for deposited nanoclusters

Currently there is an enormous amount of methods that can be used to investigate nanostructures. In this work, the focus is on characterising geometrical structure, in particular of deposited metallic nanoobjects.

Gaining knowledge of the geometrical structure of clusters and atoms requires a technique sensitive to sizes ranging from 0.1 nm to 100 nm. For example, for gold clusters in gas phase methods like mass spectroscopy (important in mass-selection procedures), ion mobility, action spectroscopy and trapped ion electron diffraction[104] are used. For the investigation of deposited clusters, methodological requirements are surface sensitivity, the possibility to obtain good statistics in a reasonably short time period and, in some cases, the ability to penetrate surface layers.

The most popular techniques for structural investigation of deposited clusters are microscopic, spectroscopic and scattering techniques. Microscopic techniques such as scanning electron microscopy (SEM), field-emission SEM (FESEM) and transmission electron microscopy (TEM and high resolution TEM) can provide information on the size and shape of nanostructures. TEM and HRTEM are also able to resolve core-shell structures and give information about the crystallinity, lattice fringes and even d-

spacing. Scanning probe microscopy techniques (STM, AFM etc.) can also give information on the geometrical structure and can be used in both ambient or liquid environment[109].

Spectroscopic methods like UV-Vis, can indirectly be used for the evaluation of the size of nanoparticles[110]. X-ray Photoelectron Spectroscopy (XPS) and Extended X-ray Absorption Fine Structure (EXAFS) can be used for surface analysis and give knowledge, for example, about elemental composition, electronic structure etc[60]. Additionally, XPS can be used as an indirect method for recognition of mass-selected deposited oxidised gold clusters, where one can distinguish if a cluster has 6 atoms or 7 depending on the changes of Au 4f state [111].

Widely used X-ray scattering techniques for structural analysis include: X-ray diffraction (XRD), Small- and Wide-Angle X-ray Scattering (SAXS and WAXS) and X-ray Reflectivity (XRR). XRD and WAXS are typically used for the analysis of crystalline phases in the materials, while XRR is efficient for deducing surface parameters like roughness and electronic density and thickness of a layered structure. SAXS is used for the morphological investigation of nanoclusters and macromolecules[112].

Although, all the described techniques are powerful and efficient for the investigation of clusters, the samples discussed in this work impose certain restriction a given method. Firstly, the method should be surface sensitive, since both structure types are deposited on the Si wafer. Secondly, the quantity of material is low, so an X-ray source providing high incident flux and a beam focusing capability should be used to obtain sufficient signal on a limited area. Thirdly, size-selected clusters are capped with a 5 nm layer of Al, which excludes the use of microscopic methods. Fourthly, the main interest is the shape and the size of clusters, therefore spectroscopic methods are not particularly beneficial.

This leaves only the group of scattering methods, which use synchrotron X-rays. Considering all the limitations, the most efficient method is a modification of SAXS with Grazing Incidence Diffraction, which makes use of measurement in the reflection mode, called Grazing Incidence X-ray scattering (GISAXS). It is surface-sensitive and can be useful for detection of small quantities of size-selected clusters as well as for the *in situ* deposition. It can penetrate the Al capping layer and can be used for quantitative estimation of cluster morphology.

1.3.1. Scattering methods

The primary method of investigation in this work, GISAXS, belongs to the well-known class of X-ray structural techniques. X-rays possess the abilities to penetrate into matter, to scatter from the electron densities and to resolve the structure of nanomaterials, due to the short wavelength of 0.01 nm to 10 nm[39]. The source of X-rays can be for example standard X-ray tube sources, a synchrotron or even a free-electron laser. The following results were obtained at the synchrotron PETRA III, DESY. As any electromagnetic radiation, X-rays are both a wave and a particle and can be described by the wavelength or photon energy. Their correlation is described by an equation coming from the Einstein-Planck formula[39,113] $\varepsilon = h\nu$ (where ε is the photon energy, h is the Planck constant and ν is the oscillation frequency of an electromagnetic wave):

$$\lambda = \frac{c}{\nu} = \frac{hc}{\varepsilon},$$

Equation 1

where c is the light constant.

Interaction of X-rays with matter can be divided in two groups: elastic coherent scattering and inelastic absorption and scattering. The elastic interactions are the X-ray diffraction methods, while the latter is the photoeffect (electron emission, fluorescence and Auger emission) and Compton scattering.

The key concept of X-ray diffraction methods is Bragg's law. It states that when X-rays (with wavelength λ) are scattered from a crystal lattice, peaks of scattered intensity are observed which hold conditions such the angle of incidence is equal to the angle of scattering (angle 2θ) and the path length difference is equal to an integer number of wavelength:

$$n\lambda = 2dsin\theta$$

Equation 2

The condition for maximum intensity given by Bragg's law allows calculation of details about the crystal structure (spacing of lattice planes), or if the crystal structure is known, to determine the wavelength of the X-rays incident upon the crystal.

1.3.1.1. Small-Angle X-ray scattering

To introduce GISAXS method it is important to describe first the basics of Small-Angle X-ray scattering. It is a popular non-destructive technique to investigate the structure of nanoobjects. This is possible because X-rays used to have a relatively small wavelength of 0.1 – 1nm. The elastic scattering of X-rays occurs at the electron charge densities of atoms. A sketch of a typical experiment is shown in Figure 7**.** X-rays pass through the sample in the transmission geometry. Incident and scattering beams can be

described as plane waves and their wave vectors are $\mathbf{k_i}$ and $\mathbf{k_s}$ respectively. Then $\mathbf{q} = \mathbf{k_i}\text{-}\mathbf{k_s}$ is a momentum transfer (sometimes it is called scattering vector) between them. This momentum transfer is a vector, which exists in the reciprocal space. Reciprocal space can be described as a Fourier transform of a real space, where all the peaks correspond to a periodic spacing in the object and detected by 2D detector.

Considering that modules of the wave vectors can be expressed as[40]:

$$|\boldsymbol{k_i}| = |\boldsymbol{k_s}| = \frac{2\pi}{\lambda}$$

Equation 3

In addition, the module of a momentum transfer is[40]:

$$|\boldsymbol{q}| = \boldsymbol{q} = 2|\boldsymbol{k_i}|\sin\theta = \frac{4\pi\sin\theta}{\lambda}.$$

Equation 4

In these formulae, λ is the wavelength, while θ is a scattering angle.

In the experiment the scattering intensity (rate of scattered photons) from a certain angular position is measured. It was found by Guinier[114] that the area of small angle (small momentum transfer) contains a lot of information with a high intensity about the geometrical structures in the nanometre range. That is the reason that Small-Angle X-ray scattering is a proper method to investigate nanomaterials, while Wide-Angle X-ray scattering can give information crystallographic lattices, but needs lots of scattering centres to increase the intensity which is statistically not so high for bigger scattering angles.

According to the SAXS theory, the scattering amplitude A_s from N identical particles in a volume V can be described as

$$A_s(\boldsymbol{q}) = \sum_{i=1}^{N} f_i(\boldsymbol{q}) e^{i\boldsymbol{q}\boldsymbol{r_i}},$$

Equation 5

where $f_i(\boldsymbol{q})$ is a scattering amplitude from one particle.

$$f_i(\boldsymbol{q}) = 4\pi \int_0^{\infty} \boldsymbol{r}^2 \rho(\boldsymbol{r}) \frac{\sin \boldsymbol{q}\boldsymbol{r}}{\boldsymbol{q}\boldsymbol{r}} d\boldsymbol{r}$$

Equation 6

ρ (**r**) is the distribution of an electron density (concentration of electrons in space).

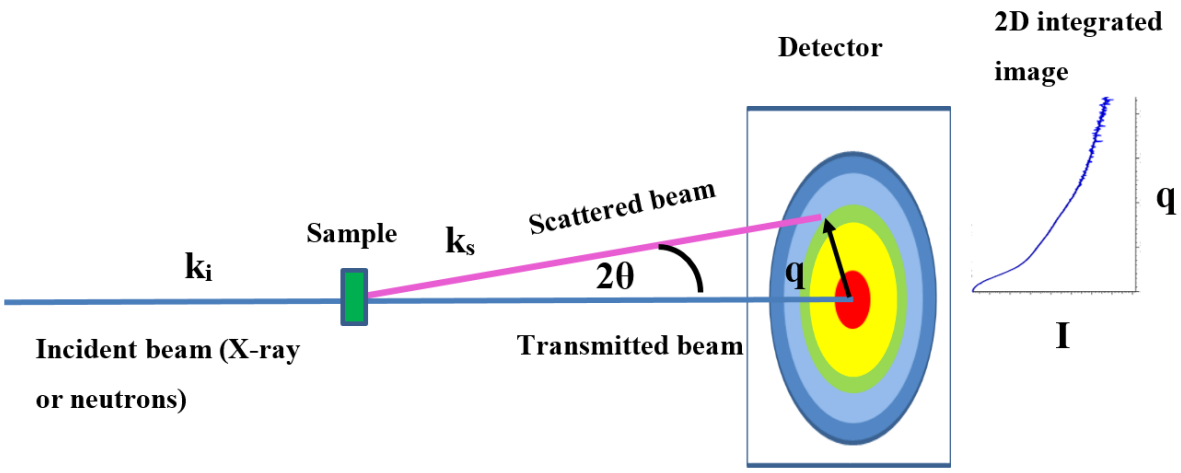

Figure 7: Sketch of the Small-Angle Scattering experiment.

In the small angle approach $f_i(\boldsymbol{q})$ can be considered a constant. Hence, instead of summation it can be integrated through the same volume and expressed as:

$$A(\boldsymbol{q}) = \int \rho(\boldsymbol{r})\, e^{iqr}\, d\boldsymbol{r}$$

Equation 7

In the real experiment, intensity is measured which is proportional to the squared amplitude:

$$I(\boldsymbol{q}) \sim A(\boldsymbol{q})A(\boldsymbol{q})^* = |A(\boldsymbol{q})^2|,$$

Equation 8

where $A(\boldsymbol{q})^*$ is a conjugate complex function. In some literature $A(\boldsymbol{q})$ for this case is called the form factor amplitude.

In general, the scattering intensity contains both form factor amplitude and so called structure factor.

$$I(\boldsymbol{q}) \sim |A(\boldsymbol{q})^2|\, S(\boldsymbol{q})$$

Equation 9

However, one can only separate them from each other in case of identical particles with spherical symmetry. In real system this does not often apply, but in case of dilute particles in solution, it can be considered that there are no interactions and the structure factor can be assumed constant[40].

To summarise, SAXS is an advanced method that can resolve form-factors and the orientation of nanoparticles. It is actively used for biological applications and especially successful in case of proteins in solution where usually only the influence of particle shape plays a role.

1.3.1.2. Principles of GISAXS

When surface sensitivity is required and nanostructures are located on a substrate, GISAXS is a more suitable method. Although transmission SAXS can be used for characterisation of nanosized objects, in case of thin films, embedded particles or particles deposited on a substrate, grazing incidence geometry helps to increase surface sensitivity. The typical scheme of GISAXS geometry is illustrated in Figure 8.

In contrast to the SAXS experiment, the X-ray incident beam impinges the surface with an angle less than 1° (usually around tenth of degrees). Then due to the grazing incidence geometry of the substrate to the beam, not only scattering but also reflection and refraction effects are observed.

The momentum transfer can be then expressed by a vector[35]:

$$\boldsymbol{q}=\frac{2\pi}{\lambda}\begin{pmatrix}q_x\\q_y\\q_z\end{pmatrix}=\frac{2\pi}{\lambda}\begin{pmatrix}cos(2\theta_f)cos(\alpha_f)-cos(\alpha_i)\\sin(2\theta_f)cos(\alpha_f)\\sin(\alpha_f)+sin(\alpha_i)\end{pmatrix},$$

Equation 10

where λ is the wavelength, α_i is the incident angle, α_f-the scattered angle in z-direction and θ_f the scattered angle in y-direction. Therefore, the data obtained with this method can be considered multidimensional.

The intensity of the X-ray scattering also contains several structural parameters and is proportional to form factor and structural factor as was mentioned in the SAXS theory Equation 9.

In the SAXS approach, the form-factor can be described with Born approximation with Equation 7, which is a simple Fourier transformation from the particle shape. However, due to the grazing incidence geometry, effects emerging from reflectivity need to be taken into account. When the incident angle is shallow, optical effects such as reflection and refraction appear. Therefore Distorted Wave Born Approximation (DWBA) is used instead[115,116].

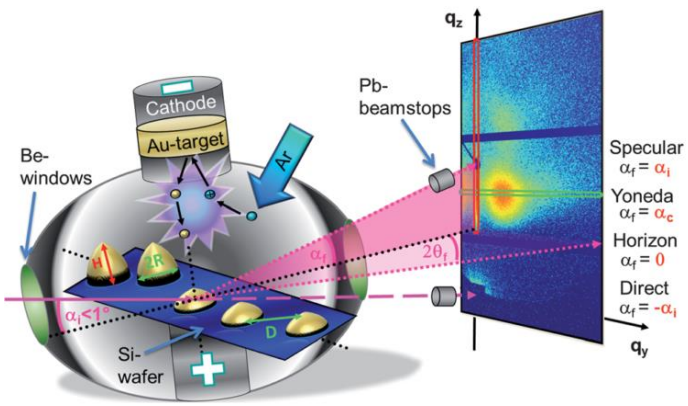

Figure 8: Sketch of a Grazing Incidence Small-Angle X-ray Scattering experiment[31].

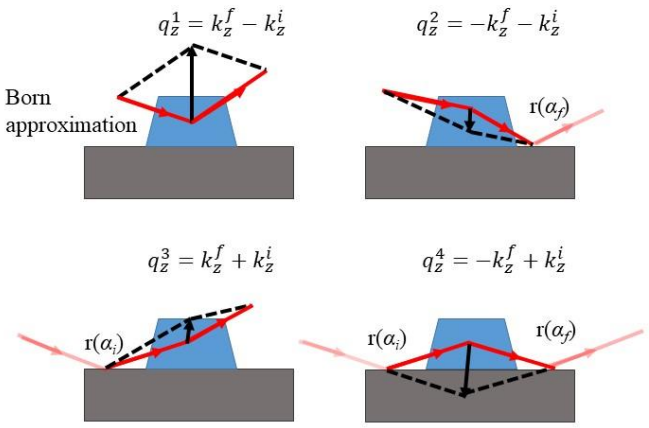

Figure 9: Scattering from one island described by DWBA.

Figure 9 shows the case of supported objects, where q-s are different scattering vectors and k-wavevectors as described above.

Then the Fourier function for the supported objects will consist of four parts:

$$A(q) = A(q_{\|}, q_z^1) + r(\alpha_f)A(q_{\|}, q_z^2) + r(\alpha_i)A(q_{\|}, q_z^3) + r(\alpha_i)r(\alpha_f)A(q_{\|}, q_z^4)$$

Equation 11

In details this is discussed in the work of Renaud, Lazzari& Leroy[117]. There is another necessary approximation, which has to be included in GISAXS theory. Although the impact of the form-factor is higher in the intensity formula, particle arrangement also has to be accounted for. The main approaches are presented schematically in Figure 10: Decoupling Approximation (DA), Local Monodisperse Approximation (LMA) and the Size-Spacing Correlation Approximation (SSCA)[118].

In DA the positions of the scattering objects are expected to have no correlation. In LMA, particles of a certain form-factor and size are considered to form a domain, and the final scattering intensity of the system is a result of a sum of such domains. In both DA and LMA, the perpendicular and the parallel directions are sometimes unable to describe certain particle types, while in the SSCA there is a coupling occurring in both directions at the same time[119]. SSCA considers that the sizes and positions are correlated with some probability[36,118].

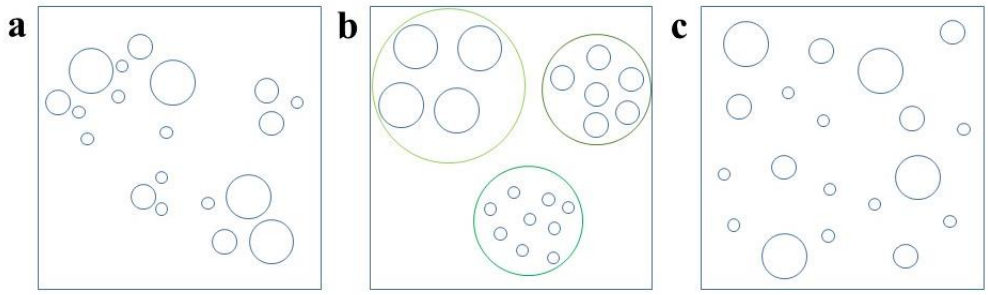

Figure 10: Schematic presentation of different particle arrangements used to calculate the X-ray scattering. a) Decoupling approximation; b) Local monodisperse approximation; c) Size-Spacing Correlation Approximation.

In addition to the form-factor and scattering factor in GISAXS one should consider the Vineyard factor[116], which in the scattering picture appears as a bright intensity band at the critical angle of the material. It can also be called the Yoneda peak[120], which results from the dynamical scattering effect when the exit angle is equal to the critical angle. This high intensity is caused by the incident angle and reflected angle having similar amplitude and being in phase. In case of thin films, this Yoneda band of higher intensity can broaden and is located between the critical angles of the substrate and the deposited material. GISAXS data analysis approaches used in the current work are described in Section 2.2.2.

Despite that, several approximations are required, GISAXS still remains a versatile method particularly suited for structural characterization of objects deposited on substrates with high surface sensitivity. GISAXS provides high surface sensitivity and can obtain information both of the radius and the height of the nanostructure.

1.3.1.3. Hemispherical model by M. Schwartzkopf.

In their hemispherical model Schwartzkopf *et al* [31] suggested a quantitative approach of radius estimation from the position of the Yoneda maximum. In this work the growth of Au clusters on the Si/SiO_2 surface was investigated *in situ*. Gold clusters were considered to be of hemispherical shape and arranged in 2D hexagonal lattice, see Figure 11**a.** $D = {2\pi}/{q_{y,max}}$ [35] is the average interparticle distance (Equation 17, described in Section 2.2.2); R is the average radius of one cluster and δ is the effective thickness of the triangular area. The volume of the red triangular area is considered equal to three times the 1/6th of each hemisphere.

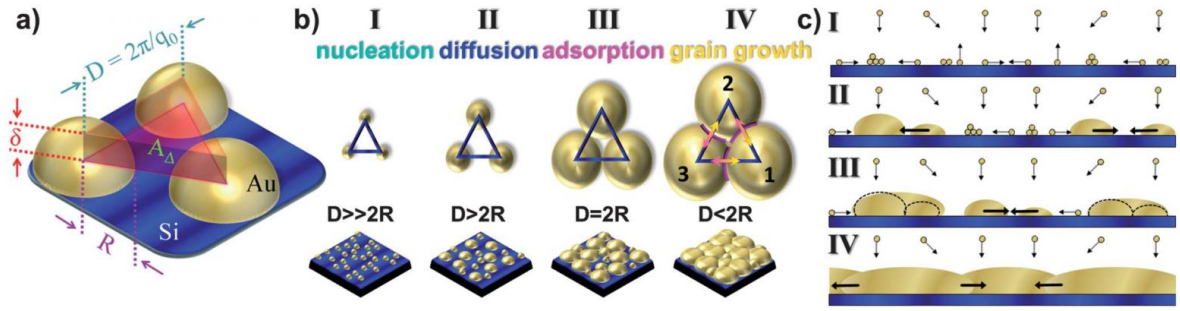

Figure 11: Evolution of model-based morphological parameters. Caption taken from the article of Schwartzkopf et al[31].: (a) 3D scheme of the geometrical model: virtually isosceles triangular prism of thickness δ and area A_Δ between the separated hemispherical clusters of distance D and radius R. (b) Gold cluster growth during sputter deposition consists of four stages: (I) nucleation; (II) diffusion-mediated coalescence (D >2R); (III) adsorption-mediated cluster growth until percolation threshold (D = 2R). Afterwards a dominant cluster (1) permanently grows by a movement of grain boundaries (IV; violet) at the expense of the adjacent clusters (2, 3) (D < 2R). (c) Side view scheme of each stage of gold cluster growth showing the predominant processes. The black arrows indicate the movement of adatoms, clusters and grain boundaries. Note that the conventional name for q_0 which is in the picture is $q_{y,max}$, as it is referred in the text.

The radii of these hemispherical gold clusters are calculated by:

$$R = \sqrt[3]{\frac{(\sqrt{3})^3 \delta D^2}{4\pi}}$$

Equation 12

It is proposed that from the radii R of the clusters it is possible to estimate the number of atoms in a cluster[121]:

$$N_{(atoms/cluster)} = \frac{1}{2}\left(\frac{R}{r_{cov,Au}}\right)^3$$

Equation 13

This model is used to evaluate both structures discussed in this work: co-deposited Au/Ag clusters and size-selected Au clusters. However, for the latter system this model is not a perfect match, it works reasonably well and in agreement with theoretical works of the geometrical structures. Note: coverage value is used as an effective thickness in this formula for ultrasmall clusters (10% ML would be equal to 0.0288 nm).

The proposed four growth stages are presented in Figure 11 **b,c.** It is demonstrated that the ratio of D to R changes when the amount of deposited gold is increasing; the percolation threshold occurs when the D is equal to two radii. Upon reaching the percolation threshold one of the clusters becomes dominant and changing its borders at the expense of the adjacent clusters.

1.3.2. Supplementary methods.

1.3.2.1. X-Ray Fluorescence (XRF)

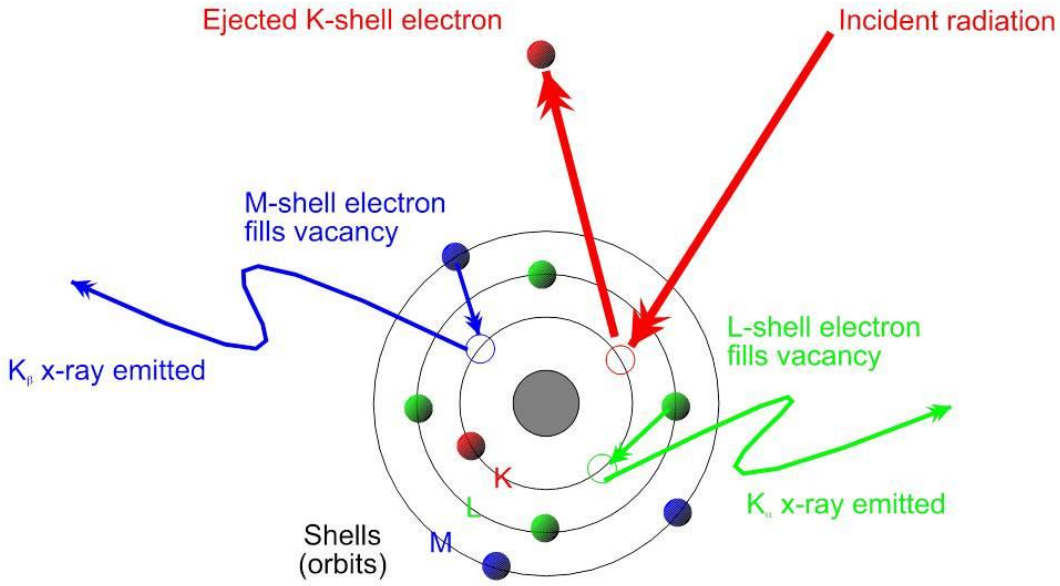

Figure 12: Schematic presentation of the working principle of XRF[122] .

XRF was used as a supplementary method simultaneously with GISAXS (Figure 12). The main working principle of this method is that incident X-rays when interacting with electrons, energise them and they leave their shell (usually it happens in the K or L shells). Subsequently an electron from an outer shell fills the vacancy. Since they have higher energies on outer levels, they need to lose energy as an emitted photon, resulting in fluorescence radiation. This radiation is detected and the elements producing it can be determined because they emit in a known energy range.

1.3.2.2. X-ray Photoelectron spectroscopy (XPS)

This method uses a similar principle to XRF but instead of characteristic X-ray emission, the ejected electron is measured. The material properties can be determined using energy conservation:

$$E_b = E_{photon} - (E_{kinetic} + \varphi),$$

Equation 14

E_b is the binding energy of the electron, E_{photon} is the energy of the X-ray used for bombardment, $E_{kinetic}$ is the energy measured by the spectrometer and φ is the work function of the instrument.

2. Experimental and analysis methods

This section describes experimental conditions and analysis approaches used in this work. In this work samples have been prepared in two different method. First, nanoclusters are prepared by deposited atoms on a surface and growing clusters on the surface, which are not size selected. Second, supported size selected cluster samples are prepared by producing them in a sputter source, mass selecting them and finally deposited them on a surface in a soft landing scheme. The different experiments used will be presented in the following sections.

The sample preparation procedure consists of two parts: substrate cleaning and the deposition process. While the cleaning procedure for both sample types is the same, storage conditions prior to the deposition and deposition parameters differ significantly.

2.1.1. Substrate preparation.

For sample preparation boron-doped single crystal Si wafers (Si-Mat, Germany) (100) were cut to sizes of 9 × 9 mm^2 and 15 × 15 mm^2, using a diamond saw. Resulting pieces were cleaned in an ultrasonic bath for 15 min using acetone. They were then rinsed with isopropanol (isopropanol to water ratio 3:1) and deionised water. Afterwards, a Piranha acid treatment was applied with a solution of 200 mL of 96 % H_2SO_4, 88 mL of 35 % H_2O_2 and 37.5 mL of deionised water. Substrates were kept in this solution for 15 min, while the temperature of the heating plate was kept constant at 80°C.

This procedure resulted in a substrate cleaned from organic residuals and with a smooth oxide layer on the surface and an increased adhesion of the sputtering material[123].

Prior to the deposition the substrates for *in situ* RF-magnetron sputtering were kept in distilled water and dried with a nitrogen gun just before placing them into the HASE chamber. The substrates for ion sputtering of size-selected clusters were dried at 80 °C in a vacuum heater and kept in separate clean boxes.

2.1.2. Cluster deposition.

Two types of differently prepared clusters were produced in this work. The first one was produced by RF magnetron sputtering and the structure was investigated during the deposition process. The second one was prepared using Ion cluster source and investigated after the deposition.

2.1.2.1. RF-magnetron sputtering chamber HASE

In this work the Highly Automated Sputtering Equipment (HASE) chamber[78] was used, equipped with RF sputtering guns. The chamber was designed for experiments at P03 beamline, PETRA III, DESY (Hamburg). RF uses an alternating current between the target and the substrate with a frequency of 13.56 MHz. In comparison with direct current, this prevents charge building up on the dielectric target materials and thus allows a wide range of materials as targets. The working gas used is Ar with a working

pressure of 2.5×10^{-2} mbar, and the vacuum needed for deposition of Au or Ag can be as high as 5×10^{-6} mbar. The HASE chamber (see Figure 13) is rather advanced and it is compatible for mounting and use at a synchrotron source. It allows the use of several sputtering sources in different geometries, heating of the sample stage during the process, and is equipped with a quartz microbalance to control the deposition rate. The large exit window and the sample stage motors make *in situ* grazing incidence small- or wide-angle X-ray scattering experiments possible. For further details on the chamber and options offered for different kinds of experiments see Dörmann *et al.*[78]

2.1.2.2. Samples prepared using HASE chamber.

Several samples have been prepared and measured, using the HASE chamber. The aim was to assess the geometrical structure of Au/Ag mixture with ratios of 50%/50% at room temperature and heated, during growth. For comparison deposition of pure metals of Au and Ag and alternate deposition of Au on Ag was performed. Hence, either one or two guns with targets of Au and Ag (Goodfellow, UK) were operated. The sample list is provided in Section 3.1 in Table 2.

The following procedure was used:

1) Single substrate was placed in the chamber.
2) Vacuum was started with Quartz Crystal Microbalance (QCM) (Inficon, Switzerland) 'in' (i.e. also used as shutter to prevent deposition on substrate)
3) As soon as pressure in the chamber reached $5 - 7 \times 10^{-6}$ mbar, Ar gas was injected for plasma ignition; working pressure during deposition was 2.5×10^{-2} mbar.
4) Before each of depositions the cluster rate was measured using Quartz Crystal Microbalance (QCM) (Inficon, Switzerland), but instead of the values given by the program Sycon the Sauerbrey equation[124] was used (see Appendix: 5.1). These values were calculated each time before the deposition started. Note: the necessity to measure it each time was due to the irreproducibility of the cluster flow after breaking the vacuum.
5) When rates of both metals (Au, Ag) were stabilised and proved to be constant and equal to 0.005 ± 0.0003 nm/s, the QCM was moved "out" and the deposition started.
6) As soon as the effective thickness reached 10 nm, the QCM was in the position "in"; the sputtering guns were stopped.

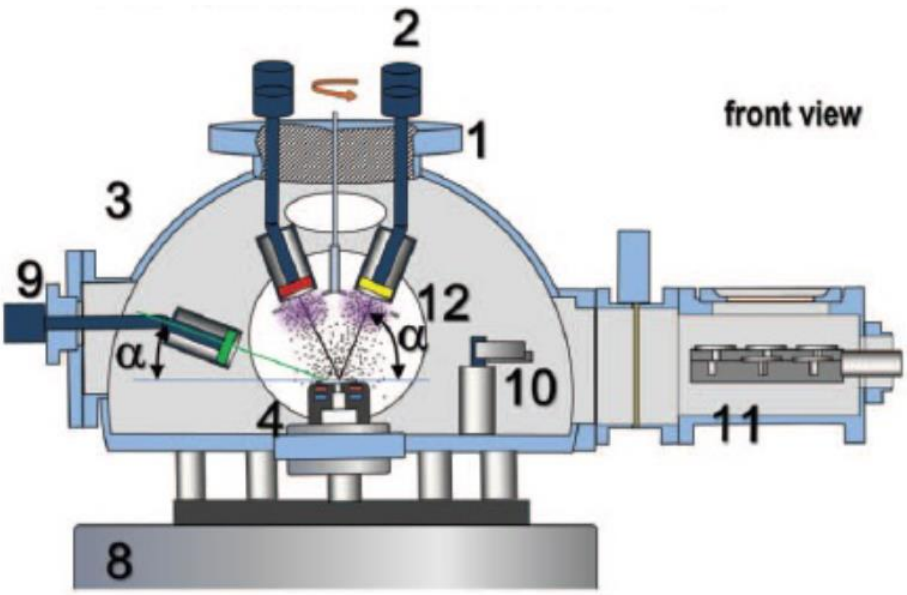

Figure 13: (Taken from [78]) Schematic drawing of the Sputtering chamber HASE with: (1) rotatable flange, (2) sputter guns, (3) vacuum deposition chamber, (4) sample stage, (6) plasma, (7) beam defining slit system, (8) sample positioning device, (9) additional sputter gun for GLAD sputter experiments, (10) sample change robot, (11) sample container, (12) exit window, (13) mask, and (14) position of the upper sputter flange.

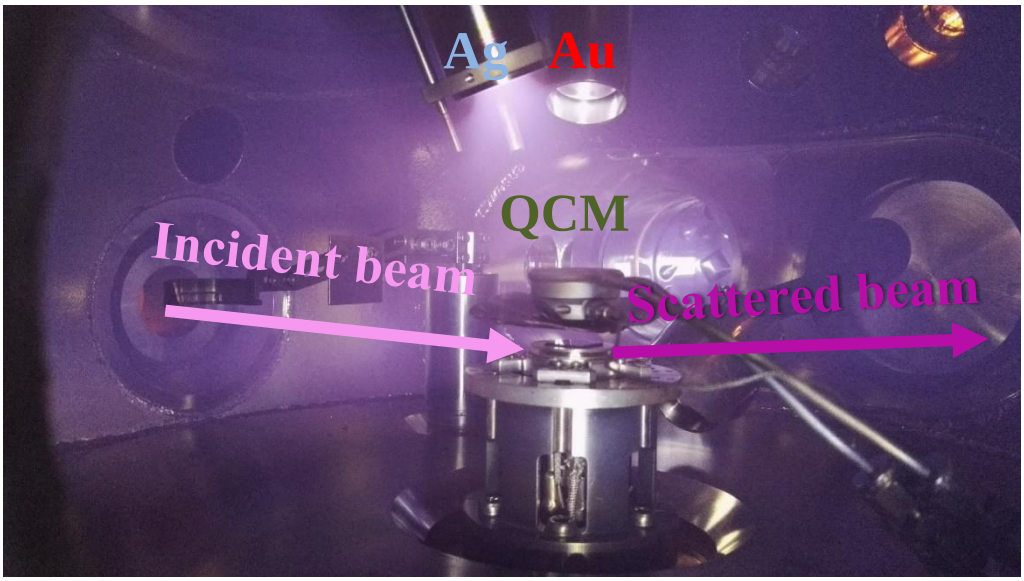

Figure 14: Side view of the sputtering process from two targets. The angle between the Au and Ag guns is 40°.

The view from a side window during the sputtering from two targets is shown in Figure 14. The position of guns was kept the same for all samples. Other possible configurations of the guns are discussed by Döhrmann *et al*[78].

All samples were studied *in situ*, description of the experiment, using GISAXS as described in Section 2.2.1.

2.1.2.3. Ion sputtering setup ICARUS

The Ionic Clusters by Argon spUttering Source[27] (ICARUS) is an ion sputtering device allowing for directed sputtering. Currently it is operated with Xe as working gas, as it is heavier than Ar and therefore more efficient for cluster preparation. The whole setup (shown in Figure 15) consists of three parts, where the first two (I and II) are the sputtering source with a set of focusing lenses and a dipole magnet for mass-selection. The third (III) is an endstation which is easily replaceable to fulfil needs of a specific experiment. The whole system works in Ultra High Vacuum (UHV) conditions. Details of the working principles of ICARUS are explained in the Thesis of Ehrke [125] and by Lau[95].

The mechanism of noble gas ionisation in an ion sputtering source differs from RF-sputtering. It is induced by a filament heating in a high potential, around 30 keV and afterwards Xe^+ ions are focused by an electrostatic lens system, applying a high voltage of around 20 keV. Polycrystalline metal discs of high purity (99,99%) are used as targets. From the primary ion beam, metal atoms acquire enough energy to leave the surface and to form clusters, whose yield is inversely proportional to their size[126]. The process of cluster nucleation in gas phase is considered to consist of two steps: 1) cluster growth by monomer addition; 2) cluster intercoagulation[127]. The resulting clusters are positively charged , as cations were shown to have higher yields than neutral or negative clusters[95,128]. Mass spectrum of Au cations is shown in Figure 15**b.**

The obtained metal clusters and atoms pass through the dipole magnet, while their movement is controlled by a system of electrostatic lenses. There they are separated via interaction with the magnetic field according to their charge to mass ratio. This allows the control that only mass-selected clusters of a certain size pass into the deposition chamber. Detailed information about the High Field Magnet Chamber (HFK) which was used in this work can be found in thesis of Beeck[129]. In the deposition chamber clusters are decelerated by a high potential of the retardation electrostatic lens to a kinetic energy of 1 eV or less per atom in a cluster, in order to reduce cluster fragmentation. However this has proved not to be sufficient to prevent fragmentation, therefore the use of a soft-landing scheme is indispensable[130,131]. This implies creation of a noble gas matrix on the substrate surface, which requires constant temperature at a freezing point of this gas from the moment it is injected on the surface. The soft-landing scheme is described in detail by Cheng and Landmann[130] and in reviews[33,38].

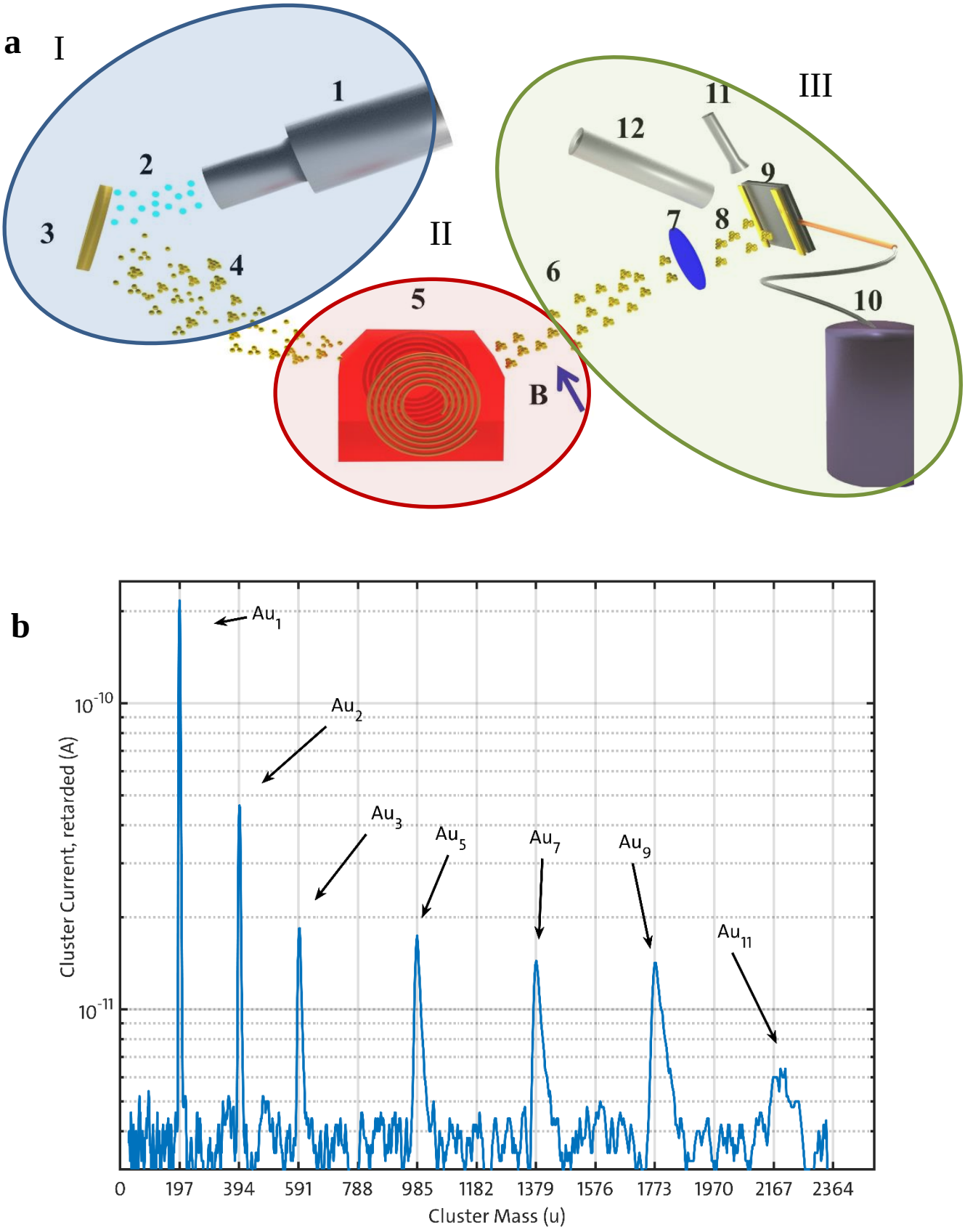

Figure 15: (a) Cluster sputtering source ICARUS. 1. Sputter gun. 2. Xe+ ions. 3. Au target. 4. Au clusters and adatoms. 5. Dipole magnet for mass selection. 6. Mass-selected clusters or adatoms. 7. Retardation lenses. 8. Mass selected clusters with E_{kin}<1 eV/atom. 9. Si substrate with Au markers. 10. He cooling for the substrate. 11. Kr gas shower. 12. Evaporator with Al. I, II, III are the three main parts setup can be divided[132]. (b) Mass-spectrum of cationic Au clusters, produced by ICARUS.

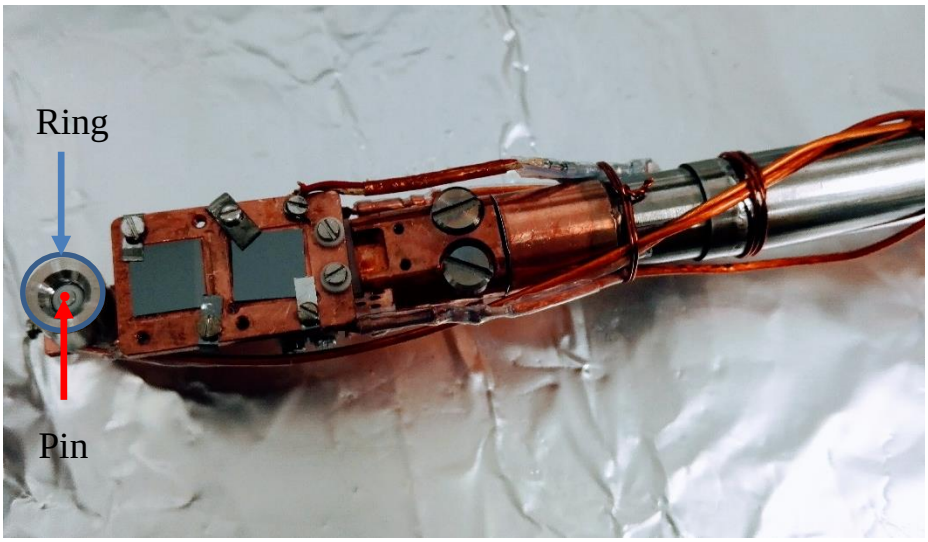

Figure 16: Sample holder with Si wafers installed prior to the deposition. Diagnostic unit consists of ring (blue) and pin (red), isolated from each other by ceramic element.

For this work it was important that the sample holder was designed such that it has a diagnostic unit, which consists of a pin, ring and the insulating connector, which is depicted in Figure 16. It also had an installation for a thermocouple to measure the temperature on the substrate as well as a heating element, which allows heating to 900K. The pin has a size of 2 mm in diameter and the initial cluster beam is focused onto it. The normalised signal is then used to calculate the amount of time needed to have a certain effective thickness of the material deposited [129]:

$$t_d = \theta_s \frac{\rho_s A_{pin} e}{In} \ ,$$

Equation 15

where t_d is the cluster deposition time [s], θ_s is the cluster coverage in monolayers [ML], ρ_s is the atomic density on deposition surface [atoms/mm^2], A_{pin} is the diagnostic pin area [mm^2], e is the elementary charge, I is the cluster current on the pin [A], and n is the number of atoms per cluster.

As an example, for the surface of Si (100) Equation 15 will look like:

$$t_d = \theta_s \frac{56877.3}{In}$$

Equation 16

After the yield estimation has been carried out on the pin, clusters are deposited in the noble gas matrix, gas is removed when the amount of material aimed for is deposited on the surface. Note that in case the substrate is Cu crystal one can carry out an investigation using one of the spectroscopic techniques immediately, but in the present experiment clusters were deposited on Si and then removed from UHV. A step-by step scheme and description of the preparation for the *ex situ* measurements of the deposition experiment is given in Section 2.1.2.3.

2.1.2.4. Samples prepared using ICARUS cluster source.

Ultrasmall size-selected gold clusters were prepared according to already established principles of preparation for such samples which are shortly described above and in details in the following works [33,98,133]. The scheme of this experiment is shown in Figure 15. On some of the substrates, one or two Au markers were deposited –thin lines of Au clusters sputtered in HASE (see step 2 in Figure 17), prior to placing in HFK deposition chamber.

For the experiment UHV conditions were fulfilled: the starting pressure in the sputtering chamber was below 1 x 10^{-7} mbar, while in the magnet and in the deposition chamber it was 1 x 10^{-9} mbar. This is essential for preparation of clean samples. At the beginning, all three parts were closed from each other by a system of shutters. Liquid He was used to cool the sample down to -200 – -210 °C. When the temperature reached this value, the substrate was heated to 100 °C to remove possible contamination of the sample which could occur between chemical cleaning and mounting of the substrate on the sample holder. Then the substrate was cooled down again to -210 °C.

In Figure 17 steps of sample preparation are shown. During the first step the substrate was cleaned according to the procedure, described in Section 2.1.1. During the second step Au markers were deposited. In the third step on the cooled substrate Kr matrix of about 5 – 10 ML was deposited. Kr gas was injected for 30 s with a pressure of 1x10^{-2} mbar inside the gas dosing system. Given the fact that the temperature during the deposition was kept constant, this noble gas stayed on the surface. Afterwards all the shutters between the magnet, cluster source and HFK chamber were opened to start the deposition. Soft landing of gold clusters was performed in the fourth step, when they were also retarded to about 1 eV/atom. The deposition time varied from sample to sample, and to estimate this time Equation 16 was used. Past material deposition Kr matrix was removed by heating the sample to -100 °C. Thermal Desorption Spectrometer (TDS) was used to confirm that the gas left the surface of the substrate. The final, sixth step was the capping of the deposited clusters with 5 nm of evaporated Al. Later, the thickness of the capping layer was measured using XRR (see Appendix: Section 5.7). Afterwards, the samples were allowed to warm to room temperature, and they were removed and stored in individual boxes before the measurement.

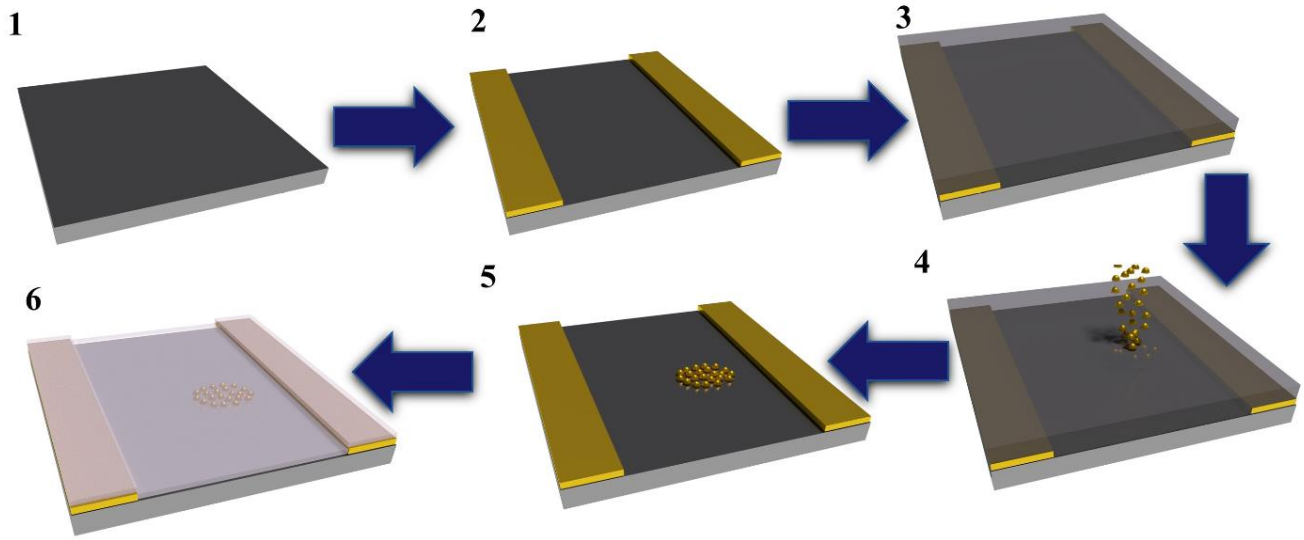

Figure 17: Scheme of the sample preparation. 1. Si substrate 9x9 mm^2. 2. Au markers (2 mm width, 10 nm height) sputtered on the edges. 3. Frozen Kr gas on the surface. 4. Soft landing of Au_9 in Kr matrix in the spot with the radius of 1 mm. 5. Kr matrix removed and clusters landed. 6. Al capping layer evaporated on the system[132].

Sample name	Atoms in cluster	Coverage [% ML]	Soft-landing	Capping layer	Au markers [number]	Marker thickness [nm]
1AUSL1	1	50	+	+	2	10
1AUSL2	1	10	+	+	1	5
1AU1	1	50	–	–	0	0
5AUSL1	5	10	+	+	0	0
7AUSL1	7	10	+	+	1	5
9AUSL1	9	10	+	+	1	10
9AUSL2	9	10	+	+	0	0
11AUSL1	11	10	+	+	1	5

Table 1: Samples prepared using the ICARUS cluster source.

The effective thickness of 10% ML was chosen as it constitutes an optimal balance between the sensitivity of the experimental method applied and potential agglomeration when depositing small quantities of material. This applies for all samples, except for two - 1AUSL1 and 1AU1 (see Table 1). The reason for applying 50% ML in these cases was to test the possibility of cluster detection, since the coverage is much higher. The illustration of the typical sample appearance is shown in Figure 18. There it is easy to see 5 nm of the marker, but indeed, ultrasmall cluster spots are not visible. The markers were also extremely useful for sample alignment during the GISAXS+XRF experiment.

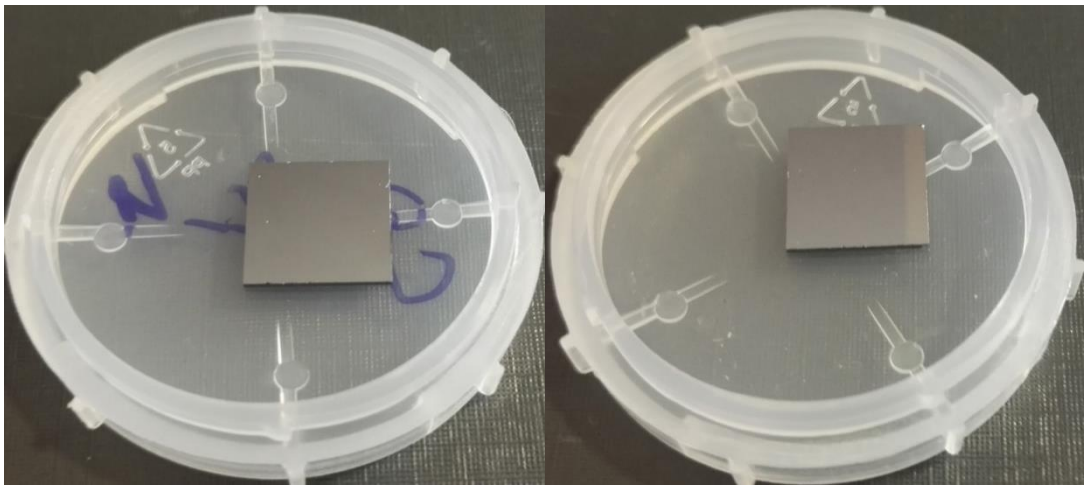

Figure 18: Photo of samples 9AUSL2 (left) and 11AUSL1 (right)

2.2. Sample investigation

In this work, GISAXS at P03 beamline, DESY, PETRA III, Hamburg was used as the main method of investigation. In general, the beam energy was kept to around 13 keV with beam size 20 × 30 μm² (H × V). However, the experiments performed for the two sample systems discussed here had several important differences between them. The primary difference is that the co-sputtered samples were investigated *in situ*, while the ultrasmall size-selected deposited Au_n were investigated *ex situ*.

2.2.1. GISAXS beamline MiNaXS

Beamline optics

In this work, all diffraction experiments were performed at the Micro- and Nanofocus X-ray Scattering (MiNaXS) beamline (P03)[134], PETRA III, DESY (Hamburg). The scheme of the optical hutch (1 and 2) is shown in Figure 19. This beamline allows experiments using X-rays of photon energy from 8 –23 keV. The energy adjustability of the beamline is provided by a high-β canted 2 m long U29-undulator, with a period length of 29 mm. Beam is monochromated after going through the undulator, shaped and focused on the sample without losing high brilliance.

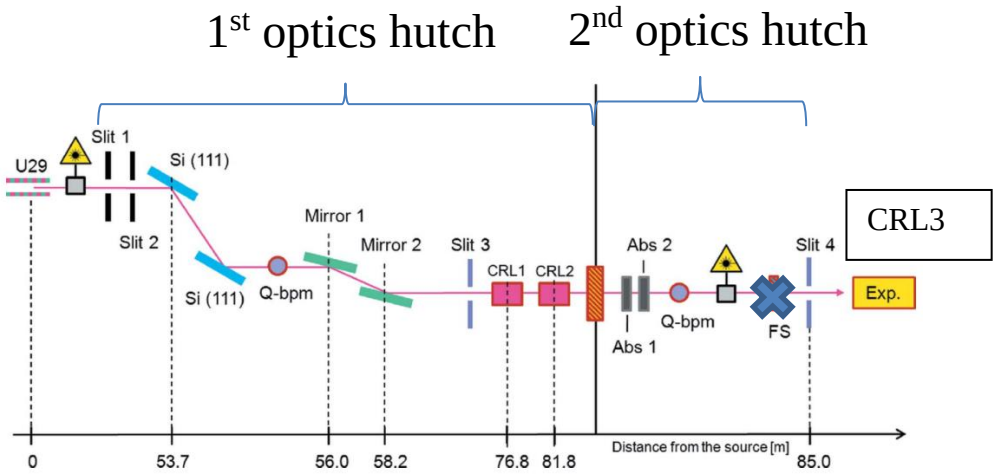

Figure 19: Updated sketch of the MiNaXS beamline optics[134]. (FS-fast shutter, Abs-Absorber, CRL-compound refractive lens, Q-bmp- quad beam position monitor, Exp-experimental hutch) Note: state as of 09.2018 – CRL3 successfully installed in the experimental hutch, fast shutters deinstalled.

In the 1st optics hutch after the undulator and opening/closing the beam Slits 1 and 2, a large-offset double-crystal Si (111) monochromator is placed, which allows compact arrangement of two beamlines together (P02 and P03). In this case, two upcoming beams can be shifted from each other in the vertical direction. The monochromator is used to slice a certain energy band from the incident beam. After the monochromator a quad beam position monitor is installed, and then placed two mirrors to suppress higher harmonics. They both have three coating options, a SiO_2 coating for the energy range 8–12 keV, a molybdenum (Mo) coating for the energy range 12–18 keV, and a palladium (Pd) coating for the energy range 18–23 keV[134]. Slit 3 placed after the mirrors is used to adjust the size of the beam, which goes into the second optical hutch. There are three Compound Refractive Lenses (CRL)[135] installed which are collimating and focusing the beam. Each of them consists of eight blocks, which can be adjusted to the energy of the beam for the higher resulting performance. They are made of beryllium (Be) which has a low atomic number and high density and can be set to match the energy of the beam.

In the 2nd optics hutch, absorbers made of Al and Ag thin foils are installed behind CRL2. They are useful to control the intensity of the beam falling on the sample. They can be used when searching for the position of the primary and the specular beams to prevent damage of the SAXS/WAXS detectors (e.g. Pilatus 300K or 1M). Absorbers are also useful to easily adjust the incident flux when carrying out experiments implying the detection of intensity variations of orders of magnitudes like in XRR. Behind the second Q-bmp is installed Slit 4, shaping the outcoming beam. This type of installation in both optical hutch helps to deliver a good shaped, brilliant beam of 20x30 µm size in the microfocus experimental hutch.

Experiment hutch MiNaXS

The experimental microfocus end of P03 beamline can be divided in three main parts: sample stage, flight tube and detectors. It is quite versatile and provides lot of possible experiment installations, which can be adjusted to the specific needs of an experiment.

The sample itself can be placed in the ambient condition and sample positioning, alignment and movement (x, y, z directions and also rotations) with high precision can be insured using either a hexapod or a Huber tower[134]. There is also a possibility to install a high-vacuum chamber for sputtering, like HASE[136] (which belongs to the P03 beamline).

In scattering experiments, it is always useful to be able to control the q-range to be covered by the detector. An evacuated flight tube is important for scattering experiments, since it reduces parasitic scattering from air. At MiNaXS, the flight tube design allows experiments from 1.5 m to 5 m sample to the detector distance (SDD). This means that the experimental conditions can be adjusted, if necessary, for measuring small structures (starting from 0.5 nm) or bigger structures (10-100 nm).

The third and very important part is the detector. Key requirements are high spatial resolution and sensitivity to hard X-rays. One of the most common synchrotron detectors used at P03 is a silicon based pixel detector, Pilatus 300K from Dectris. Besides others, it is possible to use a larger Pilatus 1M (Dectris)[137], shared by several synchrotron beamlines. Both detectors have a pixel-size of 172×172 μm^2 and allow for frame rates of 200 Hz and of 25 Hz, respectively. Both frame rates suit for *in situ* deposition experiments as well as measurements of *ex situ* samples. The primary advantage of Pilatus 1M for the experiments discussed in this work is a larger total sensitive area compared to the 300K. To protect detectors from high intensity radiation, beamstops made of Pb are used to block the primary beam and the specular beam. Another detector at P03, used in XRF measurements in this work is a Vortex-EM silicon drift X-ray detector. It has a resolution of <130 eV FWHM at Mn K_α and a high count rate capability[138].

Figure 20 illustrates a possible configuration of the experiment with minimal SDD 1.5 m. On the crane on the right side from the flight tube, a XRF detector is installed on the crane. The crane can be also used for WAXS detector installation and allows precise position alignment.

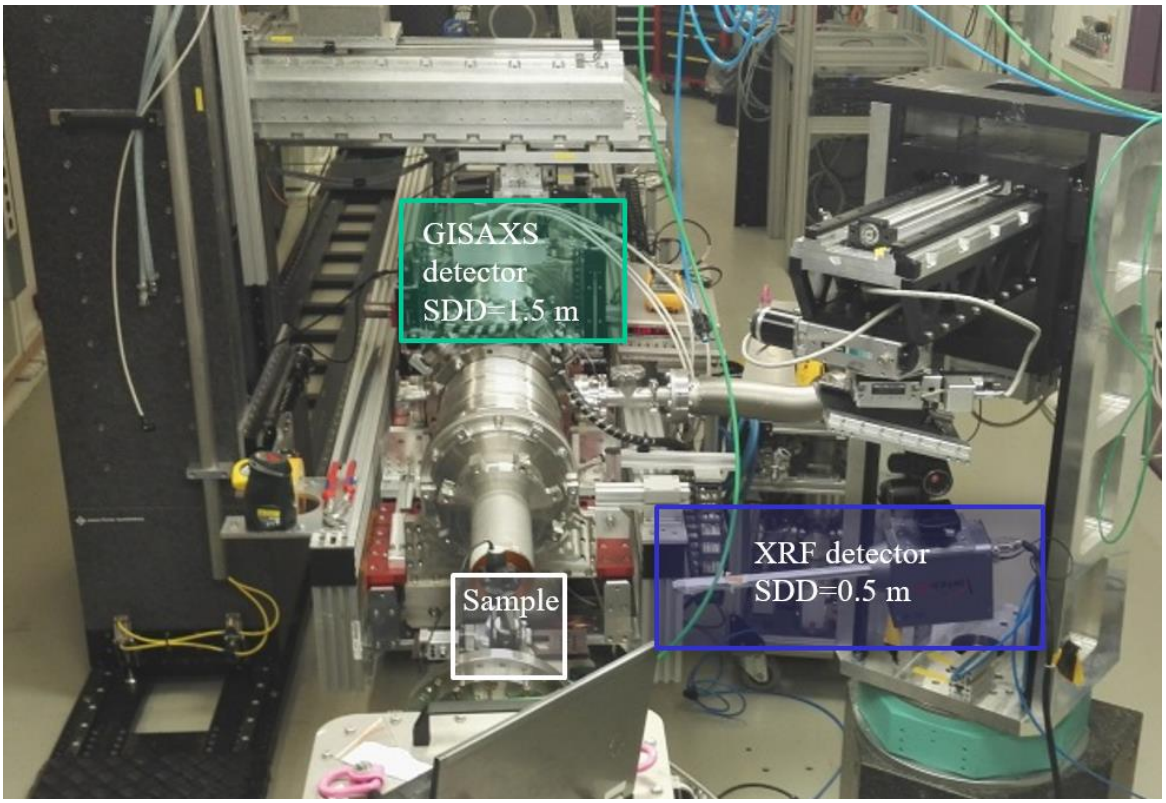

Figure 20: Photo of the experimental hutch at P03 arranged for the simultaneous measurement of GISAXS and XRF. SDD is the sample to detector distance.

2.2.2. GISAXS data analysis.

GISAXS is a well-known experimental technique to study the structure of nanosized particles in surfaces. Due to the grazing incidence geometry, such effects as multiple refractions and reflections take place, as well as scattering from the particles.

There is a variety of different tools for data analysis, but still there does not exist a standardised approach. In this work, most of the analysis was carried out using the DPDAK program[139] to extract cuts and process the fitting of the resulting 1D data. For the simulation of scattering patterns based on basic shapes, IsGISAXS[140] was used.

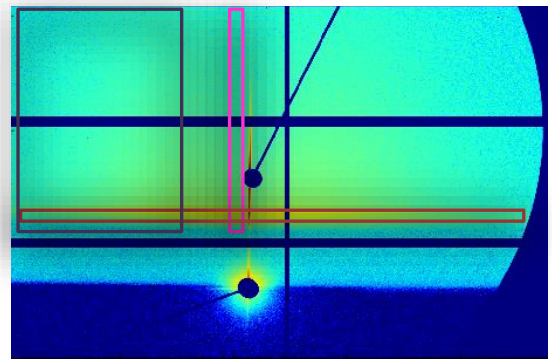

Figure 21: Image from the detector Pilatus 1M illustrating possible cut positions. (Pink-detector cut, violet-off- detector cut, burgundy-"out-of-plane" or Yoneda cut)

DPDAK software is able to process the data obtained from Pilatus detectors. To enable data processing it is necessary to enter the following values from the experiments into the program: wavelength, primary beam position, specular beam positions, incident angle, sample to the detector distance, pixel size and detector tilt. These values are used to calculate the appropriate q-range from the pixel positions of the detector. For analysis, data reduction can be applied by integrating the intensity distribution from the 2D scattering pattern in the horizontal direction along q_y ("out-of-plane" or Yoneda cut) and in the vertical along q_z ("off-detector cut") at a finite q_y (typical ranges covered are e.g. ($0.1 < q_y < 2.2$ nm^{-1})) or along q_z but around q_y=0 ("detector cut"). In Figure 21 the suggested positions of such cuts are shown. Note: The nomenclature (e.g. "out-of-plane", "off-detector cut") is used as in the review article by Roth and Schwartzkopf[29].

If the first cut is made at the critical angle of the substrate (e.g. for Si it is at $q_z = 0.7$ nm^{-1}), this so-called Yoneda cut gives the information on correlations in the lateral electron density distribution, mainly the average interparticle distance[35] (Equation 17), the size and the shape of the layout of nanostructures in the near surface regime[29].

$$D = \frac{2\pi}{q_{y,max}}$$

Equation 17

Similarly, the off-detector cut projecting the intensity in the q_z direction contains electron density correlations perpendicular to the surface, for example the average nanoparticle height or the thickness and roughness of a layer[29,35]. The detector cut can be used to estimate height[31] of the bigger structures (some nm):

$$H = \frac{2\pi}{\Delta q_z},$$

Equation 18

where Δq_z is the distance between the maxima or minima of the system in the vertical cut ('off- detector cut').

To analyse these cuts they were combined into contour plots to show the changes with time, distance or thickness. Such contour plots are helpful to make a quantitative analysis of the whole system.

2.2.3. Investigation of co-sputtered Au and Ag.

For the co-sputtered samples, prepared in room temperature conditions (Table 2), the experimental setup had the same geometrical arrangements during the *in situ* experiment. The sample to the detector distance (SDD) was 2.431±0.002 meters and the incident angle was 0.41±0.02 deg. For the samples AuAgA, AuonAgA (deposited at 185°C) the incident angle was 0.42±0.02 deg, while the SDD was

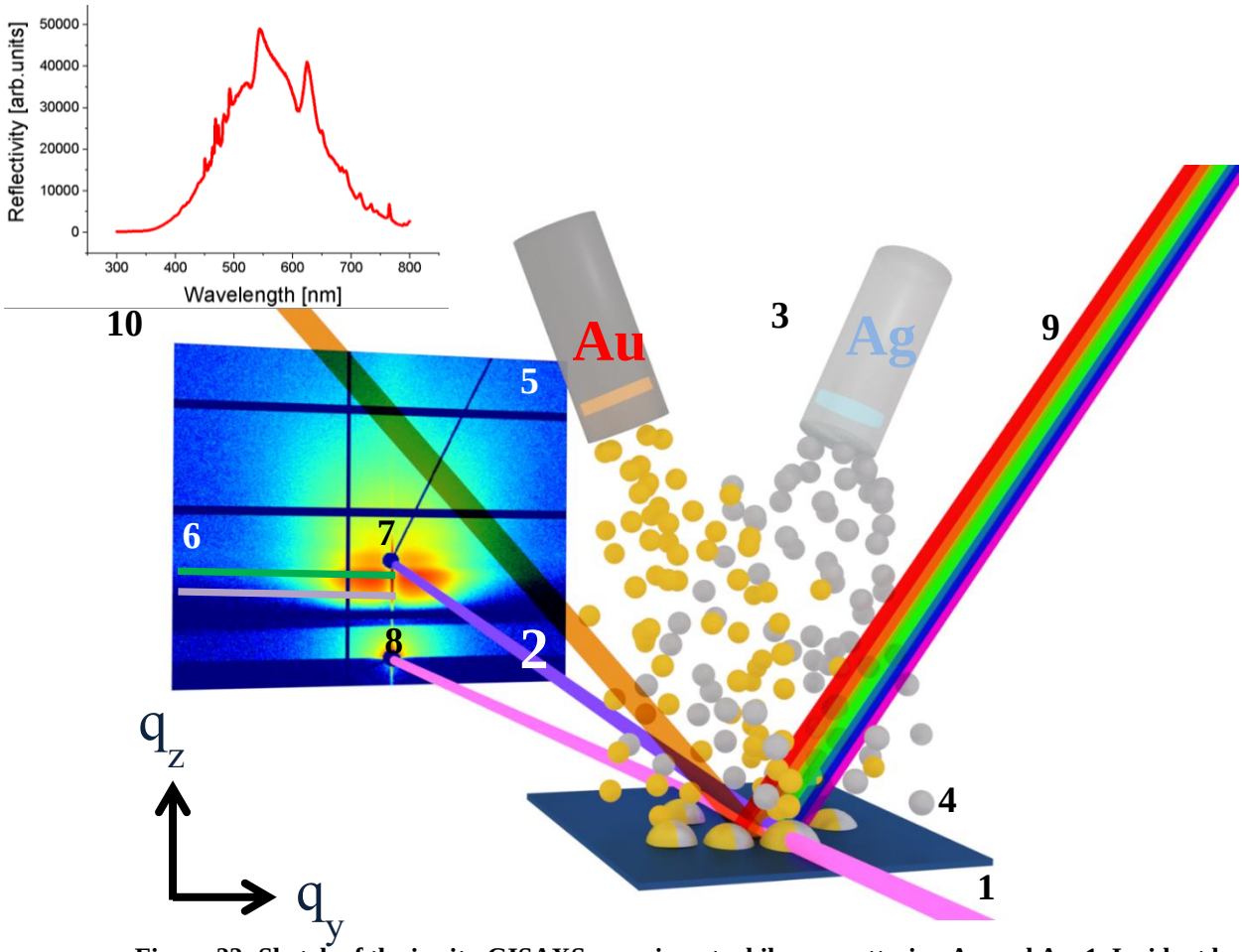

Figure 22: Sketch of the in situ GISAXS experiment while co-sputtering Au and Ag. 1. Incident beam from the synchrotron Petra III, DESY, Hamburg. 2. Beam reflected from the sample. 3. Sputtering from two sources simultaneously, 40° the angle between Au and Ag source. 4. SiO_2 substrate with mixed clusters forming on the surface, inclined 0.41deg to the beam. 5. Example of a raw GISAXS pattern. 6. Critical angle of the deposited material (green) and Si (lavender). 7. Position of the specular beam. 8. Position of the primary beam. 9. Beam from UV/Vis 75W Xe lamp. 10. Light reflected from the surface and example UV/Vis spectrum taken. Note: the chamber walls are not drawn (this drawing is an artistic view and sizes shown are hyperbolised for clarity)

4.161±0.002 m. This angle was chosen to be bigger than the critical angles of Au (0.34 deg) and Ag (0.27 deg) to prevent the beam being fully reflected from the surface.

The HASE chamber (Section 2.1.2.1) was installed at the beamline such that the X-ray beam from synchrotron passed through the entrance and the exit windows. An UV-Vis spectrometer was above of one of the chamber windows to acquire reflectivity spectra past the deposition, but before sample removal from the vacuum. The scheme of the experiment is in Figure 22.

The detector used during all co-sputtering experiments was Pilatus 1M. The frame rate was optimised while performing these experiments and was kept to 10 frames per second in most cases, which allowed both the detection of small changes as well as ensuring a sufficient signal. The detector location covered the range in q_y from -1.8 to 2.5 nm^{-1} for the samples deposited at room temperature and from -1 to 1.5 nm^{-1} for the annealed samples. This choice was influenced by the expectations of clusters forming larger

sizes having an extra kinetic energy from heating and thus the latter resolution is better. The X-ray photon energy was 13 keV which corresponds to a wavelength of 0.0953 nm. To reduce the possibility of radiation damage a scanning motion of around 1.5 mm was done. The motion range was chosen in the centre of the Si wafer and its area checked for homogeneity. When the deposition was finished, an XRR scan was performed to estimate the resulted thickness (see in Appendix: Section 5.5).

2.2.4. Investigation of Au_n.

Results from two experiments on the investigation of ultrasmall size-selected clusters are included in this work. Although both experimental arrangements employed GISAXS and XRF simultaneously, some differences existed. Due to the fact that sample 1AU1 contains neither ultrasmall nor size-selected clusters, and was tested for comparison, it did not require complicated setups and the scheme is not presented here.

Prior to every experiment where XRF detector (Vortex®-EM, Hitachi Inc.) was used the calibration was made by X-ray emission lines of foils of Ag, Tb, Rb, Mo, Cu and Ba and covered an energy range up to ~14.6 keV in 2048 channels. Example of the calibration is provided in the Appendix: Section 5.2.

The experimental setup of the first one is presented in Figure 23 (results of this work are published[132]). This sketch is an artistic representation of the real experiment; the real arrangement is presented in Figure 23**b**.

The sample to the detector distance was 2.368 ± 0.002 m for samples 1AUSL1 and 9AUSL1 and also for the 1AU1. The photon energy for the first two was 13 keV, while for 1AU1-11 keV. The Pilatus 1M detector was used for GISAXS measurements, while Pilatus 300K -for GIWAXS. Simultaneously with scattering measurements, a Vortex detector was used to measure emitted X-ray fluorescence. As in the co-sputtering experiment, the incident angle was higher than the critical angle of both gold and silicon and was kept 0.45 – 0.5° for all three, which allowed to have the beam footprint covering most of the substrate surface. Lateral scanning was performed along a distance of 7 mm with steps of 0.1 mm for the monoatomic deposited sample with 50% ML to localise the relative position of the cluster spot to the Au markers. For the sample of Au_9 with 10% ML material, 4 mm of the scanning distance has been covered according to the preceding scanning experiment. Several repetitions (>50) were made to increase the signal to noise ratio. The exposure time for each step was not exceeding several seconds on each spot during scanning to avoid beam induced effects[141] and to prevent detector saturation[137].

All the samples had a low scattering volume of the material deposited on the surface, which did not exceed 50% ML of gold and most of them had only 10% ML coverage. This produced certain complications with XRF measurements, which requires sensitivity to these very low quantities, but should not be saturated because of the marker thickness (more than 300% ML). Therefore, in the next experiment (the second experiment was performed 18 months after the first), marker thickness was

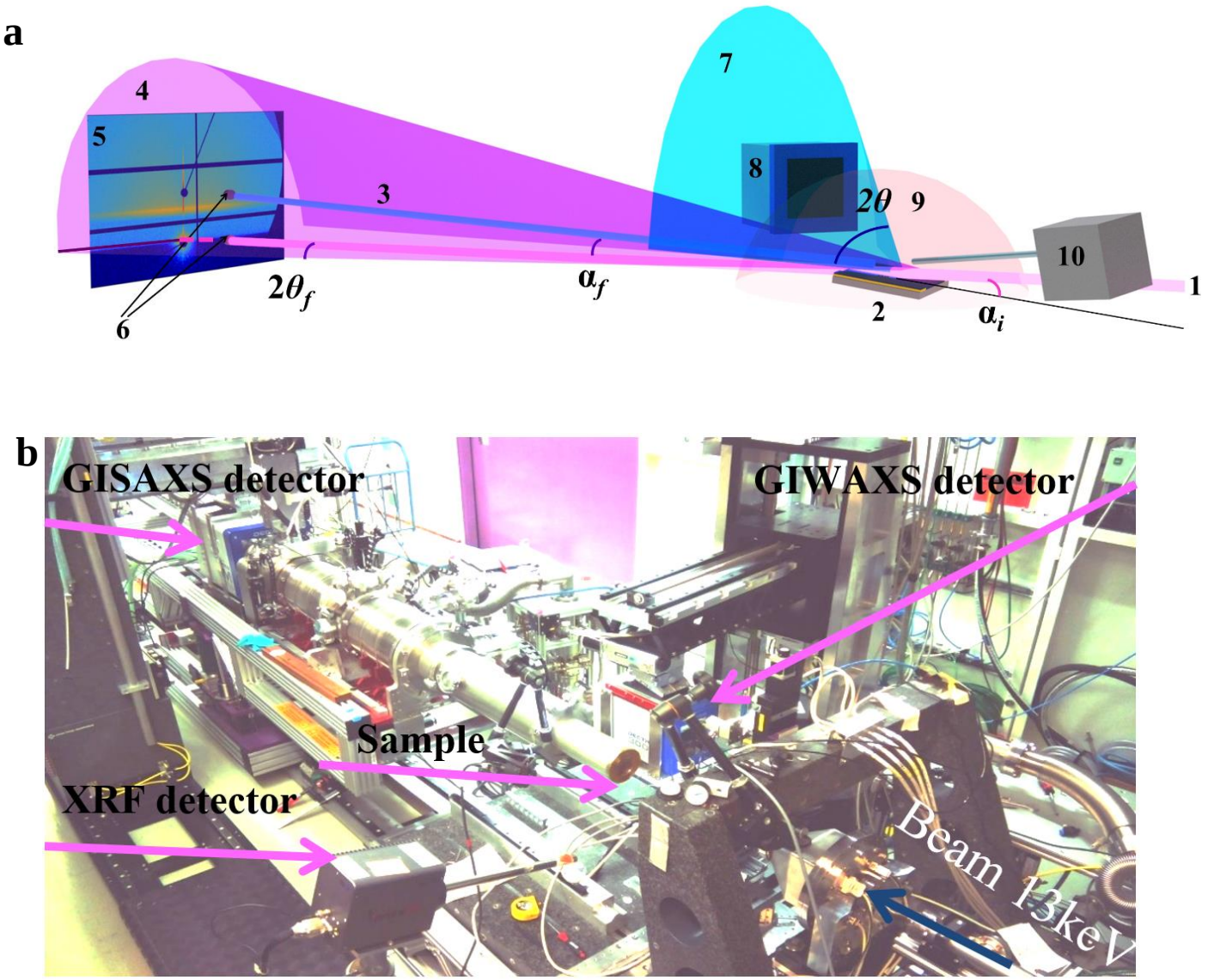

Figure 23: a) Scheme of the *ex situ* scattering experiment on ultrasmall size-selected Au clusters №1. 1. Synchrotron X-rays. 2. Sample with Au clusters or adatoms. 3. Beam reflected from the sample. 4. Small angle intensity distribution. 5. Resulted GISAXS pattern on the detector Pilatus 1M (Dectris). 6. Beamstops: primary (bottom), specular (top). 7. Wide angle intensity distribution. 8. GIWAXS detector Pilatus 300K (Dectris). 9. X-ray fluorescence from the sample. 10. X-ray fluorescence spectrometer Vortex. Angles shown in the scheme: α_i – incident angle between the X-ray beam and the sample surface, which is <1°; α_f – exit angle in GISAXS ; $2\theta_f$ – out-of-plane angle in GISAXS; 2θ – exit angle in GIWAXS.[132] b) Photo from the corresponding experiment. (Viewpoint is slightly different from in the sketch).

around 150%ML and the Vortex detector was precisely adjusted, being mounted on a crane. The optimal position was found and the setup arrangement is presented in Figure 24.

During this experiment, only GISAXS (Pilatus 300K) and the XRF (Vortex) detectors were used simultaneously. Previous studies using GIWAXS did not provide sufficient information (see Appendix: 5.3) and only one scattering detector was available. Therefore, the GISAXS detector was installed on the minimum possible SDD of 1.489±0.002 m to cover the biggest possible q_y range (0 to 3.5 nm^{-1}).

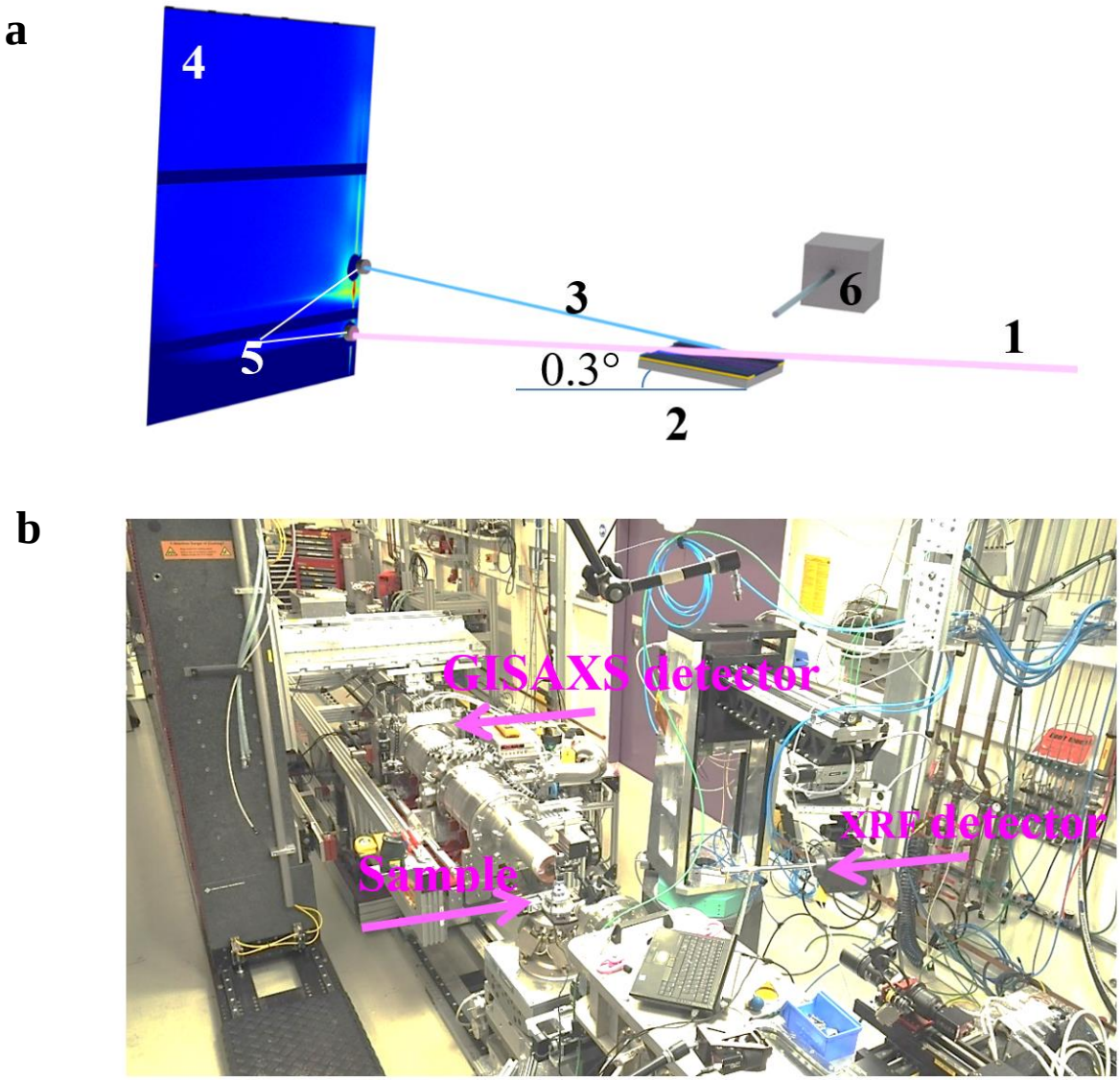

Figure 24: Scheme of the *ex situ* scattering experiment on ultrasmall size-selected Au clusters №2. a) 1. Synchrotron X-rays. 2. Sample with Au clusters or adatoms. 3. Beam reflected from the sample. 4. Resulted GISAXS pattern on the detector Pilatus 1M (Dectris). 5. Beamstops: primary (bottom), specular (top) 6. X-ray fluorescence spectrometer Vortex. b) Photo from the corresponding experiment.

This arrangement was dictated by such considerations: the smallest possible length of the flight tube was reached and previous experiments proved the need to resolve signals coming from very small sizes in the real space (therefore, large q_y range needed in the reciprocal space). Incident beam with photon energy of 12.8 keV and the same size of 20 x 30 μm² (H x V) under an incident angle of 0.32° was used. Keeping the incident angle so close to the critical angle of Au allowed a very high sensitivity to the signal from gold. All samples were precisely aligned in height before starting the scan. Lateral scanning of the surface with exposure of 1 s on each point and steps of 0.1 mm was performed. Considering possible radiation changes, it was decided to make several repetitions of such scans on the same positions (>50). This was important since a single repetition did not contain enough signal intensity to reveal the structure features both in XRF and GISAXS. Therefore, the possibility to sum several scans

was necessary. The scanning area was chosen to cover a large area of the sample, because the spot where ultrasmall clusters were deposited was expected to be in the centre of the substrate.

2.2.5. Dimensionality reduction using PCA

In this work, Principal component analysis (PCA) was applied on the experimental GISAXS data to confirm that even when data is decorrelated, the signal coming from the structure is still in the corresponding place. This was necessary due to the low signal to noise ratio. An example is provided in Section 3.2.6.

As early as in 1901 it was proposed by K. Pearson: "In many physical, statistical, and biological investigations it is desirable to represent a system of points in plane, three, or higher dimensioned space by the "best-fitting" straight line or plane."[142] His method was applied to scientific problems, it has transformed and been rediscovered several times and finally is now known as PCA. Now, it is a statistical technique used for dimensionality reduction of large datasets. It reduces contained information to a few common uncorrelated components. This increases interpretability with minimum information loss[143]. The main concept is to maximise variability of the data, which will be decorrelated at the same time[144]. Mathematically, this is done by finding for the data the new coordinate system, onto which data is projected to minimise the projection error. This is where the greatest variance lies - the first principal component (usually containing at least 80% of the variance). Then the second biggest variance lays along the second component. There can be more principal components, but the amount of them should be lower than the amount of initial variables.

Procedure of working with PCA

The procedure of applying PCA on the example of 2D data (Figure 25) is taken from the lectures and homework of Machine learning course[145] by Prof. Andrew Ng (Stanford):

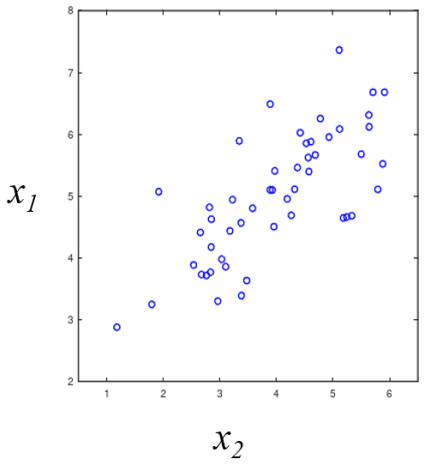

Figure 25: Example 2D dataset

1) Data is normalised by subtracting the mean value of each variable (later in the text can be referred as a feature) so that the data is scaled.

2) The covariance matrix is computed, which is given by:

$$\sum = \frac{1}{m} X^T X,$$

Equation 19

where X is the data matrix with examples in rows, and *m* is the number of examples; Σ is an n x n matrix. (X consists of x_1 and x_2 after normalisation- subtraction of the mean of the data)

3) Then using singular vector decomposition (SVD) Σ is decomposed into [USV^T]. There U is an orthonormal matrix which contains principal components (or eigenvectors) of X^T , V is also the orthonormal matrix (contains eigenvectors of the matrix X^TX). S a diagonal matrix and contains the square roots of the eigenvalues of XX^T and X^TX. Computed eigenvectors are shown in Figure 26.
4) These two principal components (eigenvectors) can be then used for the dimensionality reduction (in this case projecting 2D to 1D). In Figure 27 is shown how the initial data set is projected on two principal components.

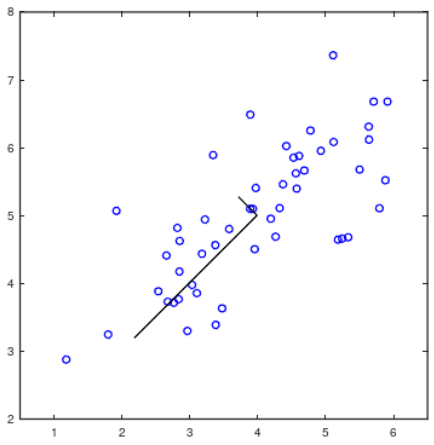

Figure 26: Computed eigenvectors of the dataset. Long black line- first principal component, which contains the maximum variance between the data. The shorter one is the second maximum variance vector.

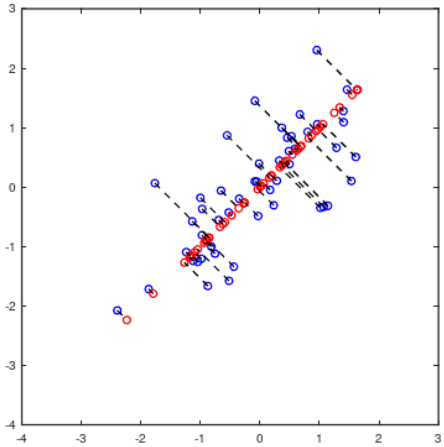

Figure 27: The projected data after PCA. Red dots –projected data points.

Due to many applications where PCA can be used, it is not required to perform such a procedure as described above. For example, Python and R already have libraries with PCA implemented. With Python it is possible to use different toolkits as Pandas[146,147] library or Scikit[148,149] together with Pandas to call the function PCA.

3. Experimental results and discussion.

This chapter is divided in two parts, where the analysis results of bimetallic small clusters Au/Ag and ultrasmall clusters of Au_n (n=5, 7, 9, 11) are presented. In both cases, GISAXS was the main method of investigation and the main output is the obtained radii and the interclusteral distances.

3.1. Au/Ag bimetallic clusters

In this Section, real-time investigation of the morphology of co-sputtered Au and Ag clusters is presented. It is also compared with pure metal deposition in the same conditions and co-sputtering of these metals while heating.

Bimetallic clusters, especially of noble metals are considered to be promising candidates for various novel technological applications[64,150,151]. Therefore, it is important to have a precise method for synthesis of AuAg nanostructures for industrial applications. For such purposes, RF-Magnetron sputtering with two targets is a promising candidate. Close observation of real time cluster growth in these systems is of a great importance, and GISAXS analysis with synchrotron radiation can provide information about real time growth of nanostructures right from nucleation.

In this work the focus is on the geometrical shape of these clusters during deposition, however optical properties of such clusters and their differences from pure metals are also briefly discussed.

The preparation conditions are listed in Table 2, while detailed procedure is provided in Section 2.1.2.1. Since the sample to the detector distance (SDD) was varied, in the table below the used values are given. Pure metallic Au and Ag samples were prepared with the rate of 0.005 nm/s, which also applied for the alternate deposited samples with pure Ag deposition followed by pure Au (AuonAg). Bimetallic AuAg had a deposition rate of the deposition sum of two metal having 0.005 nm/s each. Addition of "A" at the end of the sample name indicates a temperature of 185 °C applied during the deposition.

Sample name	Au deposition rate [nm/s]	Ag deposition rate [nm/s]	Deposition time [s]	Temperature during deposition °C	SDD [mm]
Au	0.0053	n/a	1876	21	2431
AuAg	0.0095		1050	21	2431
AuonAg	0.0050	0.0051	992+984	21	2431
Ag	n/a	0.0051	1968	21	2431
AuAgA	0.0093		1074	185	4161
AuonAgA	0.0050	0.0050	995+995	185	4161

Table 2: Samples prepared and investigated during co-sputtering of Au and Ag.

In Figure 28, GISAXS patterns at different deposition stages are shown. Comparison of these four types of real-time deposition is done at the effective thicknesses 1 nm, 5 nm, 10 nm (final thickness). Similarities in the shape of the signal for all of the samples are observed, which mean that at the

beginning of the deposition their shapes were similar, although the relative position (from the primary beam) of the signal indicates bigger cluster sizes for Ag. For each sample, the shape of the signal still has common features at 5 nm, but at 10 nm all samples shows significant difference in the GISAXS data. Interestingly, there is a certain resemblance of features between Au and AuAgA, while AuAg and Ag also look similar to each other. As it has been demonstrated[31] that deposited gold has a hemispherical shape in close conditions (both with the experiment and simulation), it seems highly probable that both Au and AuAgA clusters are hemispheres at 10 nm. At the same time, Ag has shown to be cylindrical already at 7.6 nm[152], and the patterns resemble those in the present work. Therefore, they show a tendency to form cylinders or ellipsoidal shapes. This can be an indication that the shape of AuAg clusters prepared at room temperature is highly influenced by Ag growth behaviour, whereas shape formation while heating even to as low as 185 °C is affected by Au metal growth.

In Figure 29, contour plots of the out-of-plane cuts (along q_y) are shown extracted at the Si Yoneda peak depending on the effective thickness. The position of the cut made is demonstrated in Figure 22, where the lavender line at 6 is the Si position. The deposition rate of each sputtering target was kept constant, therefore the desired 10 nm thickness was reached faster while co-sputtering. That is why, for consistency, time dependency was replaced by the effective thickness. These plots exhibit similar features. Initially until a thickness of 3 nm, all of them have a rather wide distribution of sizes (indicated by the wide wing shape), which at the same time lay in the bigger q_y-range (small size structures in the real space). As the thickness increases beyond 3 nm, a decrease in size distribution is observed while the size of the clusters increases. This represents cluster growth in the real space.

The positions of the maxima of such out-of-plane (Yoneda) cuts can be fitted with Lorentzian or Gaussian function as described in Section 2.2.2, where interparticle distance D and radius R can be calculated with Equation 17 and Equation 12, respectively. Temporal evolution of radii and fitting positions for all of the samples has been discussed below, after the simulation results.

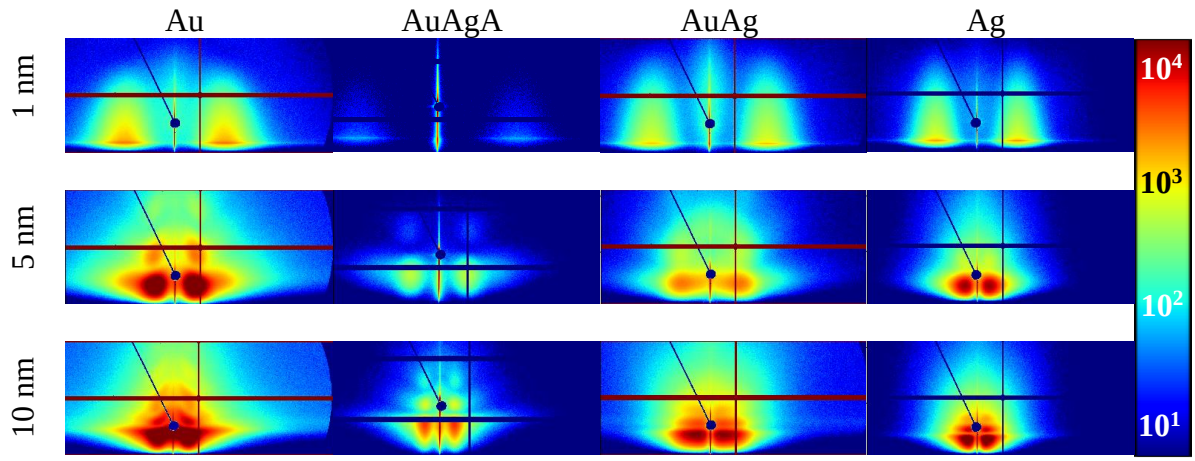

Figure 28: Evolution of the GISAXS pattern depending on the effective thickness of sputtered materials

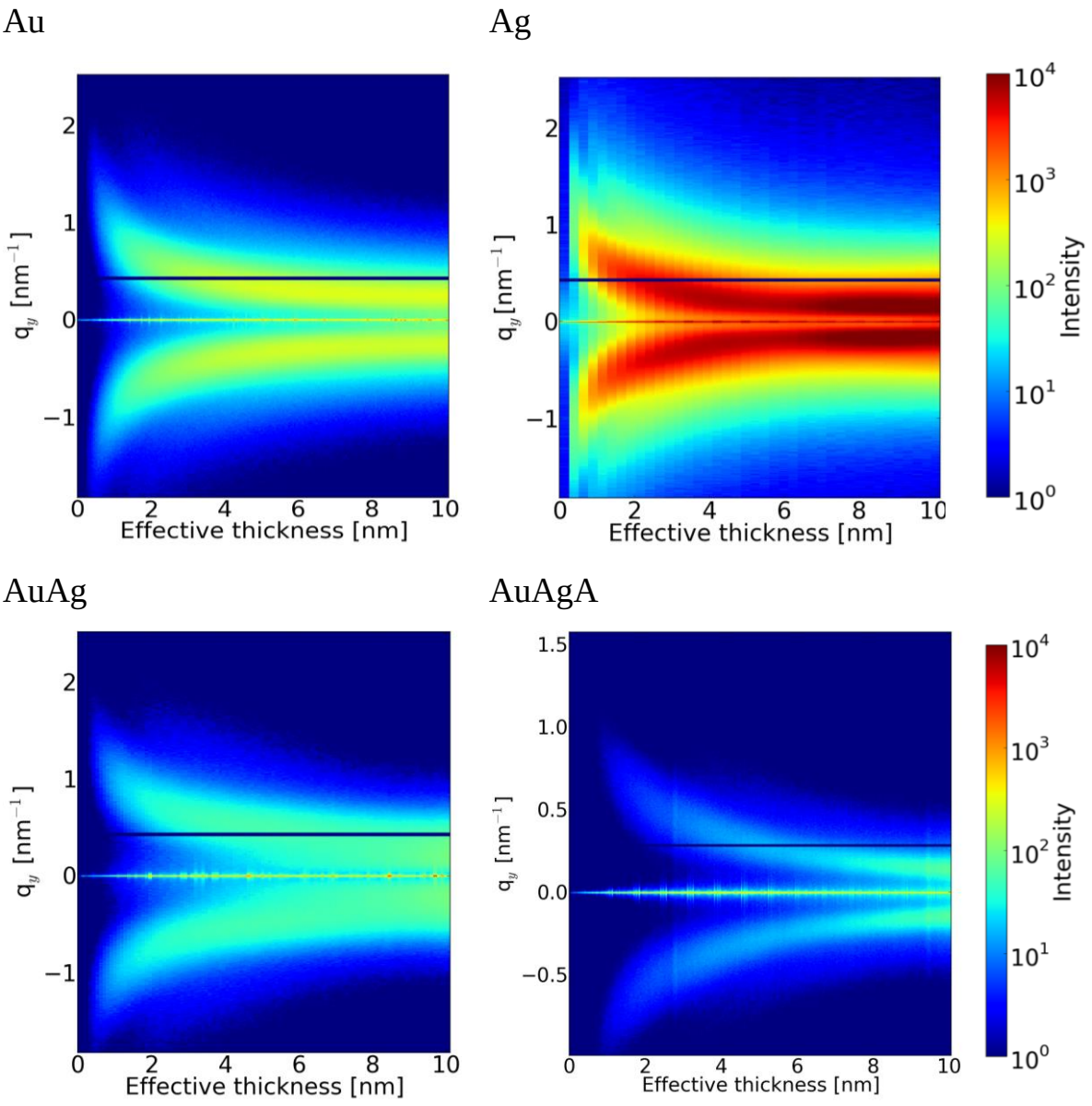

Figure 29: Temporal evolution of intensity (along q_y) derived at the Si Yoneda peak (q_z=0.65 nm^{-1}) during deposition for Au, Ag, AuAg and AuAgA.

3.1.1. Simulations using IsGISAXS

Simulations were done using IsGISAXS (version 2.6)[140], and an example of the simulation input file used is provided in the Appendix: Section 5.9. The framework was "Distorted Wave Born Approximation for supported islands"[117,140], and all the parameters were adopted to the experimental ones. The index of refraction of the substrate and materials were table values[153], while for AuAg and AuAgA this value was estimated as for the compound material with the density of 14.9 g/cm^3 [153]. The obtained radii and interparticle distances are listed in Table 3, several different form-factors provided in IsGISAXS were used (sphere, cylinder, anisotropic hemispheroid, ellipsoid, triangular prism, pyramid, hexagonal prism and cone-some illustrations are featured in Appendix: Section 5.10).

Thickness [nm]	Parameters [nm]	Au	AuAgA	AuAg	Ag
1	R	2.8	3.0	2.6	3.2
	D	7.3	8.0	6.4	9.1
5	R	8.8	10.0	7.5	12.0
	D	18.2	21.9	14.4	29.0
10	R	13.8	20.2	13.5	18.2
	D	25.1	44.6	24.4	38.1

Table 3: Experimentally obtained parameters, used for simulations with IsGISAXS (R-radius, D-interparticle distance).

It should be noted that simulations were used to describe geometrical shapes only, no quantitative analysis was performed.

Figure 30 – 33 display the detector images vs corresponding simulations of Au, Ag, AuAg and AuAgA respectively. It can be seen that the simulated patterns have more features than the real data, which can be expected due to the experimental resolution (and because of limitations of the models used to solve the problem of the structural factor). These possible secondary and higher order signals would be seen for isolated particles[154], but the concentrated systems introduce a smearing of the signal. Additionally, simple shapes cannot always fully represent real structures.

Simulated patterns were compared to the experimental data and a good agreement with simulated structures was found, which show the experimental result can be described as anisotropic hemispheroid (AHS) and ellipsoid (Ell) structures (illustrated in Figure 34). From the simulation an obtained nanostructure shape in case of Au, AuAgA was hemispherical, while for Ag and AuAg flattened ellipsoidal.

Note: colour scheme was adjusted for better visibility; IsGISAXS program failed to simulate the whole pattern but the relative pixel positions of height modulations matches the experiment.

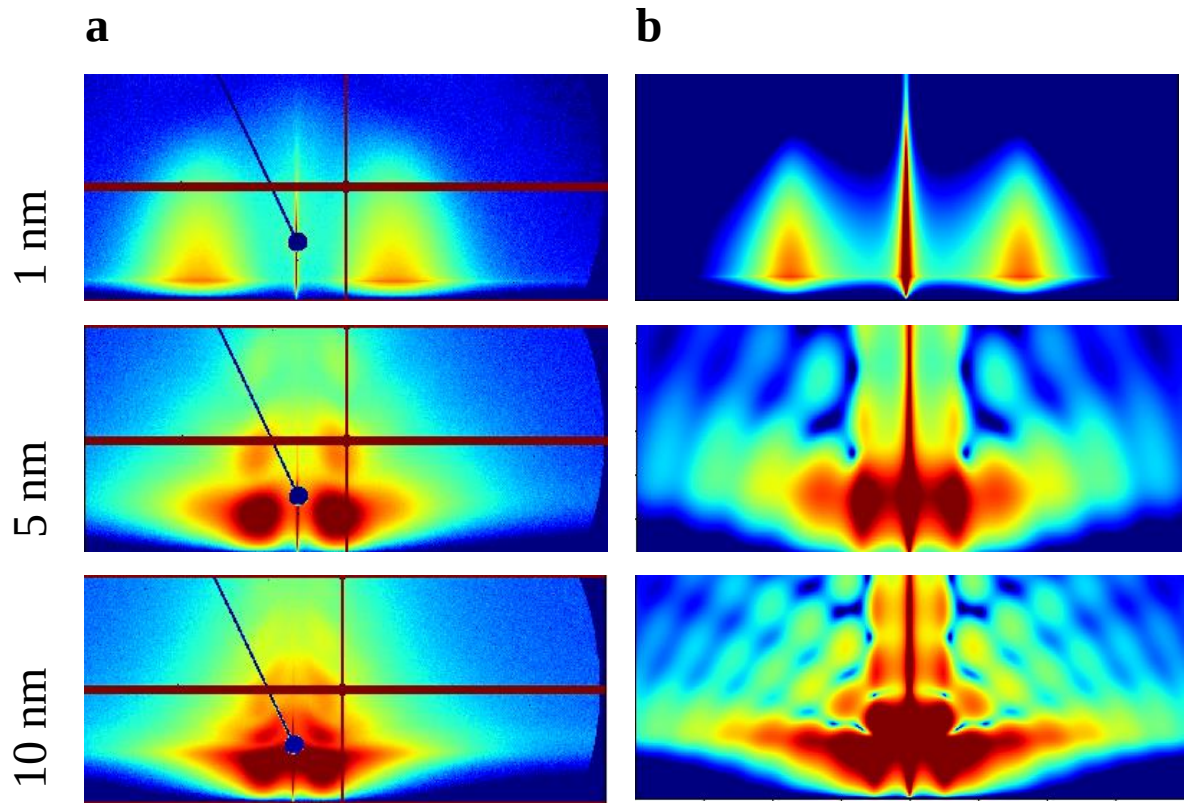

Figure 30: (a) 2D GISAXS detector images and (b) corresponding simulations for different effective thicknesses of Au.

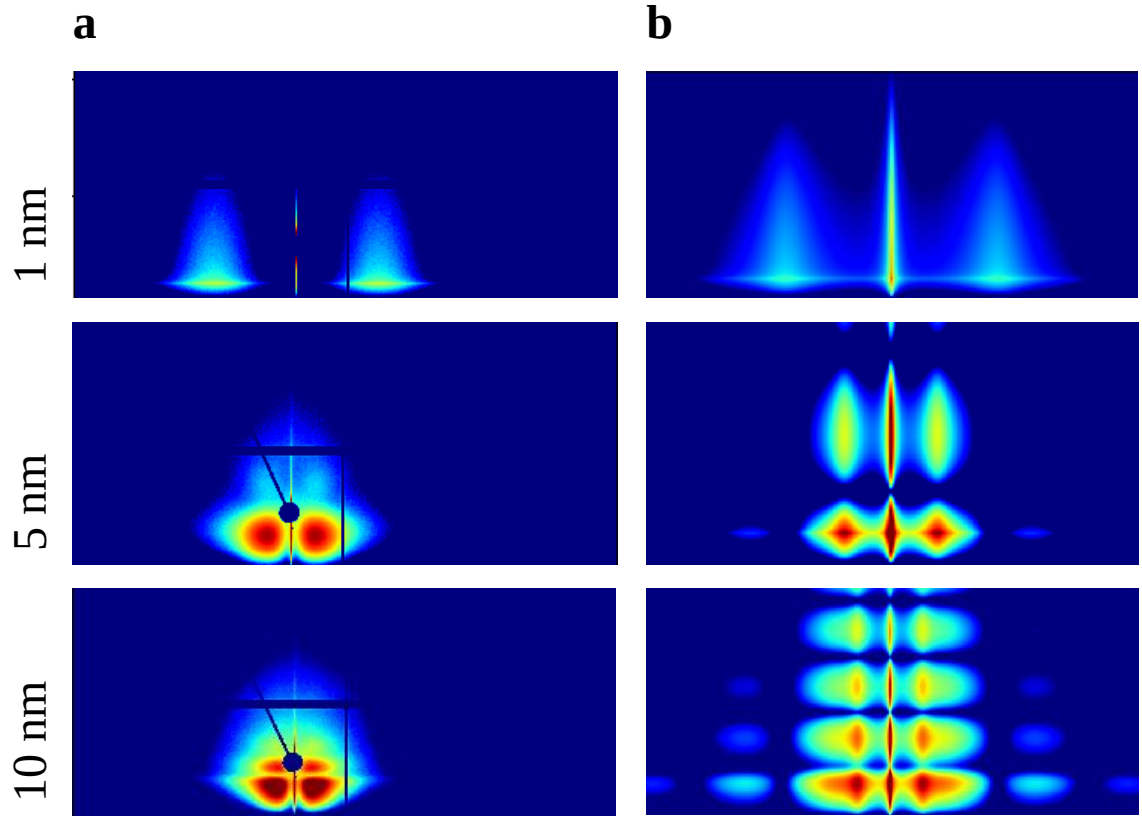

Figure 31: 2D GISAXS detector images (a) and corresponding simulations (b) for different effective thicknesses of Ag.

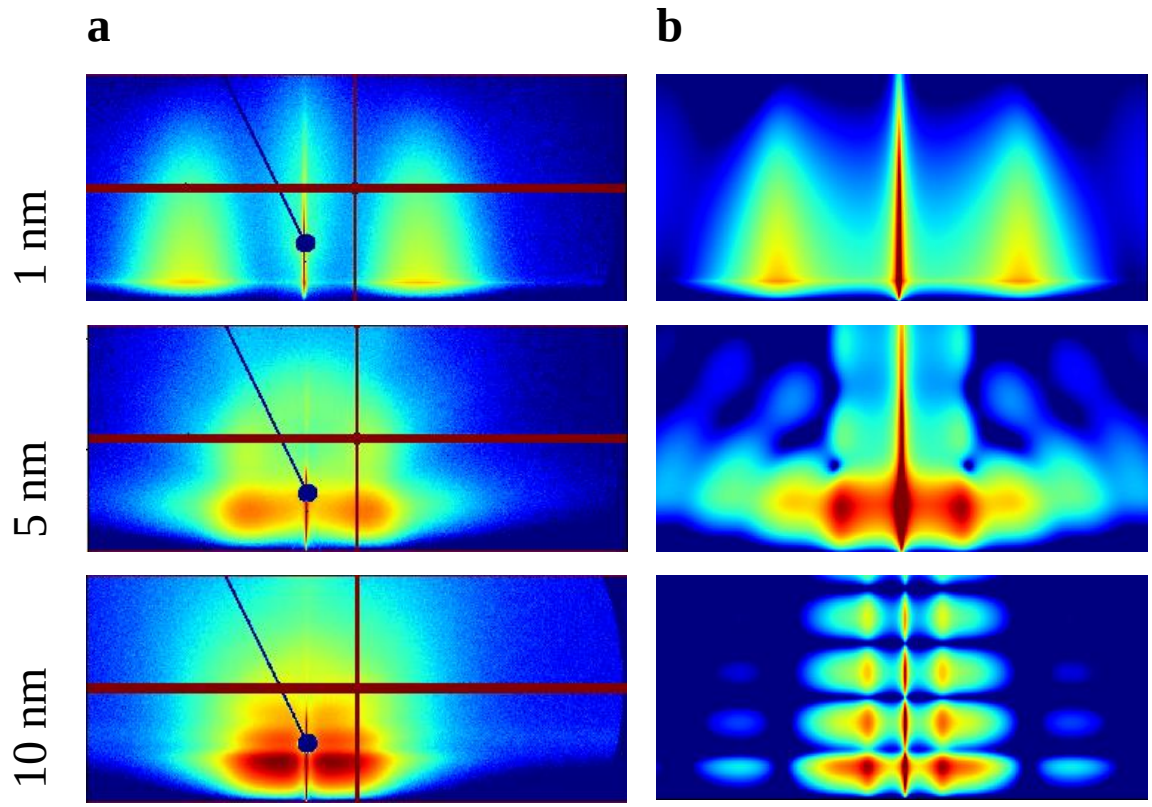

Figure 32: 2D GISAXS detector images (a) and corresponding simulations (b) for different effective thicknesses of AuAg.

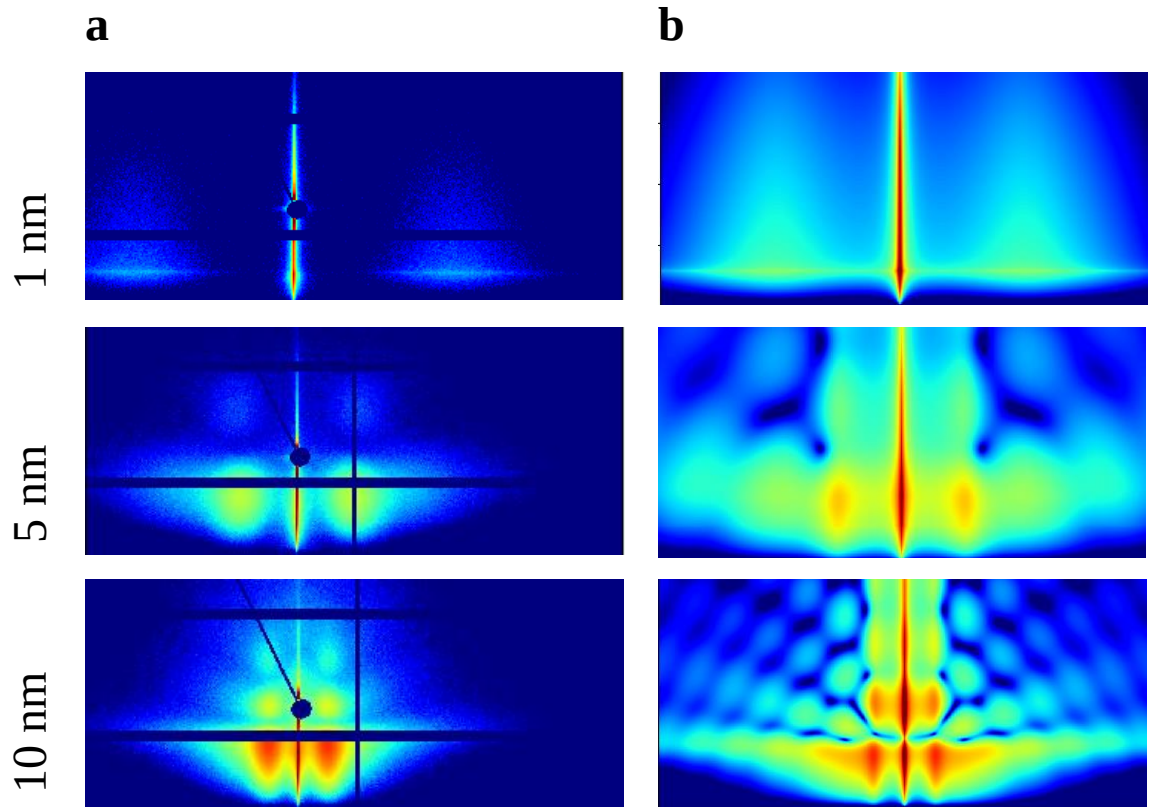

Figure 33: 2D GISAXS detector images (a) and corresponding simulations (b) for different effective thicknesses of AuAgA.

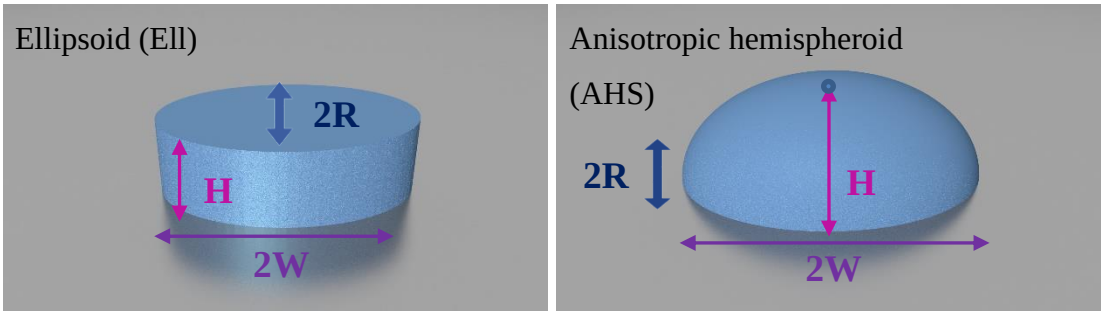

Figure 34: Two most suitable form-factors describing experimental GISAXS patterns.

These simulations can provide knowledge of the ratio between radius, height and width of the structure. Table 4 shows the ratios and form-factors that were best describing the real system. It can be seen that the previous assumption of AuAg and Ag showing tendency to a flatter structure; and Au and AuAg to be closer to a hemisphere in shape still apply.

Thickness [nm]	Parameters	Au	AuAg	AuAgA	Ag
1	Form-factor	AHS	AHS	AHS	AHS
	H/R	1.5	1.3	1	1
	W/R	1	1	1	1
5	Form-factor	AHS	AHS	AHS	Ell
	H/R	1.1	1.2	1	0.7
	W/R	1	1	1	0.7
10	Form-factor	AHS	Ell	AHS	Ell
	H/R	1.1	1.3	1.1	1.7
	W/R	0.9	0.35	1	1

Table 4: Geometrical parameters of form-factors matching the experimental detector images for Au, Ag, AuAg and AuAgA.

3.1.2. Quantitative analysis during cluster growth.

To identify exact positions of lateral maxima ($q_{y,max}$) fitting was performed. In Figure 35 temporal development of $q_{y,max}$ positions is shown, these positions were obtained using the Lorentzian fit. These values are presented with the fit error, which shows that while the effective thickness is lower than 1 nm, it is difficult to obtain a pronounced and reliable signal from the structure. After this point the error is lower, which means that it should be possible to estimate the geometrical structure of growing clusters at every moment of the deposition.

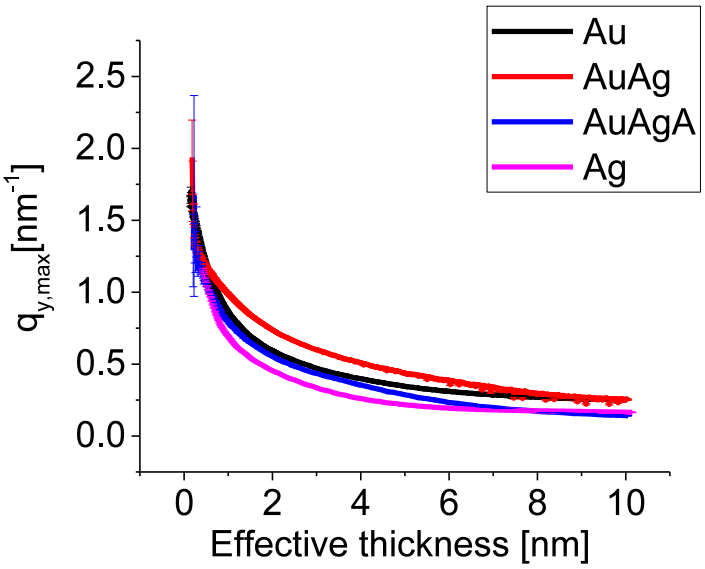

Figure 35: Temporal evolution of the Lorentzian fitted Si Yoneda cuts for Au, AuAg, AuAgA and Ag.

As discussed in Sections 2.2.2 and 1.3.1.3, $q_{y,max}$ positions have been used to estimate interparticle distance and their respective radius. The final effective thickness of 10 nm was also confirmed with XRR analysis (results provided in the Appendix: Section 5.5), which was done directly after the deposition. The resulting calculated radius dependency from the effective thickness is shown in Figure 36. According to this graph, the resulting clusters of Au and AuAg have a similar radii size of about 13 nm, while Ag and AuAgA have much larger radii, around 20 nm.

The percolation threshold (2R/D=1) was also estimated for these systems using the approach of Schwartzkopf *et al*.[31] and the results are presented in Figure 37. It is clearly visible that AuAg is reaching percolation at around 3 nm, while pure Au only reaches percolation at 6 nm of the effective thickness. Both pure Ag and AuAuA seem to require higher effective thickness to reach this threshold.

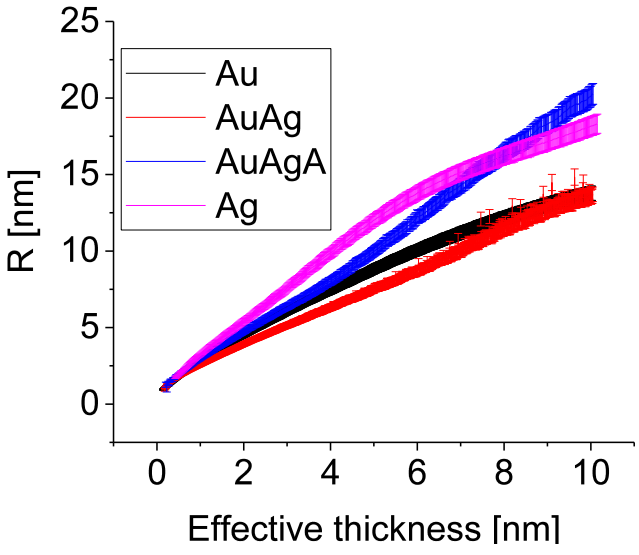

Figure 36: Radius dependency from the effective thickness of the deposited material.

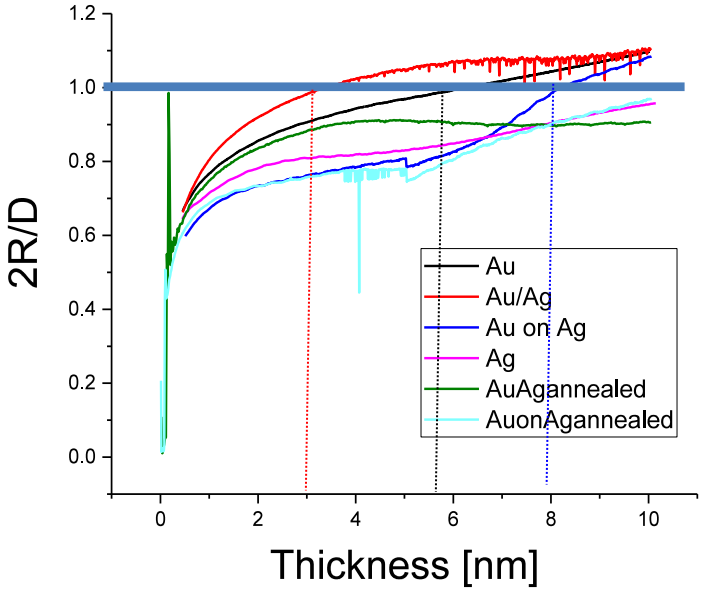

Figure 37: Ratio of 2R/D during deposition. Percolation threshold is reached when the blue line at 1 (2R/D) is crossed.

The expected cluster growth stages at 1, 5 and 10 nm are shown in Figure 38. This sketch illustrates the tendency of co-sputtered AuAg to percolate on the early stages, while even very large clusters of AuAgA and Ag do not show signs of percolation. Au shows similar behaviour to that proposed by Schwartzkopf et al[31] and percolates between 5 and 6 nm.

The pure gold percolation threshold occurred at 5.5 nm effective thickness as was reported by Schwartzkopf et al[31]. In his work the deposition rate was kept much higher (0.1 nm/s) than in the present work. At the same time, the reported percolation for Ag does not occur, which for similar conditions was at 5.7 nm^{-1} with rate of 0.015 nm/s[30]. Therefore, one can assume that the deposition rate of silver plays a bigger role in the formation of the final structure than for gold. What is also in agreement with the previous work is the growth kinetics[31], since one can observe the nucleation happening in Volmer–Weber mode. However, for the four samples discussed here, the grain growth stage happens at a different effective thickness and bimetallic AuAg has it the earliest. Afterwards, when the percolation is reached, from simulations it seems that island shape of AuAg changes from hemispherical to ellipsoidal. Which might be the influence of Ag in the system, which was reported to have truncated sphere island shape change to cylinders upon surpassing the percolation threshold[152]. In the present experiment, Ag also shows a tendency to form flattened structures rather than spherical after certain amount of material was deposited.

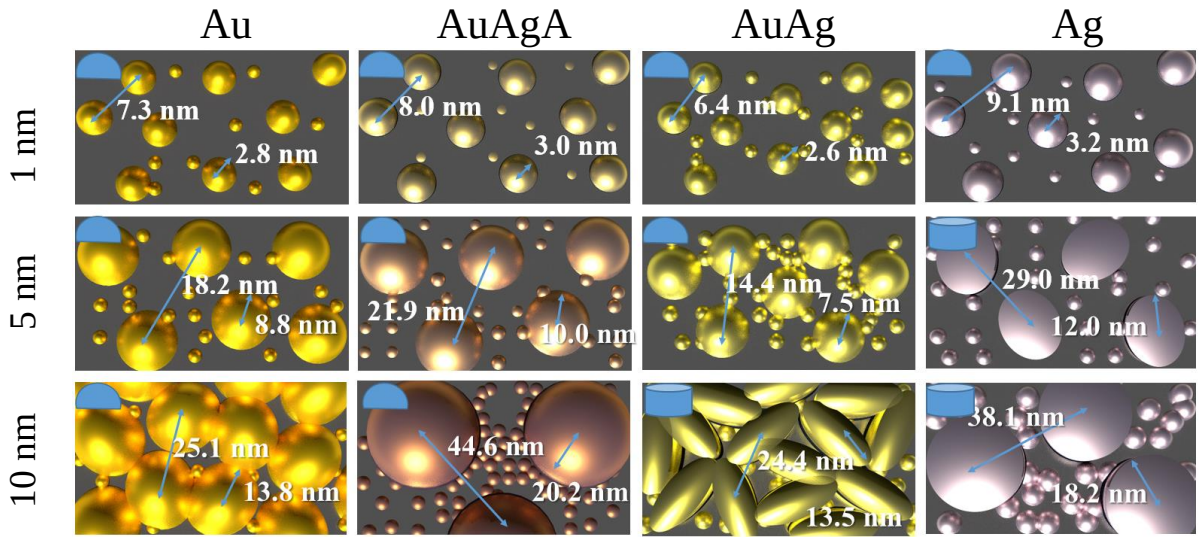

Figure 38: Sketch of the cluster growth for Au, AuAgA, AuAg and Ag at 1, 5 and 10 nm of effective thickness. Note: these images are schematic and represent an artistic view.

To summarise, it has been found with both simulations and quantitative analysis using GISAXS, that co-sputtered AuAg inherit cluster size from Au influence and the shape from Ag. Heating even to rather low temperatures (180 –190 °C) changes both the size and the shape of the resulted structure. Heating of AuAg seems to repel clusters from each other, but at room temperature they percolate even at low thicknesses.

3.1.3. Optical properties of AuAg.

Reflectance was tested collecting UV characteristics during deposition. The relative reflectance of the final 10 nm is shown in Figure 39. In all the data, substrate signal was subtracted, and normalised such that 100% of signal refers to the Si signal. Here the co-sputtered sample also exhibits an interesting feature: AuAg shows an intense reflectance in wavelength range 400 – 800 nm, much higher than that observed in pure metals.

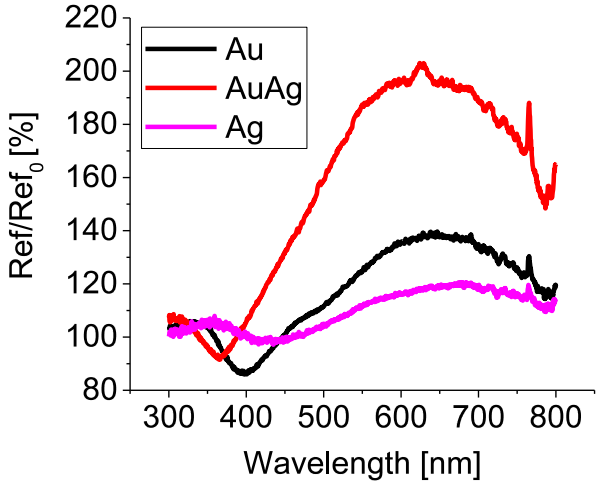

Figure 39: UV/Vis reflectance for 10 nm effective thickness..

3.1.4. Geometric structure of AuonAg and AuonAgA.

Alternate deposition of 5 nm gold on the deposited 5 nm of silver was performed at room temperature and during heating. These samples (AuonAg and AuonAgA) were produced to demonstrate which differences occur when compared to co-sputtered samples.

The intensity maxima obtained by fitting is shown in Figure 40, where it is presented as a function of the effective thickness. For both heated and room temperature deposition the position of $q_{y,max}$ shows similar tendency to decline till silver deposition stopped at 5 nm. This corresponds to the expected cluster growth, monitored *in situ*. Then both of them have a jump to even smaller q_y values, which corresponds to even bigger cluster sizes. This is probably caused by the postdeposition growth, which happened during 20 min before the other sputtering could be started. When the gold deposition starts, size differences between AuonAg and AuonAgA became much more pronounced.

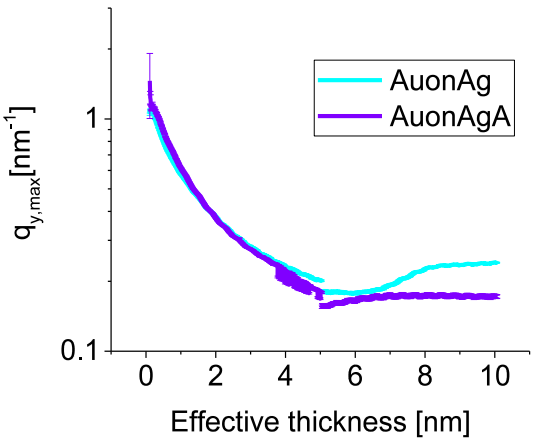

Figure 40: Temporal evolution of the Lorentzian fitted Si Yoneda cuts for AuonAg and AuonAgA.

The radii for these systems were also estimated, using the hemispherical model (Section 1.3.1.3) and shown in Figure 41. The obtained radius of AuonAgA is close to that of pure silver and is around 18 nm, while the one of AuonAg is close to the one after pure gold deposition.

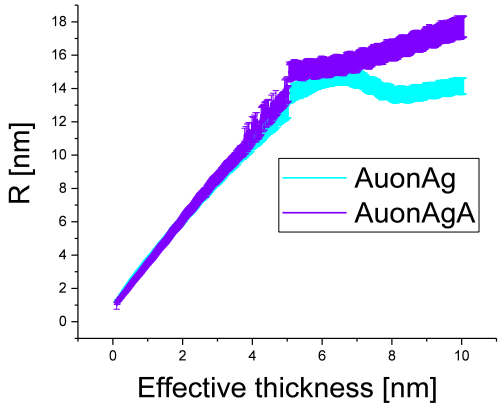

Figure 41: Radius dependency from the effective thickness of the deposited material.

3.2. Ultrasmall size-selected Au clusters

Ultrasmall gold clusters, deposited on oxide surfaces have been of high interest to scientists for the last decades. While nanoclusters with hundreds and thousands of atoms, discussed in the previous subchapter, have a different structure and properties than materials in bulk, ultrasmall clusters (those with 5 – 20 atoms) can also exhibit variance from both. Geometrical structure is closely connected to the physical properties in such systems with only a few atoms, therefore it is of high importance to determine this for each system.

In this chapter the measured properties of ultrasmall size-selected Au_n (n=5, 7, 9, 11) clusters and adatoms are presented. The main focus of the research was the geometrical structural investigation of such clusters, using GISAXS in combination with fluorescent spectroscopy. The correlation between the number of atoms in different clusters and their size was examined.

Firstly, measured samples and the analysis routine are discussed. Then the data and the analysis of each cluster size is presented. Afterwards PCA application on the example of Au_{11} is explained. Finally, radiation induced changes and aggregates are discussed.

3.2.1. Sample overview and the analysis routine.

All samples, except for 1AU1 were prepared in the same conditions, using ICARUS cluster source. Their preparation steps were described in Section 2.1.2.3 and Table 1 shows the different parameters used in synthesising each sample. Some of them like 1AUSL1, 9AUSL1 and 1AU1 were the first successful measurements of such ultrasmall structures and the results are published[132]. They had slightly different experimental conditions, which were described in Section 2.2.4 and Table 1 is reproduced below. Despite these differences, one can calibrate and compare these samples during the analysis. Note that negative numbers in this case, when q values are discussed are equal to the positive ones and only depend on the lateral position of the detector from the beam (maximum, which is visible at q_y=-1nm^{-1} also exists at q_y =1nm^{-1}).

Sample name	Atoms in cluster	Coverage [% ML]	Soft-landing	Capping layer	Au markers [number]	Marker thickness [nm]
1AUSL1	1	50	+	+	2	10
1AUSL2	1	10	+	+	1	5
1AU1	1	50	–	–	0	0
5AUSL1	5	10	+	+	0	0
7AUSL1	7	10	+	+	1	5
9AUSL1	9	10	+	+	1	10
9AUSL2	9	10	+	+	0	0
11AUSL1	11	10	+	+	1	5

Table 1: Samples prepared using the ICARUS cluster source.

Sample name	SDD [mm]	Energy [keV]	Angle [deg]	XRF	Detector
1AUSL1	2368	13	0.45	+	Pilatus 1M
1AUSL2	1488	12.6	0.32	+	Pilatus 300K
1AU1	2366	11	0.42	–	Pilatus 1M
5AUSL1	1488	12.6	0.32	+	Pilatus 300K
7AUSL1	1488	12.6	0.32	+	Pilatus 300K
9AUSL1	2368	13	0.50	+	Pilatus 1M
9AUSL2	1488	12.6	0.32	+	Pilatus 300K
11AUSL1	1488	12.6	0.32	+	Pilatus 300K

Table 5: Experimental conditions during GISAXS experiments on ultrasmall clusters. (SDD-sample to the detector distance)

Figures used for the analysis

In the following analysis for all samples (except for 1AU1) such plots and figures were used and provided:

1) XRF yield depending on the scanning position done at L_α line of gold (9.6 keV[155]). High intensity signal in the area starting at 8 mm is from the Au marker, bell-shaped signal in the middle (3–6 mm) is from the spot of deposited ultrasmall clusters.

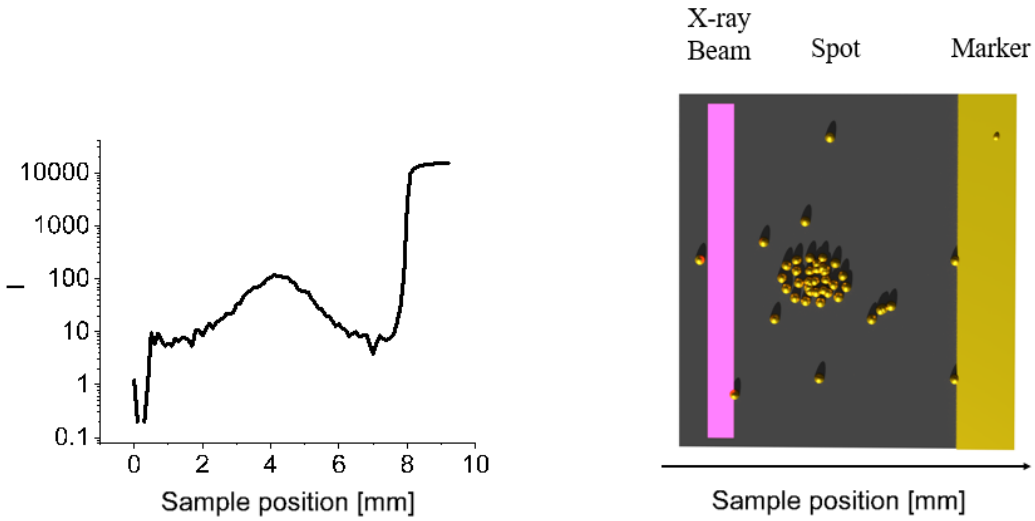

Figure 42: Example of the XRF profile at the L_α line of gold with the drawing of the sample surface. The X-ray beam (pink line is a beam footprint) moves horizontally over the samples.

2) XRF yield depending on the photon energy for certain positions: Spot position, Si (substrate signal of this sample, this position was used for the background subtraction in examples below (3), 4), 5), 6)) and Au marker (if it exists on the substrate).

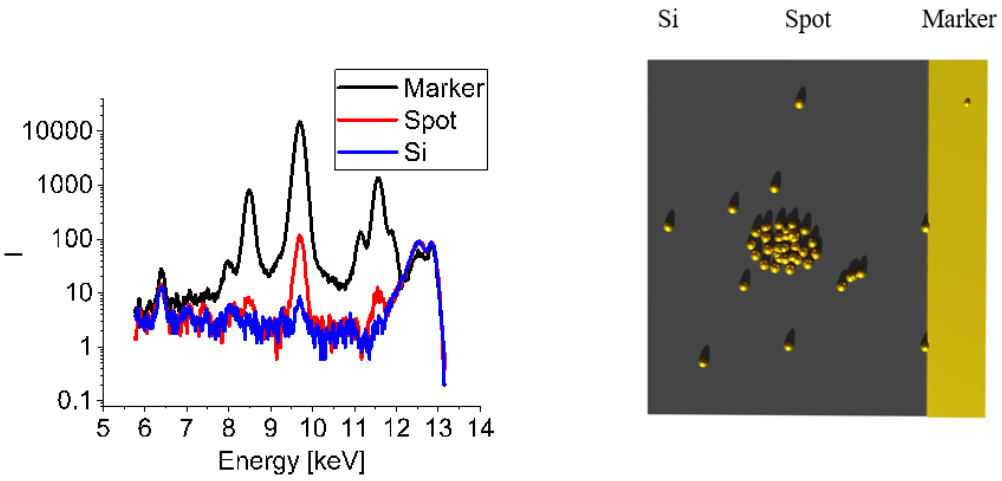

Figure 43: Example of the XRF yield depending on the photon energy for Si, Marker and spot with the drawing of the sample.

3) 2D contour plot along q_y at the critical angle of substrate (Si), which is used to make conclusions about the lateral distances of the object. See illustration in Figure 44.

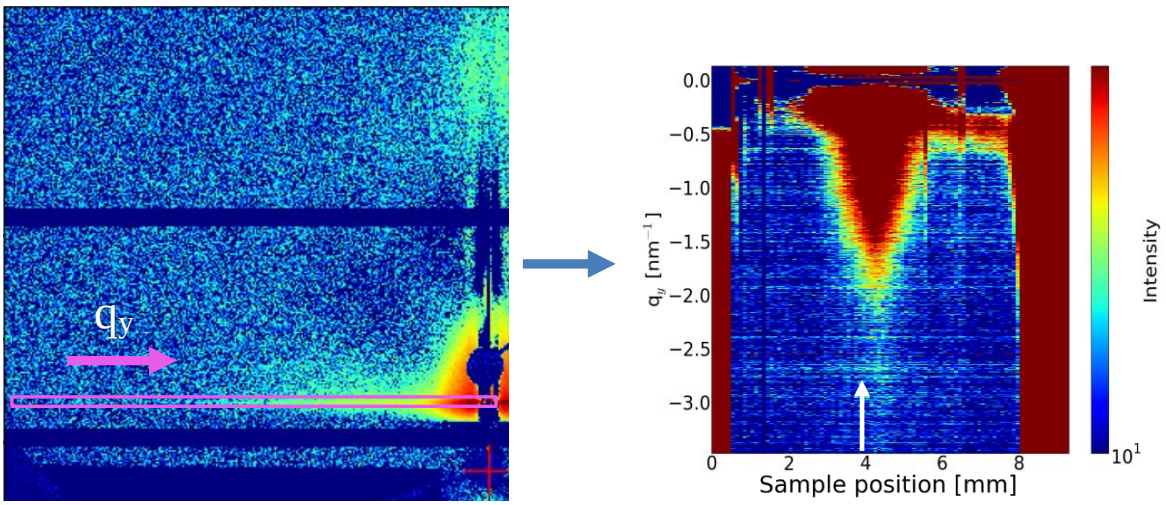

Figure 44: Example of the 2D plot along q_y. On the left is a single detector image, pink triangular shows the cut position at the critical angle of substrate. On the right is a full contour plot, consisting of several such cuts, arranged depending on the sample position. White arrow indicates the subtracted frame.

4) 2D contour plot along q_z covering the area where $q_{y,max}$ was found, which is used to estimate the signal corresponding to the height of the object (Figure 45).

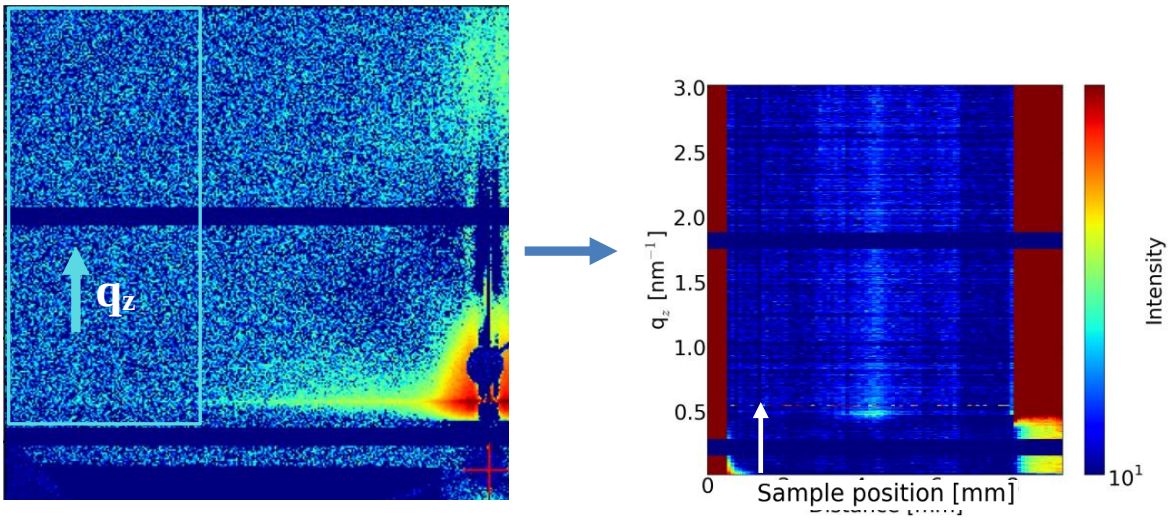

Figure 45: Example of the 2D plot along q_z. On the left is a single detector image, cyan rectangular area shows the cut position at the $q_{y,max}$. On the right is a full contour plot, consisting of several such cuts, arranged depending on the sample position. White arrow indicates the subtracted frame.

5) Horizontal line cut for the spot position showed in 2). Example provided in Figure 46.

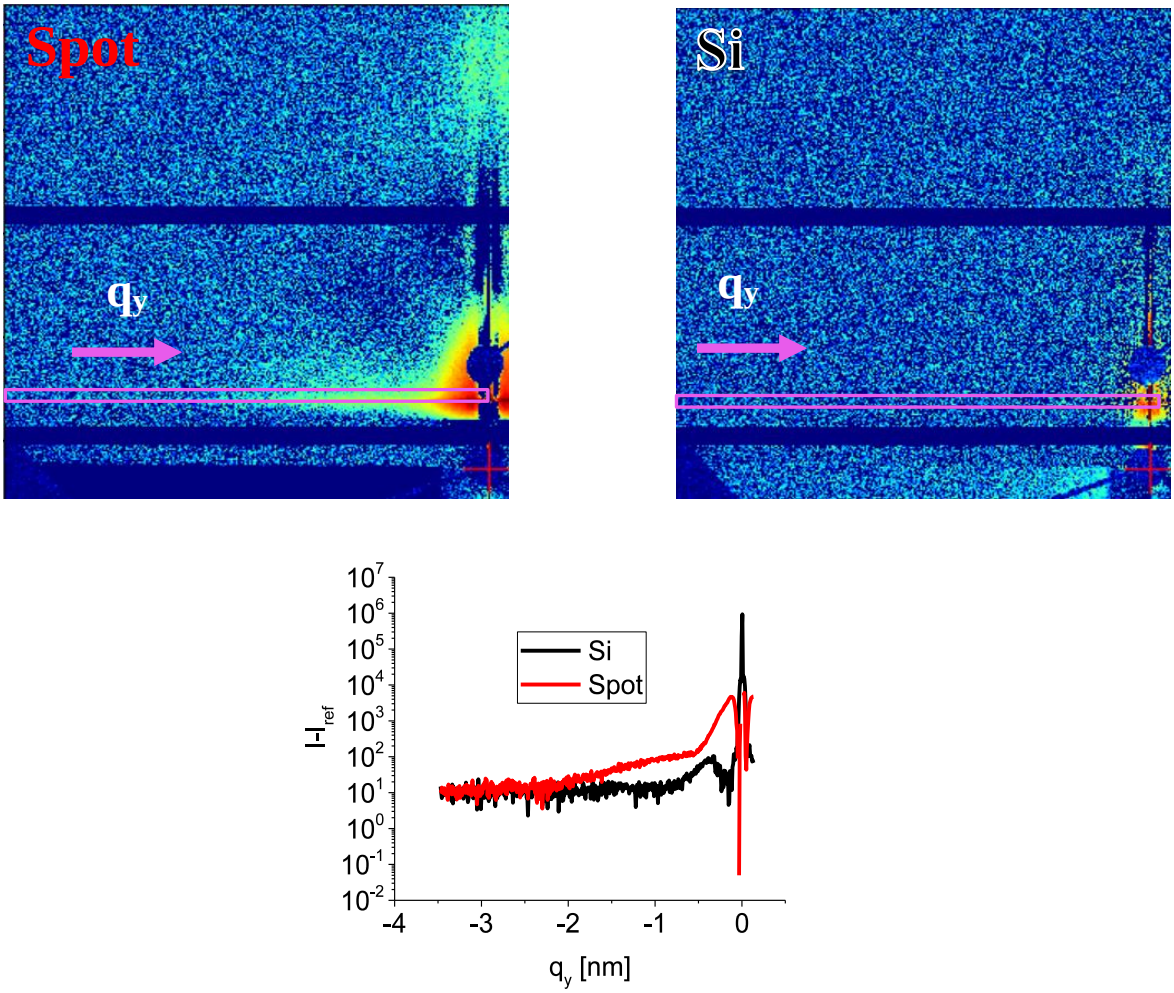

Figure 46: Example of the horizontal cut along q_y. On top two detector images on different sample positions are shown: Spot maximum and Si. Below are the horizontal cuts made at their positions.

6) Vertical cut at the q_y,max position shown together with the corresponding simulated data. This is provided for size-selected clusters only, not for adatoms (1AUSL1 and 1AUSL2 are adatoms in this text). See example in Figure 47.

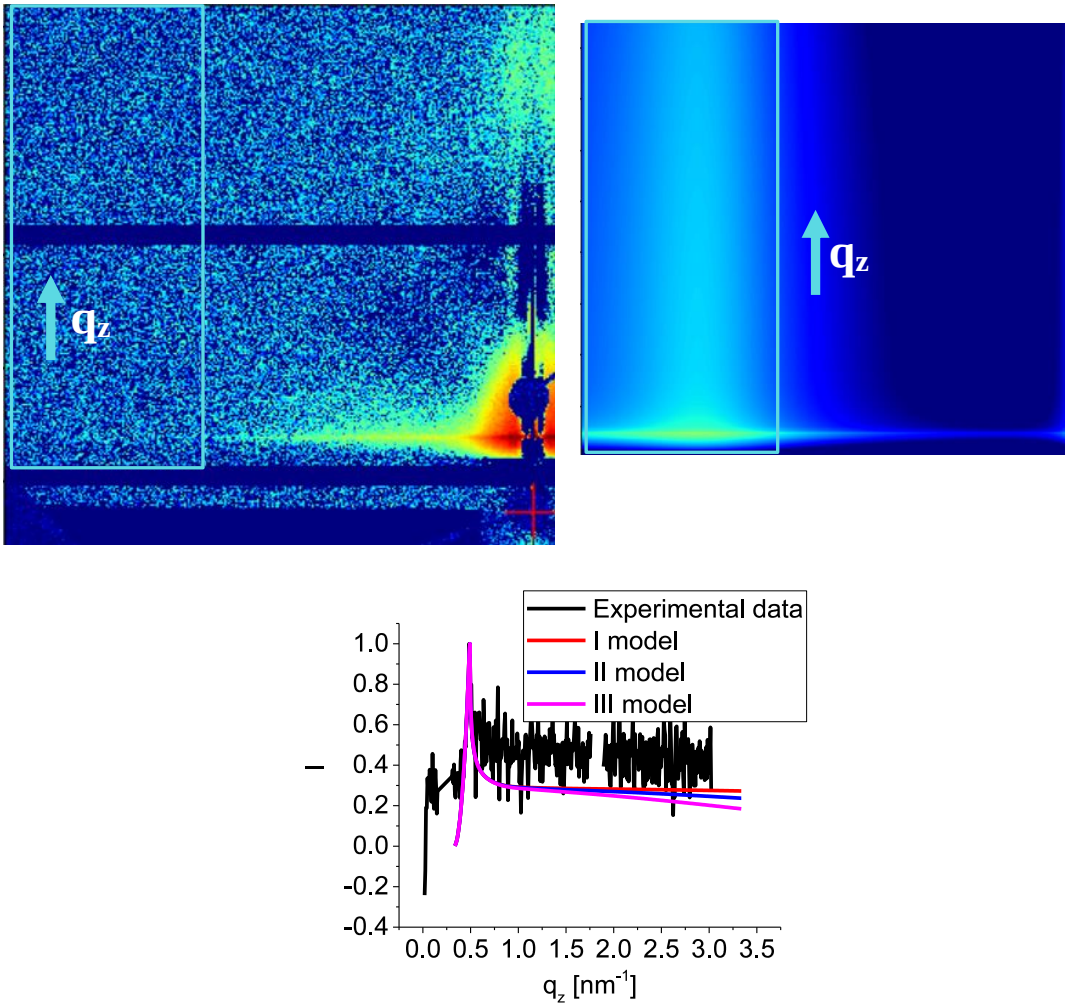

Figure 47: Example of the vertical cut on the spot position with the simulated data. On top left figure is the experiment and right one is one of the simulations. Below is the vertical cut for the experiment with cuts from 3 simulated models.

7) Vertical cut at the small q_y position along q_z, see Figure 48. It is called a 'detector cut' and gives information about the height of bigger structures. Sometimes it is located at q_y=0, but beamstops can disturb the signal, therefore in this case it is close to zero but outside of the beamstop position. Such a cut is provided for 1AUSL2, 5AUSL1, 7AUSL1, 9AUSL2, 11AUSL1 at q_y = -0.6 – -0.17 nm^{-1}. They all are discussed in Section 3.2.7.

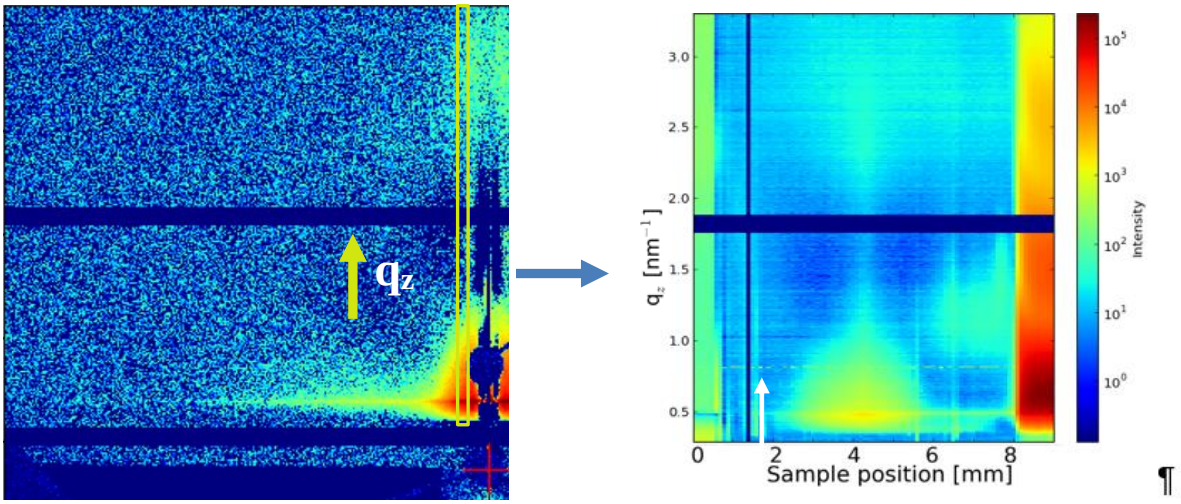

Figure 48: Illustration of the 2D plot along q_z. On the left is a single detector image, yellow triangular shows the cut position at the small q_y. On the right is a full contour plot, consisting of several such cuts, arranged depending on the sample position. White arrow indicates the subtracted frame.

Background subtraction and choice of the exposure.

For all samples 1) is used to make a choice of the sample position to be exploited in the structural analysis. Samples except for 1AU1 have undergone the background subtraction of the Si (the same as in 2)), since all of them have a capping layer of Al. XRR analysis of the capping layer on several samples was done (provided in the Appendix: Section 5.7) and showed thicknesses of 4.6–5.4 nm, this meant a slight variation of Al layer thickness on each of them. Therefore, it was important to choose as the background frame one which is on the corresponding sample. For the samples 1AUSL2, 9AUSL2, 5AUSL1, 7AUSL1, 11AUSL1 GISAXS data was summed up to be equal to 20s exposure (1s per position). This was chosen to exclude a possibility of the radiation induced changes on the ultrasmall clusters, to make an experiment more consistent but still remain sensitive. For the abovementioned samples radiation induced changes and the explanation about the optimal exposure time is provided in Section 3.2.8. For the samples 1AUSL1 and 9AUSL1 10 s and 800 s exposure, respectively, was used. This was done after the thorough analysis for the radiation induced damage (provided for the latter samples in the supplementary information of the published article[132]), since single atoms are much easier to be affected 1AUSL1 could resist less exposure.

Analysis routine for samples 1AUSL1, 1AU1 and 9AUSL1

9AUSL1 and 1AUSL1:

Data from 1) and 2) was used to detect the maximum of the spot. Then it was compared with the 3) and 4) to confirm existence of the signal on the corresponding sample positions. Three integrated curves in the middle (maximum of the spot) were summed up in order to improve the signal to noise ratio. Then, $q_{y,max}$ was found using Lorentzian fit in 5). Finally, knowing $q_{y,max}$ and effective thickness (note: in this model approach it is equal to coverage) both interclusteral distance D (Equation 17) and cluster radius

R (Equation 12) was calculated, see description of the approach in Sections 2.2.2 and 1.3.1.3. The number of atoms in a cluster was estimated for the 9AUSL1, using Equation 13.

1AU1:

Sample with the effective thickness of 50% ML had clusters deposited on the whole substrate surface. Using horizontal cut, as in 5), a Lorentzian fit was performed. The resulting $q_{y,max}$ was used to estimate D and R.

Analysis routine for samples 5AUSL1, 7AUSL1, 9AUSL2, 11AUSL1.

Higher intensity signals in **1** (points above) also revealed the position of gold on the surface of these samples. It had a clearly visible Lorentzian shape signal, which showed gold distribution over a limited space. The higher intensity indicated the middle of the gold spot. From the previous experiments done with ICARUS cluster source the expectation was that in the area of 2 mm^2 (size of a detection pin mounted) an evenly distributed 10% ML was deposited. To estimate real effective thickness of each point of the bell shaped curve, the area under the graph was calculated and then compared with the expected area. This provided an estimate of the thickness in the middle of a spot. An example is shown in Figure 49. This was not done for 1AUSL2 and the approach used for 1AUSL1 was applied.

Since it was expected that the higher the effective thickness is, the more aggregation occurred, one had to aim for the point on the surface with still significant signal but having not so much material deposited. This could also be influenced by the size of clusters, since the bigger the cluster the less it tend to aggregate. This meant that for 11AUSL1, the position where the effective thickness is 12% could be used, while for 9AUSL2 the best position was the one with 10–11% ML, while for 7AUSL1 and 5AUSL1 sample positions with 8–9% ML were taken. This approach allowed observation of the signal from ultrasmall clusters with minimal distortion due to the signal from aggregates. The next step was to estimate the $q_{y,max}$ signal and to fit it by Lorentzian or Gaussian function in 5). For 1AUSL2 fit was done on the maximum spot position. The data was noisy, so it was required to sum up frames from several repetitions. To maintain balance between getting better signal and excluding possible radiation effects, 20 frames were taken for all of the samples (as explained in Section 3.2.8). Interclusteral distances and radii were estimated as described in Equation 17 and Equation 12. All samples except for 1AUSL2 had the number of atoms in each cluster estimated, using Equation 13.

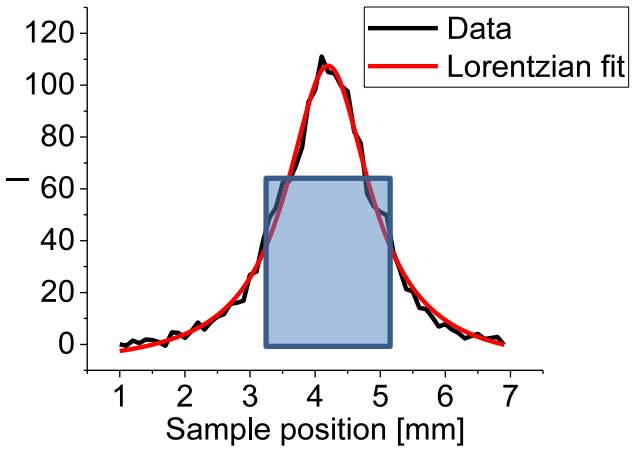

Figure 49: Part of the XRF profile curve from Figure 42 (black) and the fitted curve (red). The blue rectangle has the same area as the fitted curve.

The width of the spots of deposited ultrasmall clusters are listed Table 6. The FWHM increases with the clusters size, which can indicate that smaller clusters being lighter are landing on an area smaller than the size of the pin, while larger clusters are more widely distributed. This can also be a reason for the higher aggregation effect on 5AUSL1 and 7AUSL1.

PCA statistical analysis was done for several samples. The aim was to show that there is a signal in the expected area of bigger q_y even if the data is uncorrelated. The biggest variance revealed the spot signal on the corresponding sample positions.

Note: error for all values was calculated using Gaussian error propagation, using techniques outlined by Schwartzkopf[121].

Sample name	FWHM in XRF profile [mm]
5AUSL1	0.53±0.05
7AUSL1	1.16±0.02
9AUSL2	1.18±0.05
11AUSL1	1.57±0.04

Table 6: Values of spot FWHM obtained from fluorescence data.

3.2.2. Au_1

In this chapter three adatomic samples are discussed. They are two samples with 50% ML of gold material, the first of which was soft-landed and capped with Al (1AUSL1), the second deposited with RF magnetron (HASE[78]) (1AU1). The third sample (1AUSL2) is similar to 1AUSL1, but with a coverage of 10% ML. For all samples GISAXS data is shown, but XRF was used only for 1AUSL1 and 1AUSL2. The latter method is important for finding the exact position of gold and therefore it was not needed for 1AU1, which had gold evenly distributed throughout the sample.

This chapter is organised as follows: in the first subsection samples with 50% ML (0.144 nm) are compared; in the second - observed differences from the sample with 10% ML are discussed. The former (Investigation of 1AUSL1 and 1AU1) is the part of the published article "Towards the geometric structure of small supported Au_9 clusters on Si."[132].

Investigation of 1AUSL1 and 1AU1.

Figure 50 shows the XRF spectra for 1AUSL1. During the measurements, the sample was moved perpendicular to the incident beam with small steps of 0.1 mm covering a range of 7 mm in total. This allowed the detection of part of the two Au markers at the edges and the Al-covered spot with ultrasmall Au clusters, and thus it was possible to precisely locate the deposited clusters on the surface. Figure 50**a** gives the XRF yield at an energy of 9.6 keV (corresponding to the L_α – line of Au) as function of sample position. Given the scanning scheme and sample preparation, the left and the right peak correspond to the markers. The peak at position 4.5 mm (indicated with the red arrow) therefore arises from the adatomic spot, and this is also supported due to its width of about 1 mm (FWHM). Note that only part of the marker signals is seen and blue lines show the expected marker shape. It is important to resolve the centre position, which has the low fluorescence signal coming from the spot, considering that at the marker position the XRF detector shows saturation. Figure 50**b** shows the XRF yield measured at three selected positions on the adatomic sample, namely Au markers, substrate (Si) and spot (schematically presented in Figure 17). The emission lines of Au L_α and L_β are located at 9.6 keV and 11.4 keV[155], respectively, and are clearly visible in two of the spectra shown. Along with Figure 50**a**, the spectra could be associated to the Au marker (red line), adatomic spot (black line) and the Al-capped Si substrate (blue line).

The GISAXS contour plots shown in Figure 51 demonstrate how line cuts along q_y and q_z accordingly repeat the shape of the markers and the spot from Figure 50**a**. Markers of Au, which show high signal intensity on the left and the right of the sample, are also recognizable. For all of the GISAXS plots, the Si and Al background was subtracted to enhance the Au signal. The black lines at position 2.5 mm is from the subtraction of the Si background from the whole set of data.

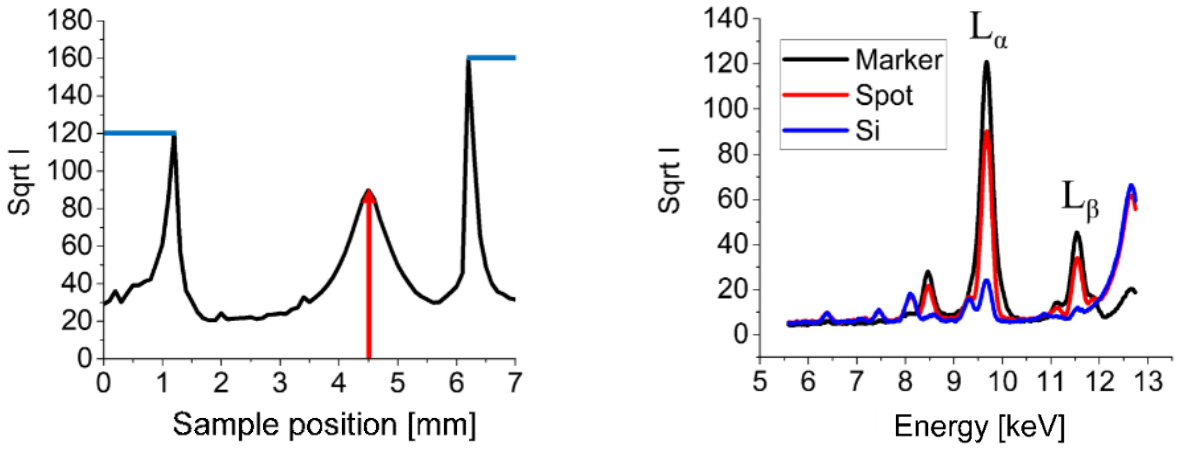

Figure 50: Sample 1AUSL1 (a) XRF spectra of the sample at the L_α Au line as function of lateral distance on the Si surface. At a distance of 4.5 mm on x-axis is the maximum of XRF signal stemming of the adatomic spot, on the left and right from it are Au markers. Blue lines show the expected shape of the markers, because the sharp shape of them caused by detector saturation. (b) XRF spectra of the sample for adatomic spot (red), Au markers (black) and Si (blue). [132]

The Si and Al backgrounds were also subtracted from Figure 51**a** to obtain a more prominent signal. Figure 51**b** depicts a horizontal cut from the location of the spot on the sample, whose position has been selected from the XRF signal. This graph provides information on the average lateral correlation distances of the objects. The peak position of the spot $q_{y,max}$ was used to estimate cluster correlation distances using $D = {2\pi}/{q_{y,max}}$ (Equation 17)[35] .

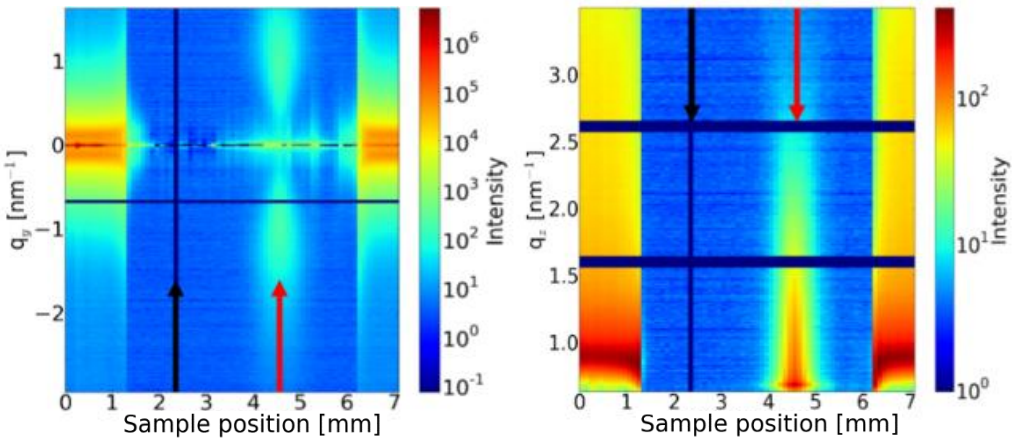

Figure 51: (a) Contour plot of the out-of-plane cuts (along q_y) derived at the Si Yoneda peak (q_z=0.7 nm^{-1}) for different positions on the substrate. The black arrow indicates the subtracted data frame, the red one- the maximum of the adatomic spot. (b) GISAXS off-detector (along q_z) line cuts at q_y from -1.9 to -0.7 versus the position on the substrate. The black arrow indicates the subtracted data frame, the red one indicates the maximum of the adatomic spot. [132]

Given the position of the out-of-plane maximum at $q_{y,max}$ = 0.91 nm^{-1} obtained by a Lorentzian fit of the intensity distribution in Figure 52**a**, the average interparticle distance is about D = 6.9 nm. Further analysis was performed using the established hemispherical model for Au cluster growth on silicon substrates by Schwartzkopf *et al.*[31]. In the present work the cluster radius has been calculated. According to this model assumption, the average radius of the supported clusters can be calculated by $R=\sqrt[3]{(\sqrt{3})^3 \delta D^2/4\pi}$ (Equation 12), where R is the radius of the cluster, δ is an effective thickness of a homogenous layer and D is the cluster correlation distance. The results obtained are shown in Table 7.

Figure 52**b** depicts a typical out-of-plane cut from sample 1AU1. Positions of the side maxima are located at smaller q_y (0.29 ± 0.01 nm^{-1}) than for the adatomic 1AUSL1 sample (0.96 ± 0.01 nm^{-1}) with equivalent coverage. This shows the existence of twice as large geometrical structures as for the sputtered sample. Since in the sputtered 1AU1 case small cluster sizes are expected[31], this can indicate

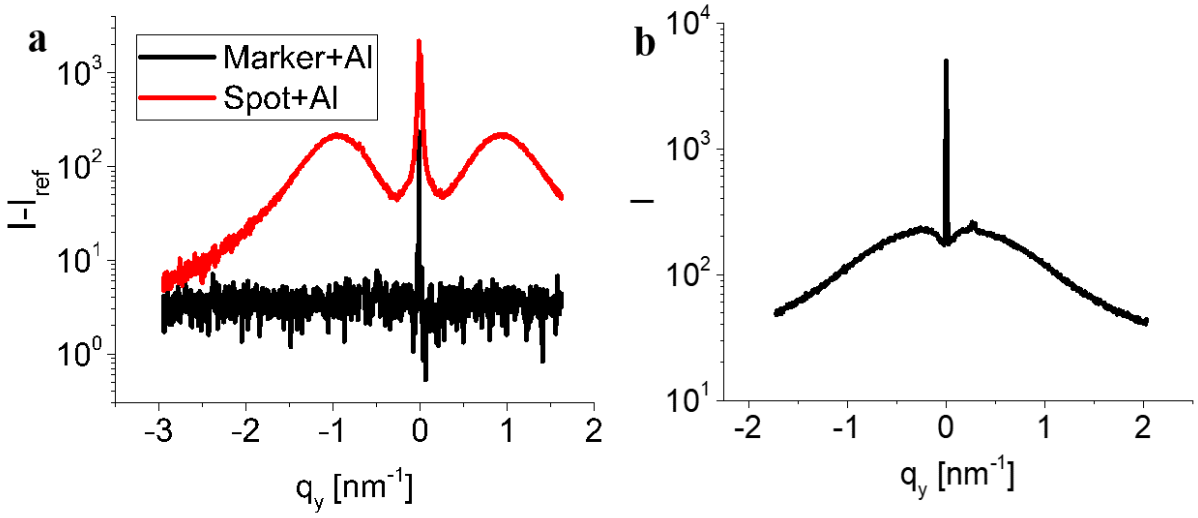

Figure 52: (a) GISAXS out-of-plane (along q_y) line cuts at the position with the maximum amount of material obtained from the XRF data. Red curve- adatomic spot, black curve- markers. Sample 1AUSL1. (b) GISAXS out-of-plane (along q_y) line cuts for 1AU1 sample.[132]

Name	1AUSL1	1AU1
Effective thickness δ[nm]	0.14 ± 0.01	0.14 ± 0.01
$q_{y,\,max}$[nm^{-1}]	0.96 ± 0.01	0.29 ± 0.01
Cluster correlation distance D [nm]	6.54 ± 0.06	22.08 ± 0.59
Cluster radius R[nm]	1.37 ± 0.05	3.07 ± 0.02

Table 7: Calculated structural values for soft-landed adatomic and sputtered sample

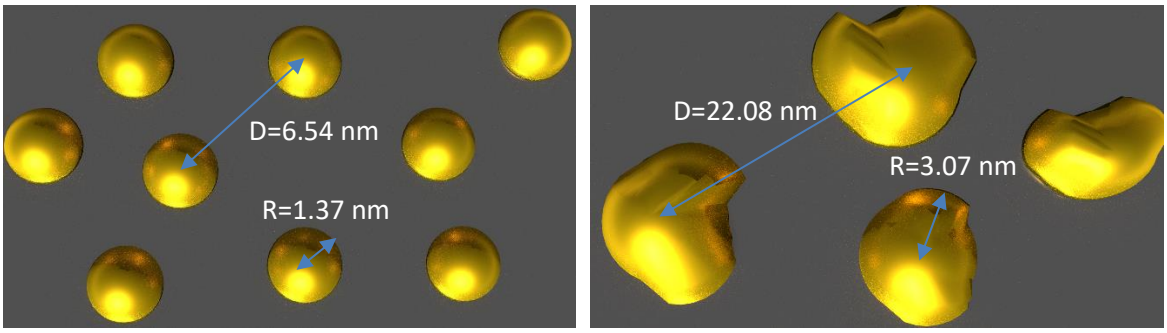

Figure 53: Schematic illustration of supported clusters on the surface of Si, coverage of 50% ML. (left) 1AUSL1 after soft-landing of atoms and (right) 1AU1 after deposition in RF-magnetron.

that the lack of a capping layer led to agglomeration. In the work of Levine *et al.*, a cluster mobility for small Au amounts was detected[156] which can also occur for the adatomic 1AUSL1 sample. However the preparation method used here, using soft-landing of ions and a capping layer, helps to reduce the agglomeration and cluster mobility effects. Therefore, not only the soft-landing scheme but a capping layer is mandatory in case of *ex situ* investigations of ultrasmall clusters.

Using the estimated values of radii and interclusteral distances, the appearance of how the clusters on the surface might look are illustrated schematically in Figure 53.

Investigation of 1AUSL2.

The same approach as for 1AUSL1 was used to analyse the sample 1AUSL2. The XRF plots for this 10% ML adatomic sample are shown in Figure 54. In this measurement, the range of 7.8 mm was covered, with of 0.1 mm. By this method a large part of the sample was examined, including the marker which in this case was only on one side of the sample. The profile of the sample expressed by the XRF yield depending on the sample position is shown in Figure 54**a**. It can be seen that a low, but still visible signal is on the position 3–5 mm, which is expected to be originated by the adatomic spot. At the positions 7.3–7.8 mm is the signal from the deposited marker. In Figure 54**b** the fluorescent yield for three position on the sample (Marker, Spot and Si) is shown. Emissions lines of Au L_α (9.6 keV) and L_β (11.4 keV) has been clearly visible similar to 1AUS11. The XRF detector alignment aiming to be extremely sensitive to locate small amount of gold throughout the whole sample. It is the indication that during the deposition atoms were deposited not only in the selected area, but some were scattered on the whole surface. It is possible that the similar situation can exist for all prepared sample, but not detectable. Due to the thickness of 5 nm, it is optically visible which is demonstrated with the photograph of the sample in Figure 54**c**.

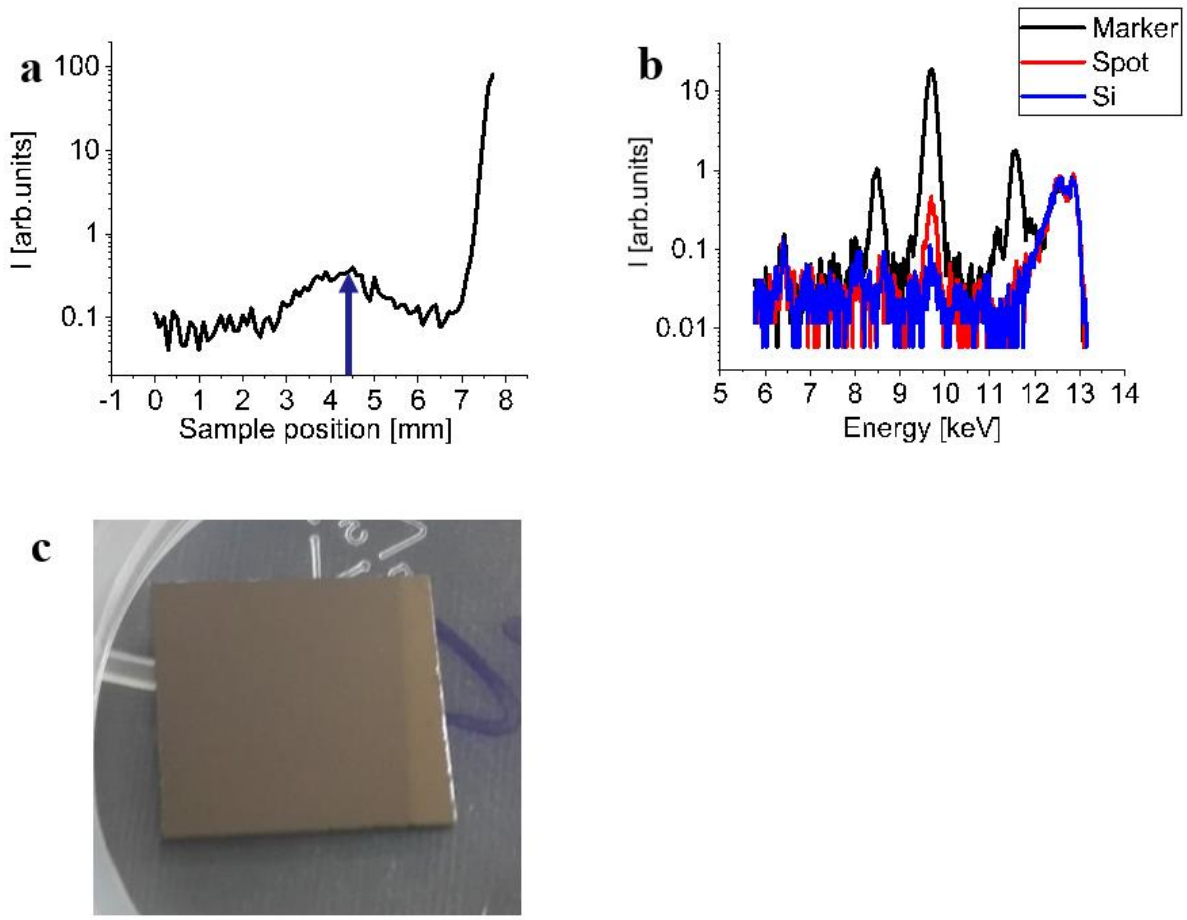

Figure 54: (a) XRF spectra of the sample at the L_α Au line as function of lateral distance on the Si surface. At a distance of 4.5 mm on x-axis is the maximum of XRF signal stemming of the adatomic spot, on the right from it is the Au marker. (b) XRF spectra of the sample for adatomic spot (red), Au marker (black) and Si (blue). (c) Photograph of the sample 1AUSL2. The yellow line on the right is the Au marker.

The XRF data in Figure 54**a** can be compared with the GISAXS data in Figure 55**a,b.** In Figure 55 contour plots of line cuts along q_y and q_z are provided, where the high intensity signal position is on the same place was found at (3.5–5.5 mm) as in the XRF plot. It also applies to the signal from the marker which is on the left. Interestingly, the spot signal in this data is only visible in the small q-range, which indicates that such structures have big radius in real space. This result suggests that this signal is from aggregates, formed from adatoms. Contour plot along q_z indicates that this structure has a large height too, since the distance between the signal maxima is rather small in reciprocal space.

In Figure 56 single line cuts along q_y and q_z from the maximum of the spot are shown. As above cluster radius was estimated, using Equation 12 with the value of 2.4 nm, as shown in Table 8. In addition to the lateral distance, estimation in Figure 56**a**, it is also possible to estimate the height of the cluster. Since several maxima in the q_z direction are visible, the height of the cluster has been calculated [31] using Equation 18: $H = 2\pi/\Delta q_z$. There Δq_z is a distance between two maxima or minima in the vertical direction. The resulting height is around 6.5–6.6 nm, which indicates a three dimensional structure. This aggregate most likely has larger height than its diameter.

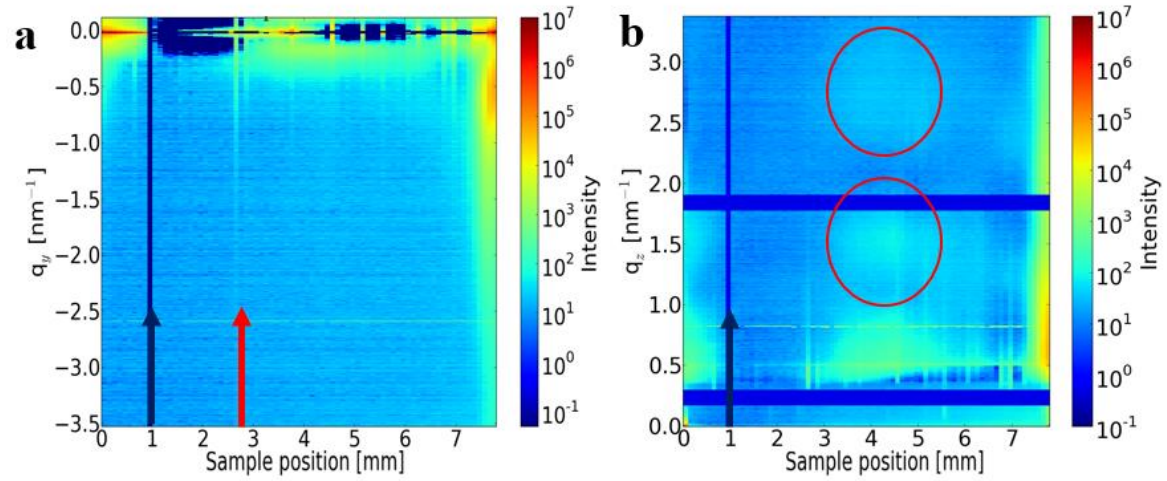

Figure 55: (a) Contour plot of the out-of-plane cuts (along q_y) derived at the Si Yoneda peak (q_z=0.54 nm^{-1}) for different positions on the substrate. The black arrow indicates the subtracted data frame, the red one- the maximum of the adatomic spot. (b) GISAXS off-detector (along q_z) line cuts at q_y from -0.3 to -0.08 versus the position on the substrate. The black arrow indicates the subtracted data frame, red circles the maxima of the adatomic spot.

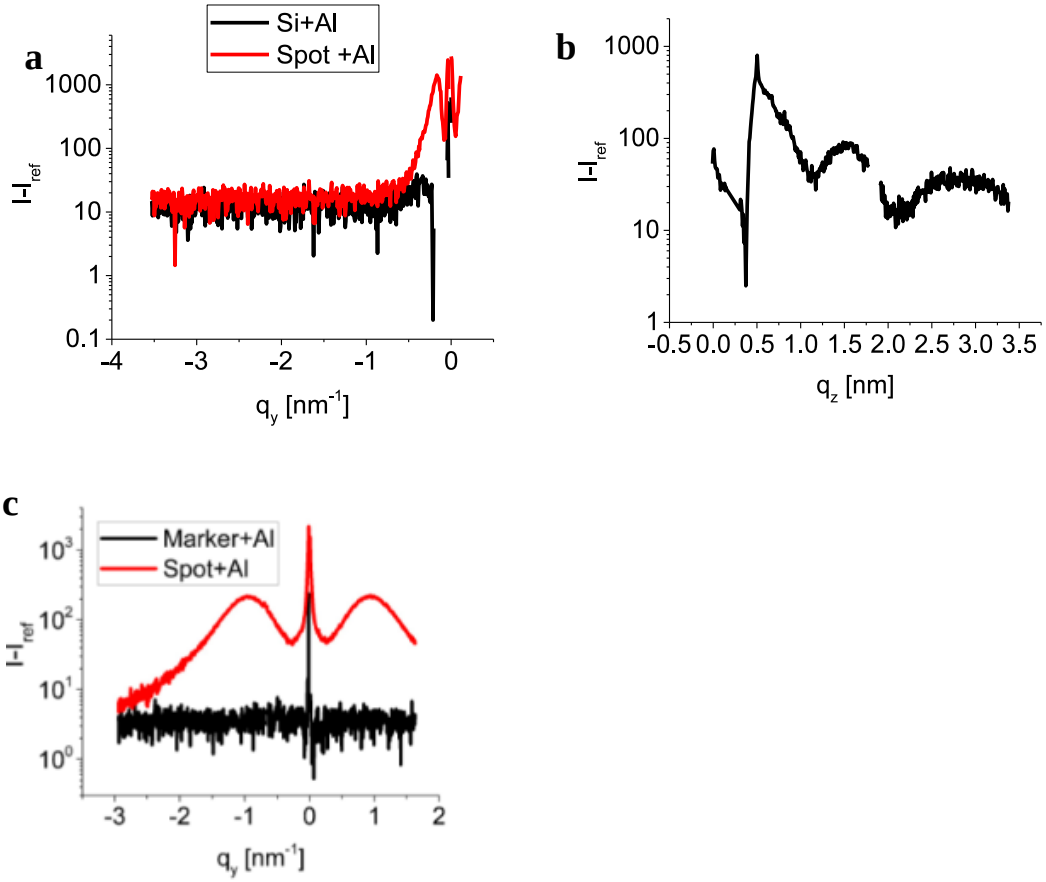

Figure 56: (a) GISAXS out-of-plane (along q_y) line cuts at the position with the maximum amount of material obtained from the XRF data. Red curve- adatomic spot, black curve- markers. (b) GISAXS off-detector (along q_z) line cut for the experimental data at the position with the maximum amount of material obtained from the XRF data. (c) GISAXS out-of-plane (along q_y) line cuts at the position with the maximum amount of material obtained from the XRF data. Red curve- adatomic spot, black curve- markers. Sample 1AUSL1.

Name	Adatomic 10% ML
Effective thickness δ[nm]	0.0288± 0.003
$q_{y,\,max}$[nm^{-1}]	0.18 ± 0.003
Cluster correlation distance D [nm]	34.9± 0.06
Cluster radius R[nm]	2.42 ± 0.08
Cluster height H [nm]	6.5 ± 0.21

Table 8: Calculated structural values for 1AUSL2.

Table 9 compares the measured radii of all three samples: 1AUSL1 (50%ML), 1AU1 (50%ML), 1AUSL2 (10%ML). As expected, the sample 1AU1 (being prepared without soft-landing scheme and also higher velocity (higher energy) than other samples) formed the largest clusters of 3.07 ± 0.02 nm radius. Interestingly, 1AUSL1 had the smallest radius of 1.37 ± 0.05 nm. These results suggest that the structure with sizes of about 1.4 nm did not form when the soft-landed sample had 10% ML (1AUSL2) effective thickness. Although this does not seem consistent, there are two possible explanations for this result. The first is that adatomic deposition samples are not as reproducible as for the big clusters. The second is that as the amount of material deposited has a much lower signal, soft-landing matrix was more sufficient than for the long deposition of 1AUSL1. In case dimers or trimers formed during this deposition, not only their scattering volume was too low to be detected but in such experimental conditions q_y range was not sufficient.

The resulted cluster arrangement is presented in Figure 57 for each of the three samples discussed. 1AUSL2 had the biggest interclusteral distance, while the sputtered 1AU1 sample had the largest radius. According to the analysis, the height of 1AUSL2 is slightly bigger than the radius, which indicates an elongated shape, possibly as the result of the soft-landing deposition.

Name	1AUSL1 (50%ML)	1AU1 (50%ML)	1AUSL2 (10%ML)
q_y [nm^{-1}]	0.96± 0.01	0.29 ± 0.01	0.18± 0.003
R [nm]	1.366± 0.05	3.07 ± 0.02	2.42± 0.08

Table 9: Comparison table for adatomic and sputtered samples.

This result has shown that in the case of monoatomic deposition, even when the soft-landing scheme applied, resulted structures do not seem to be easily reproduced. The reason for the different size structure of 1AUSL2 than 1AUSL1 could be due to a difference in temperature during preparation. Small Au clusters have been found to exhibit diverse properties at different temperatures Jia *et al.* showed a strong temperature dependence of the catalytic activity of Au clusters of size below 1 nm in the range of -90 – -70 °C[157]. It can be extrapolated from the work of Castro et al.[49] that the melting temperature of Au could be lower than 0 °C for clusters smaller than 1 nm, and that the melting temperature itself is strongly influenced by the cluster size[46]. Therefore in systems with a single atom as the initial unit, small differences of temperature may strongly affect the properties of the final system. It can be the subject of further work to investigate the dependence of ultrasmall Au cluster formation on preparation temperatures in the range -200 – 0 °C.

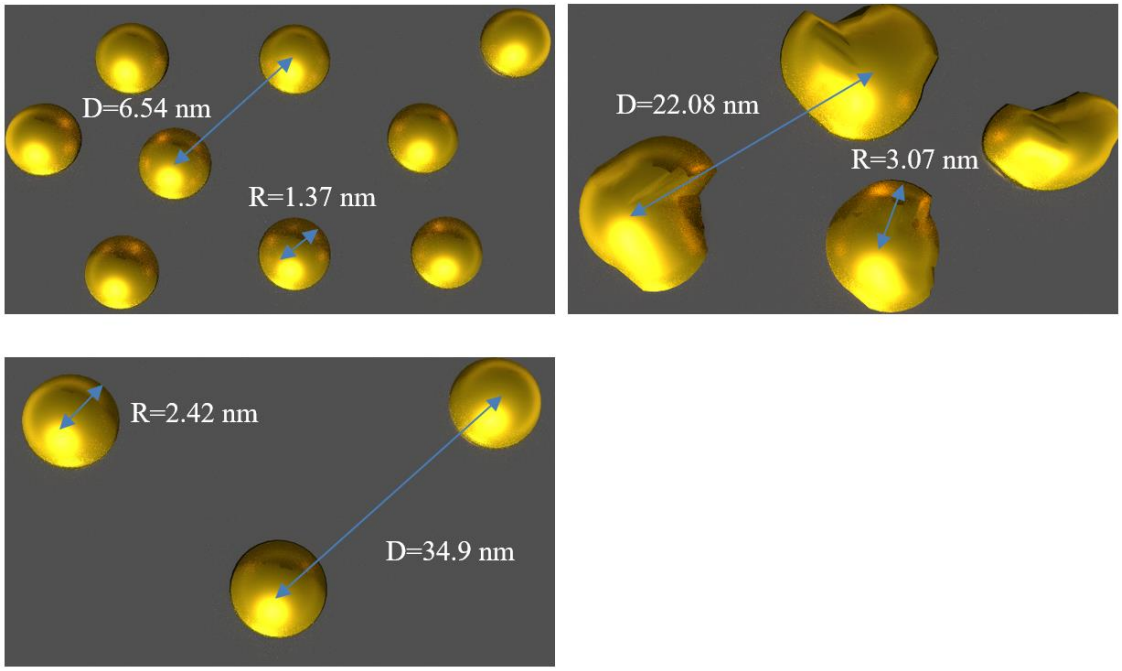

Figure 57: Scheme of cluster arrangement for 1AUSL1, 1AU1 and 1AUSl2.

3.2.3. Au_9

In this section, two samples of Au_9 are discussed, which were prepared and measured separately. The sample 9AUSL1 was the first deposited size-selected cluster successfully investigated with both XRF and GISAXS methods. In addition to these, XPS data for 9AUSL1 is shown to demonstrate the stability of the capping layer. The sample 9AUSL2 was measured with optimised experimental conditions and was important for confirmation of the sample reproducibility.

The subsection about 9AUSL1 is the part of the published article "Towards the geometric structure of small supported Au_9 clusters on Si."[132]. In the next section, the sample 9AUSL2 has been discussed and compared with 9AUSL1. Part of the conclusions in the part Height analysis, concerning 9AUSL1 includes a small part from the article mentioned above.

Investigation of 9AUSL1

Figure 58 shows the corresponding set of plots for the Au_9 soft-landing deposition. In this case the same strategy is used, but for a much more complicated system with a five times lower deposited amount of Au, i.e. having a 10% ML coverage (choice of the coverage discussed in Section 3.2.7). This small amount of material is needed to reduce the probability of aggregation, thus allowing the determination of the shape of the individual clusters. Figure 58**a** gives the fluorescent signal at E= 9.6 keV (L_α Au line) of the sample while scanning through it over a distance of 4 mm. Figure 58**b** shows the XRF yield collected on the Au_9 sample.

Figure 59 presents contour plots obtained from corresponding GISAXS data. Both of these 2D GISAXS plots had the Al and Si backgrounds subtracted. To enable the observation of even a very weak signal from the size-selected cluster spot, an adaption was made (colour scheme was adapted). In Figure 59**a** and Figure 59**b**, a strong peak exists at distance of 3.2 mm from the start of the scan, which arises from the marker.

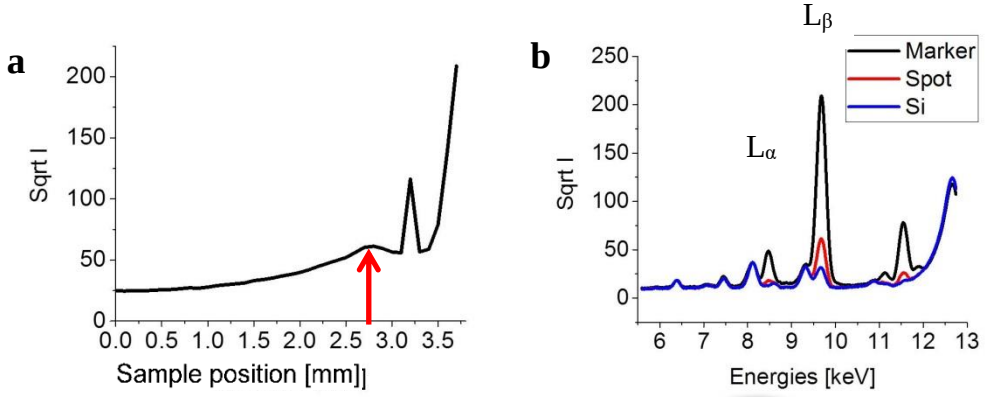

Figure 58: (a) XRF spectra of the sample at the L_α Au line as function of lateral distance on the Si surface. At a distance of 2.8 mm on x-axis is the maximum of XRF signal stemming of the adatomic spot, on the right from it the sharp peak is an artefact and at 3.5 mm is an Au marker. (b) XRF spectra of the sample from energies for Au_9 spot (red), Au marker (black) and Si (blue). [132]

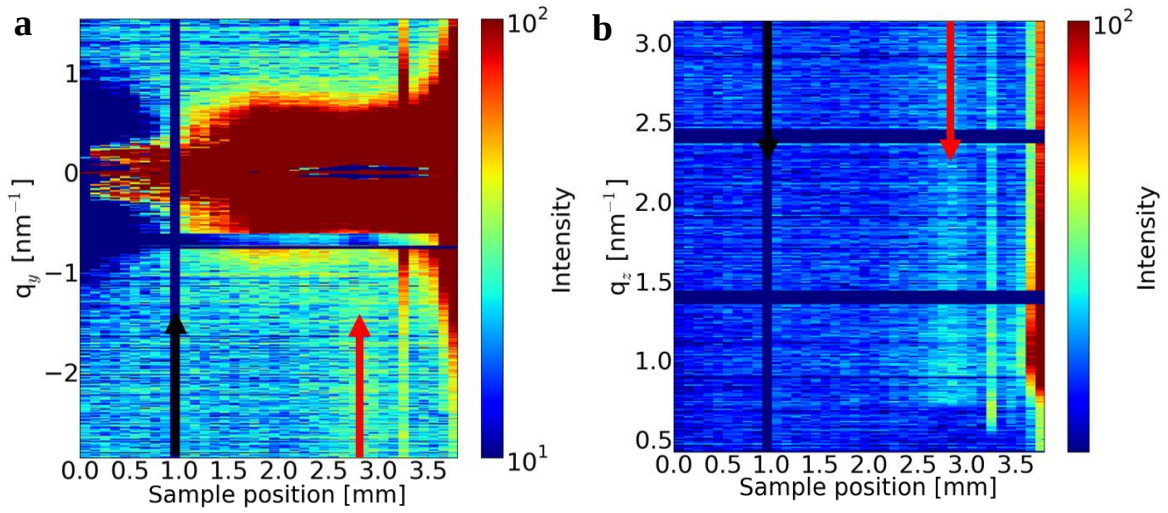

Figure 59: (a) Contour plot of the out-of-plane cuts (along q_y) derived at the Si Yoneda peak (q_z=0.7 nm^{-1}) for different positions on the substrate. The black arrow indicates the subtracted data frame, the red one- the maximum of the Au_9 spot. (b) Contour plot of off-detector (along q_z) line cuts at q_y from -2.1 to -1.4 versus the position on the substrate. The black arrow indicates the subtracted data frame, the red one the maximum of the Au_9 spot. [132]

In Figure 60 out-of-plane cuts are shown for the cluster spot and for Si. The inset shows a selected region ranging from -1 nm^{-1} to -3 nm^{-1} and suggests that a slight difference exists between the signals due to a peak occurrence in the spot signal at $q_{y,max}$=(2.4 ± 0.51) nm^{-1}. However, the peak is very weak and may be assigned to a very small amount of the material on the surface, being consistent with the 10% ML coverage. For this sample the same hemispherical model[31] as above was applied. The derived values for the cluster radii and correlation distances are shown in Table 10. The radius for Au_9 cluster results to 0.43 ± 0.06 nm, which is close to the value expected for a 3D cluster where the base consists of five atoms, three on the second level and one on the third. This type of cluster shape is one of those predicted by DFT calculations[28,6]. In view of possible damage induced by radiation, the measurements were repeated with shorter exposure and did not show discrepancies with the existing data.

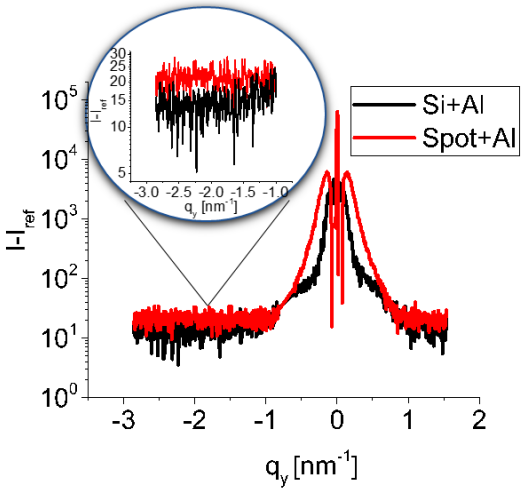

Figure 60: GISAXS out-of-plane (along qy) line cuts at the position with the maximum amount of material obtained from the XRF data and the Si position. Red curve - Au_9 spot, black curve - Si. The inset shows the difference between the Si and Au signal.[132]

Investigation of 9AUSL2.

Sample 9AUSl2 was scanned over a distance of 9.7 mm with a step size of 0.1 mm. This sample did not have predeposited marker layer of Au, and the scanned area of the substrate is in the range of 0.3–9.1. Outside of this area the sample was exposed to the X-ray beam, so meaningful information was not expected in this area due to the influence of X-ray beam. In Figure 61**a** the fluorescent yield from the surface of the sample at the energy 9.6 keV is shown. The main spot position is from 5 to 7 mm, but a small amount of gold around the spot area can be observed. The estimated FWHM was 1.18±0.05 mm. The pot maximum is marked with the red arrow. In Figure 61**b** is the XRF yield at the positions of one point of the spot and on the silicon surface.

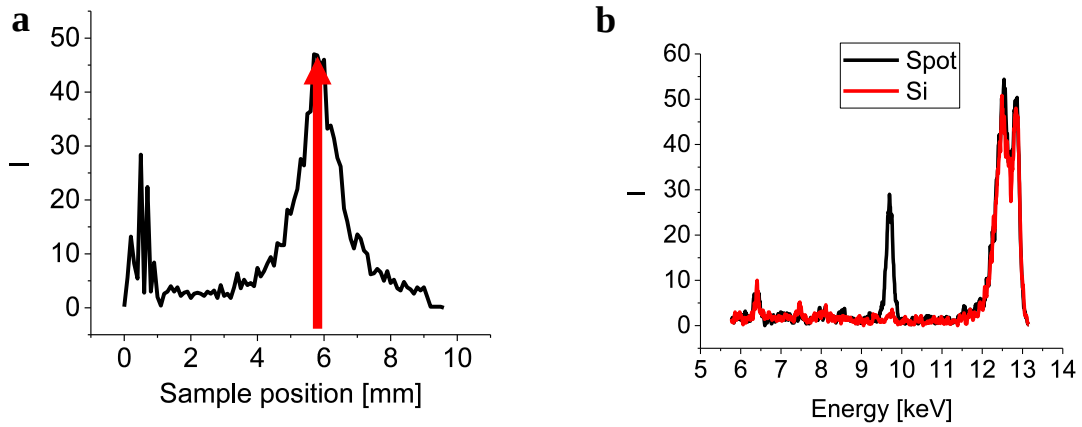

Figure 61: (a) XRF spectra of the sample at the L_α Au line as function of lateral distance on the Si surface. At a distance of 5.9 mm on x-axis is the maximum of XRF signal stemming of the adatomic spot, no markers were deposited. (b) XRF spectra of the sample for the spot (black), Si (blue) and the specimen had no markers.

Figure 62 shows contour plots of line cuts along q_y and q_z respectively. Both of them have the same area subtraction to enhance the signal from the size-selected clusters s. The subtracted frame is marked with the black arrow in both 2D plots. Both of them are in concordance with the XRF profile. It can be seen that the GISAXS signal intensity in larger q_y-ranges is not strong. This is caused by several reasons: 1) at larger q, the signal is weaker, 2) size-selected clusters consisting of nine atoms do not have a large scattering volume, 3) any signal from aggregates, being very intensive, influences the plot.

In Figure 63**a** the line cut on the position 6.4 mm is presented where the estimated effective thickness is around 10% ML in comparison with Si lateral position (7.8 mm). A line cut in the larger q-range is shown in Figure 63**b** to demonstrate the difference.

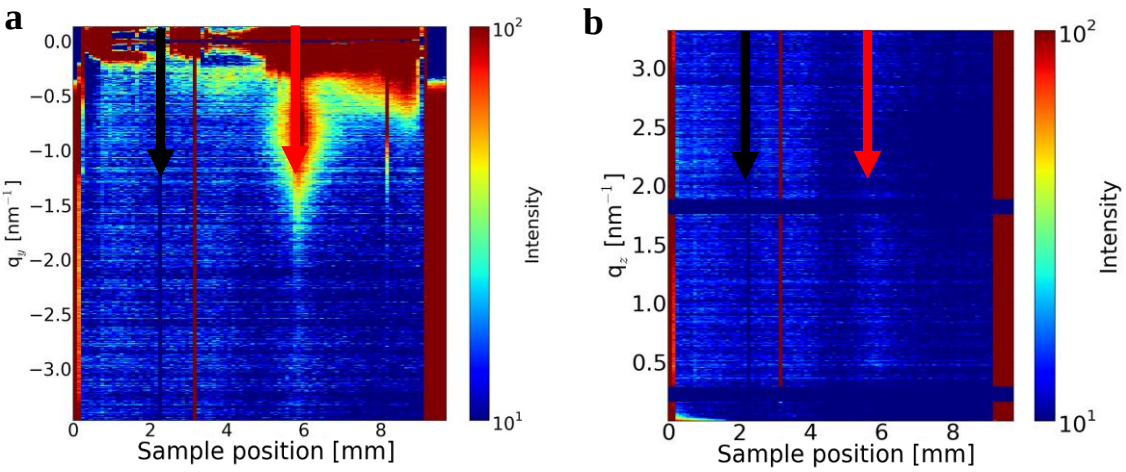

Figure 62: (a) Contour plot of the out-of-plane cuts (along q_y) derived at the Si Yoneda peak (q_z=0.54 nm^{-1}) for different positions on the substrate. The black arrow indicates the subtracted data frame, the red arrow indicates the maximum of the Au_9 spot. (b) Contour plot of off-detector (along q_z) line cuts at q_y from -3.5 to -1.5 versus the position on the substrate. The black arrow indicates the subtracted data frame, the red one the maximum of the Au_9 spot.

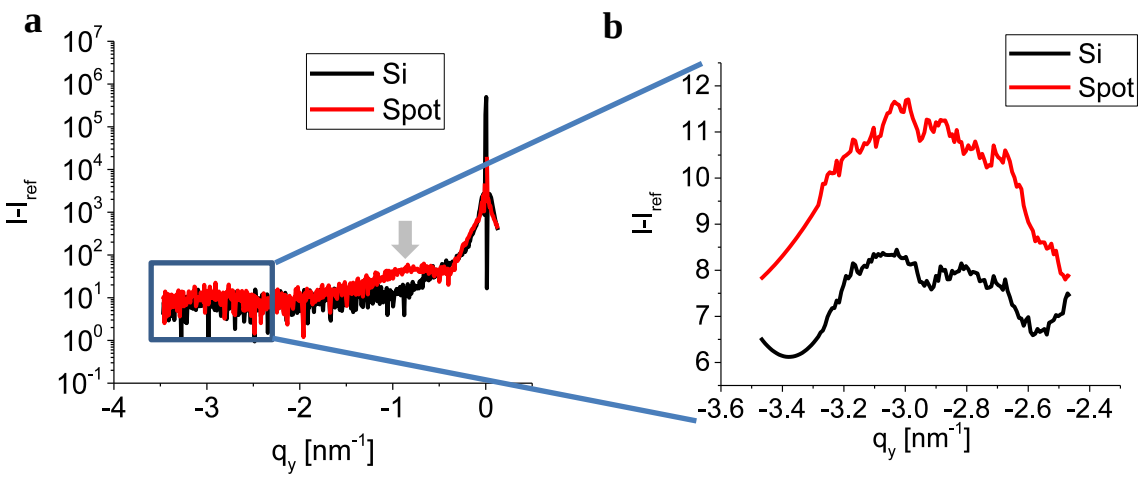

Figure 63: Sample 9AUSL2. (a) GISAXS out-of-plane (along q_y) line cuts at the position where the maximum counts of the material obtained from the XRF signal on the Si position. The red curve is showing - Au_9 spot and black curve is showing- Si. The feature indicated with an arrow at q_y=-1 nm^{-1} is caused by aggregates (see Section 3.2.7) (b) GISAXS out-of-plane cut in q_y range of -3.5 to -2.5 nm^{-1} , which helps to illustrate the difference in the bigger q-range between the spot (red) and Si (black).

For both 9AUSL1 and 9AUSL2, the radii and number of atoms in a cluster were estimated, using Equation 12 and Equation 13. Results are shown in Table 10 below.

Sample Name	9AUSL1	9AUSL2
q_y [nm^{-1}]	2.4±0.51	3.18 ±0.11
R [nm]	0.43± 0.06	0.38 ±0.02
N [atoms/cluster]	13.7±6.85	9.2±3.11

Table 10: Calculated structural values of 9AUSL1 and 9AUSL2.

Height analysis of 9AUSL1 and 9AUSL2.

Although the size of the radius and the number of atoms in a cluster are important, an estimate for the height can also help to understand the most probable shape. A number of models were created for simulations, using IsGISAXS[140]. In these simulations, radii and interclusteral distances, obtained from the experimental data were used. In addition, the differences in the experimental conditions were accounted for. Since this program only works with simple shapes, an anisotropic hemisphere was selected as a rather flexible form-factor. This allowed variation of the height without affecting the radius.

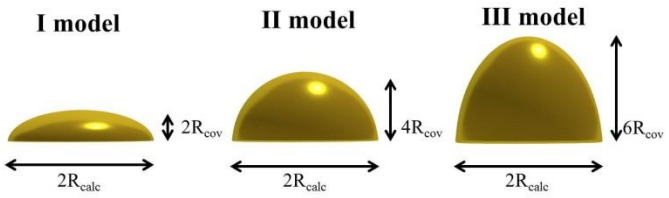

Figure 64: Sketch of the hemispheroidal models as used in the IsGISAXS simulations. R_{cov} = covalent radius of Au. R_{calc} is the calculated radius for Au_9 clusters.[132]

Figure 64 illustrates the shapes that were used for simulations in IsGISAXS[140]. The output of this program is a GISAXS detector image. A hemispheroidal shape for the clusters was chosen since one can change the height without interruption of the radius, and this was closer to the initial expectation. As can be seen in the picture above the I model is - hemispheroids with the height of 1 Au atom, II model is hemispheroids with the height of 2 Au atoms and III model assumption is hemispheroids with the height of 3 Au atoms. In these model simulations: radius was kept constant and equal to the calculated value from experimental data using Equation 12; height cannot be smaller than the size of the Au atom; the size of the detector, wavelength and the sample to the detector distance is the same as in the experiment; the substrate is Si and the scattering material is gold.

The obtained off-detector line cuts from the simulated scattering patterns are compared with experimental data for both samples in Figure 65**a,b**. These cuts contain information about the height of the object in the system. A linear fitting for these curve was performed over the area from 1 nm^{-1} to 2.5 nm^{-1} to compare the slope between the simulations and the experiment data, because this provides information about the height of the Au_9 cluster. The values obtained are presented in Table 11. It can be seen that the values of slopes in similar models are different, which is caused by the fact that in these two experiments conditions were different. The reason for this was that 9AUSL1 was the first successfully measured sample, while for 9AUSL2 experimental conditions were optimised considering all the previously collected knowledge about this system. However, the resulting structures have similar (within the error bar) q_y value, radius and estimated number of atoms (see Table 10). Furthermore, the second experiment was performed more precisely. The sample to the detector distance was kept as small as possible, the considering minimum length of the flight tube. The position of the XRF detector was precisely aligned using high precision motors, which increased the sensitivity and also decreased the dead time during measurements. Most importantly a smaller exposure time was used (1 s instead of the previous 10 s), which guaranteed no radiation induced changes (discussed in Section 3.2.8). In case of 9AUSL1, very small radiation induced changes could take place, but due to the longer exposure and not so highly optimised setup it was impossible to observe.

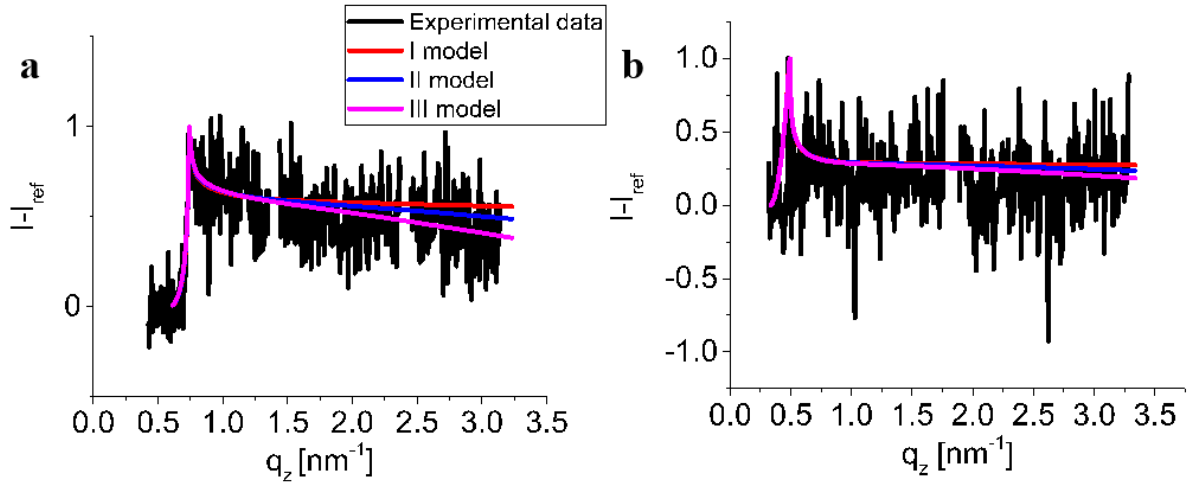

Figure 65: (a) GISAXS off-detector (along q_z) line cuts for the simulated shapes and experimental data at the position with the maximum amount of material obtained from the XRF data. Black curve is scattered data of –spot on the sample 9AUSL1. Other colours-simulations.[132] (b) GISAXS off-detector (along q_z) line cuts for the simulated shapes and experimental data at the position where the maximum amount of material identified from the XRF data. Black curve –spot on the sample 9AUSL2. Other colours-simulations.

Name	Slope 9AUSL1	Slope 9AUSL2
1 model	-0.0289 ± 0.0005	-0.007± 0.00004
2 model	-0.0620 ± 0.0004	-0.022± 0.00008
3 model	-0.1106 ± 0.0003	-0.042± 0.0002
Experiment	-0.094 ± 0.01	-0.036± 0.01

Table 11: Slopes estimated for the linear fits of simulated and experimental data of 9AUSL1 and 9AUSL2.

In the current study, both samples have been found to have three-dimensional structure, as can be seen from the data in Table 11. According to the theory, one of the probable structures has five atoms in the base, three on the second level and one on the third. Both results are in accordance with the 3D structure and mostly with the III model. However, there is a possibility of clusters with differing shapes and sizes, but due to the fact that GISAXS gives the average characteristics of the sample, the 3D shape with the height of three Au atoms and the radius equal to 0.43±0.06 nm contributes the most. This is in concordance with one of the possible structures of Au_9 clusters suggested by Fernandez *et al.*[6] from DFT calculations and found experimentally by Schooss *et al.*[80]. Both of these studies used these models for clusters in the gas phase which indicates that the soft-landing deposition scheme preserved the 3D geometrical structure of these clusters. A sketch of the possible Au_9 cluster shape obtained from the experimental data is shown in Figure 66.

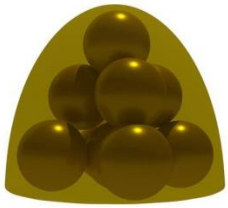

Figure 66: Possible structure of the soft-landed Au_9 on the Si surface according to the experimental data[132].

Sample stability

Additionally to the XRF and GISAXS studies, one year after the GISAXS measurements, the 1AUSL1 sample with 10% ML was investigated using X-ray photoemission spectroscopy (XPS) at the P04 beamline, PETRA III, DESY, Hamburg. This was done to prove the efficiency of the capping layer to be partially an oxygen scavenger for the studied system. The experiment was performed using the ARGUS instrument[158] at 1000 eV photon energy. The photon beam properties and the analyser were tuned to ultimate performance. The beamline bandwidth is roughly 50 meV and the analyser resolution is better than 20 meV. The fitted Lorentzian linewidth γ of the Au $4f_{7/2}$ line was 0.42 eV. The spectra were calibrated against the Au $4f_{7/2}$ line of a clean Au (111) crystal.

The XPS spectrum recorded is shown in Figure 67 It can be seen that the binding energy of the Au clusters agrees very well with the measured data from the Au (111) crystal. Also the binding energy of the Au_9 clusters agrees very well with a comparable, previous experiment by Lim *et al.*[111]. Lim *et al.* have further shown that Au_9 clusters can be oxidised in an activated oxygen atmosphere resulting in a large chemical shift of the Au 4f lines, showing even more reactivity than smaller clusters[159]. The current experimental results therefore imply that the Au clusters remain unoxidised due to the capping layer even after one year of storage under ambient conditions and after several hard X-ray measurements. Therefore possible effects such as beam damage or alloying with the capping layer can be ruled out.

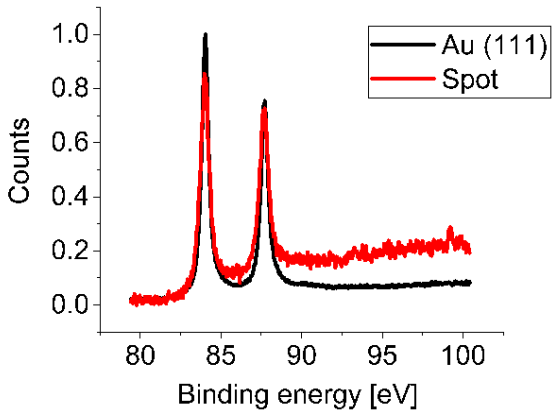

Figure 67: XPS spectra for Au_9 spot and Au (111) crystal at Au $4f_{7/2}$ line[132].

3.2.4. Au_5 and Au_7

In this part of the chapter two samples: 5AUSL1 and 7AUSL1are discussed. They both have 10% ML coverage, but 5AUSL1 contains clusters consisting of five atoms while 7AUSL1 contains clusters consisting of seven atoms.

The first subsection presents the XRF spectra observed for 5AUSL1 and their correlation to the GISAXS contour plots in both directions, while the second subsection presents the same for 7AUSL1. The last subsection compares the structural characteristics of the two systems, as well as the limitations of the experiment for such objects.

Investigation of 5AUSL1.

As is shown in Figure 68, the 10% ML Au_5 sample was easy to detect using XRF. In this case, the scanned area was also selected to be large enough to find the spot. Although, scans with so many steps (84) and several repetitions took a longer time, this was necessary for the detection of the spot (as a very weak signal was expected due to the small number of atoms in this sample). XRF yield as a function of the sample position for the energy of 9.6 keV (L_α) is presented in the Figure 68**a,** where FWHM is 0.54±0.01 mm. The XRF signal for the spot (black curve) and Si (red) is shown Figure 68**b**. It can be observed that on the Si position in 5AUSL1 there is a signal at 9.6 keV, although much less pronounced. It means that small amounts of gold are scattered over the entire surface. This sample did not have a gold marker on the surface prior to deposition of ultrasmall clusters.

In Figure 69 contour GISAXS plots along q_y and q_z are shown. A correlation between the geometrical position of the maximum of gold spot at 6.8 mm on the substrate surface in the XRF and GISAXS data is observed. A very high intensity area around q_y=1.3 nm^{-1} in Figure 69**a** indicates that the detected signal should be from a large structure, possibly an aggregate. Interestingly, an intense signal on the spot position in the region of higher q_y values (-3.4 – -2.4 nm^{-1}) is visible in Figure 69**b** (marked with white ellipse). This observation does not correlate with the assumed small scattering volume of five gold atoms.

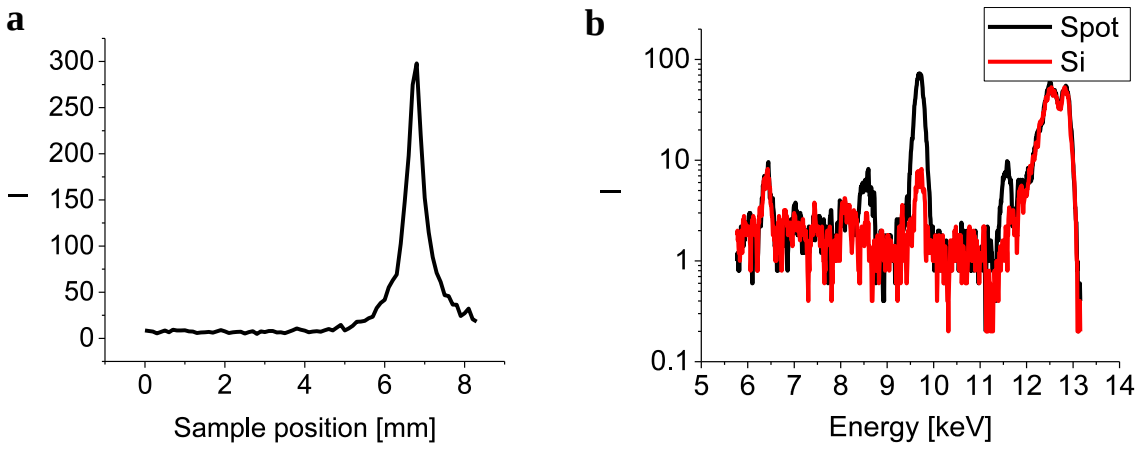

Figure 68: (a) XRF spectra of the sample at the L_α Au line as function of lateral distance on the Si surface. At a distance of 6.8 mm on x-axis maximum of XRF signal stemming of the Au_5 spot. (b) XRF spectra of the sample for Au_5 spot (black) and Si (red).

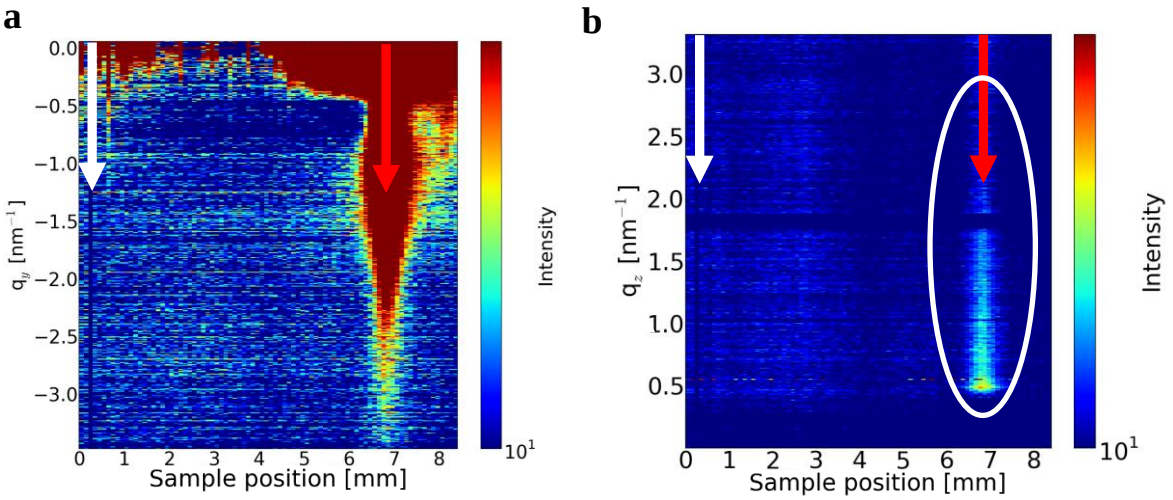

Figure 69: (a) Contour plot of the out-of-plane cuts (along q_y) derived at the Si Yoneda peak (q_z=0.54 nm^{-1}) for different positions on the substrate. The white arrow indicates the subtracted data frame, the red one- the maximum of the Au_5 spot. (b) GISAXS off-detector (along q_z) line cuts at q_y from -3.4 to -2.4 versus the position on the substrate. The white arrow indicates the subtracted data frame, red arrow the maxima of the Au_5 spot.

Investigation of 7AUSL1.

Consistently the same systematic approach was used for 7AUSL1 as was used for the samples described above. In Figure 70 XRF data is presented with the yield at 9.6 keV depending on the sample position in the Figure 70**a** and fluorescence pattern for three different positions in Figure 70**b**. It is clearly visible that the gold marker is at 8.2 –10 mm, on the right from the spot maximum at 6.7 mm with FWHM of 1.16±0.02 mm. Interestingly, the width of the deposited spot is two times higher than for 5AUSL1 and slightly smaller than of 9AUSL2.

GISAXS contour plots depending on the sample position are presented in Figure 71. Figure 71**a** shows combined line cuts along q_y, while long cuts along q_z are shown in Figure 71**b**. Data obtained at position 3.4 mm was used for background subtraction. For the sample with only seven atoms per cluster (7AUSL1) it is expected the signal should be rather weak in comparison with 9AUSL2 and 11AUSL1 (nine and eleven atoms per cluster respectively). There contour plot along q_z had low intensity, see Figure 71**b**. Contour plot along q_z at q_y=-3.4—2.4 nm in Figure 71**b** shows unexpectedly strong signal in the vertical direction (marked with white ellipse). This also can be an indication of a structure with higher scattering volume than clusters consisting of seven atoms.

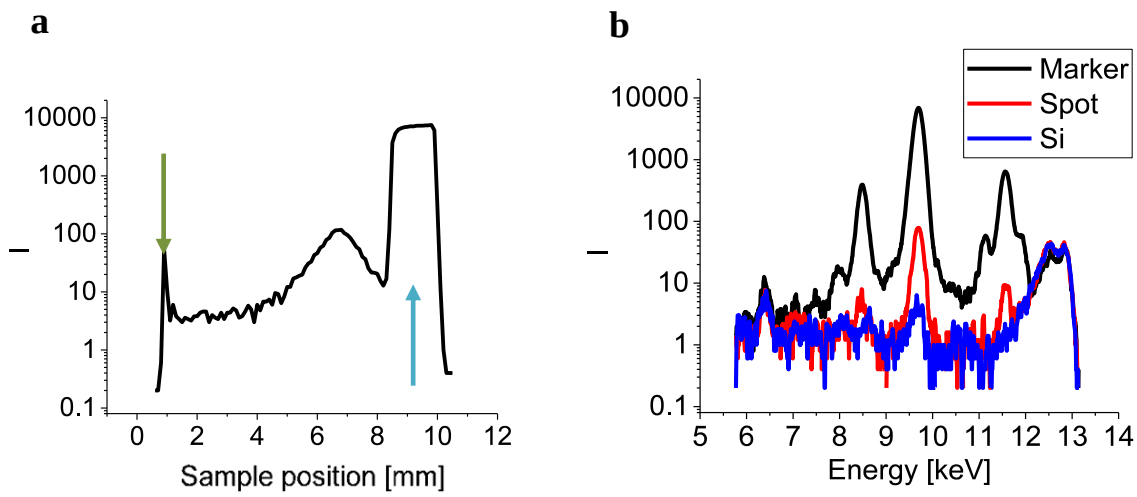

Figure 70: (a) XRF spectra of the sample at the L_α Au line as function of lateral distance on the Si surface. At a distance of 6.8 mm on x-axis where the maximum of XRF signal stemming of the Au_7 spot. Green arrow-position outside of the sample, blue-marker. (b) XRF spectra of the sample for the Au marker (black), Au_7 spot (red) and Si (blue).

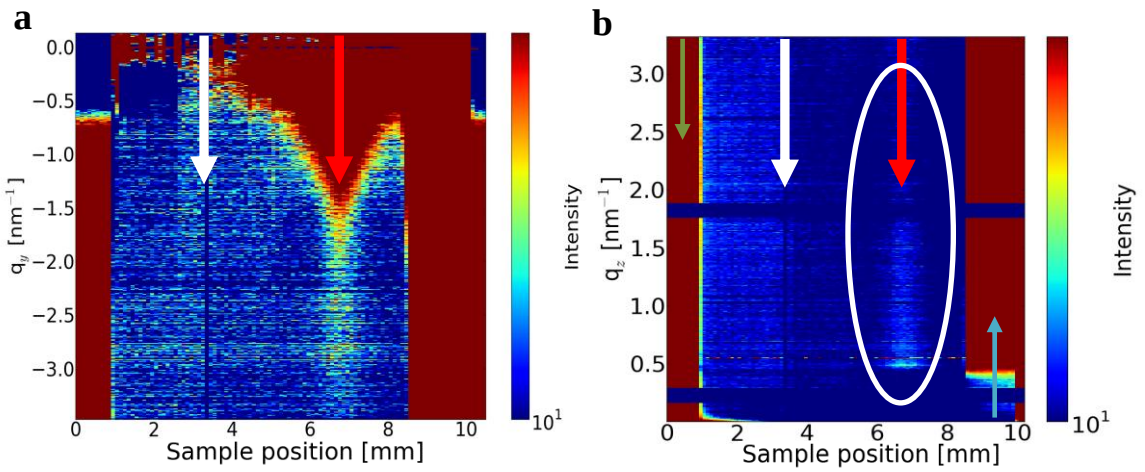

Figure 71 (a) Contour plot of the out-of-plane cuts (along q_y) derived at the Si Yoneda peak (q_z=0.54 nm^{-1}) for different positions on the substrate. The white arrow indicates the subtracted data frame, the red one- the maximum of the Au_5 spot. (b) GISAXS off-detector (along q_z) line cuts at q_y from -3.4 to -2.4 versus the position on the substrate. The white arrow indicates the subtracted data frame, red arrow the maxima of the Au_7 spot, green –area outside of sample, blue-marker.

Structural analysis of 5AUSL1 and 7AUSL1.

In Figure 72 GISAXS line cuts for both 5AUSL1 and 7AUSL2 are compared. Horizontal cuts at the positions of Si and of the spot with effective thickness of around 10% ML are shown for both samples**.** Fitting of the data in the q_y range from -3.5 to -2 nm^{-1} with a Lorentzian function was performed to find the best-fitted maximum, corresponding to very small structures. This produced the positions at 2.95 nm^{-1} in the case of 5AUSL1, and 2.92 nm^{-1} for 7AUSL1 (fits are provided in the Appendix: Section 5.8). The calculated values of radii (R) and the number of atoms/per cluster (N) are listed in Table 12. The N value estimation indicated that the probable $q_{y,max}$ position is outside of the detector area, if we assume our clusters to be 3D. Therefore, only dual clusters can be observed from this data. Arrows in Figure 72 **a,b** mark the position of signals which are caused by larger structures, possibly arising from aggregated clusters.

In Figure 72**c,d** vertical cuts for the q_y range of -3.4 – -2.4 nm^{-1} are depicted for 5AUSL1 and 7AUSL1, respectively. Similar strategy to the height analysis of 9AUSL1 and 9AUSL2 was tested in this case. Simulation with IsGISAXS using estimated radii and varying the height as Figure 64 was done. The comparison of the resulted slopes between the experimental data and the simulations is listed in Table 13. Both show tendency for the 3D structures, which confirms the assumptions that only aggregates can be influencing the signal in that q_y range. Interestingly, that 7AUSL1 structure is exceedingly high compared to the one of 5AUSL1, which should be due to Au_7 being bigger than Au_5. However, in both cases the structure is higher than three atoms piled up on each other, which cannot be possible for such small clusters.

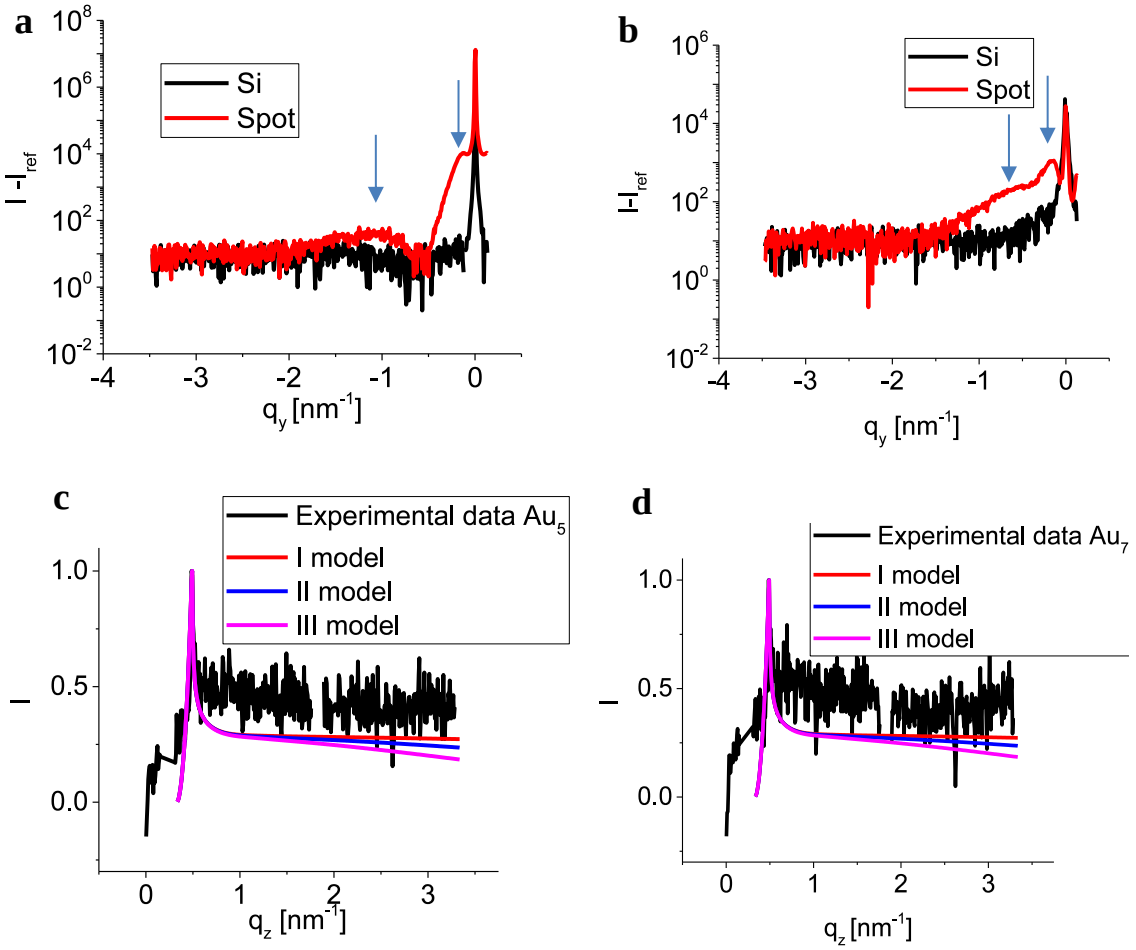

Figure 72: (a) GISAXS out-of-plane (along q_y) line cuts at the position with the maximum amount of material identified from the XRF data and on the Si position. Red curve- 5AUSL1 spot, black curve- Si. (b) GISAXS out-of-plane (along q_y) line cuts at the position with the maximum amount of material identified from the XRF data and on the Si position. Red curve-7AUSL1 spot, black curve- Si. (c) GISAXS off-detector (along q_z) line cuts for the simulated shapes and experimental data at the position with the maximum amount of material identified from the XRF data. Black curve – 5AUSL1 spot, red curve - hemispheroids with the height of 1 Au atom, blue curve- hemispheroids with the height of 2 Au atoms, pink - hemispheroids with the height of 3 Au atoms. (d) GISAXS off-detector (along q_z) line cuts for the simulated shapes and experimental data at the position with the maximum amount of material obtained from the XRF data. Black curve –7AUSL1 spot, red curve - hemispheroids with the height of 1 Au atom, blue curve- hemispheroids with the height of 2 Au atoms, pink - hemispheroids with the height of 3 Au atoms.

Name	5AUSL1	7AUSL1
q_y [nm^{-1}]	2.88±0.05	2.92±0.05
R [nm]	0.37±0.01	0.42±0.01
N [atoms/cluster]	8.34±2.36	12.71±3.82

Table 12: Calculated structural values of 5AUSL1 and 7AUSL1.

Name	Slope of 5AUSL1	Slope of 7AUSL1
I model	-0.007 ± 0.00005	-0.007± 0.00006
II model	-0.021 ± 0.00007	-0.021± 0.00006
III model	-0.041 ± 0.00002	-0.041± 0.00002
Experiment	-0.046 ± 0.01	-0.093± 0.01

Table 13: Slopes for the linear fits obtained from simulated and experimental data of 5AUSL1 and 7AUSL1.

The calculated radius values of both clusters are close to these of Au_9, presented in Section 3.2.3, and when combined with a large height and larger number of atoms in a cluster, cannot be due to Au_5 and Au_7 clusters. The solution could be to use the larger detector or reduce the SDD (get a different flight tube built before the detector), which was not possible during this experiment. Also, it is possible that with this coverage such small clusters would not have a sufficient scattering volume to be detected and an increase of the coverage would lead to bigger distortion by aggregates (see Section 3.2.7).

3.2.5. Au_{11}

In this Section, structural investigation of 11AUSL1 is discussed. The scanned area was 9.4 mm, which means that an area larger than the sample itself was measured. It can be clearly seen in the XRF profile of the sample at 9.6 keV shown in Figure 73**a,** at the drop of the intensity at the position from 0 – 0.6 mm. The Au marker is located on the right edge at 8 – 9.4 mm and the spot maximum is at 4.3 mm with FWHM of 1.57±0.04 mm. The XRF yield on the positions of the Au marker Au_{11} spot and Si is shown in Figure 73**b**. It can be seen that the highest intensity is coming from the marker, which had a thickness of 5 nm, the intensity is lower from the spot itself, and the Si surface contained a tiny amount of gold.

In Figure 74 contour plots obtained from the corresponding GISAXS data are shown. Background subtraction was performed in both cases. In the Figure 74**a** the Au marker signal and the area where the sample was not in the beam are located on the positions 8 – 9.4 mm and 0 – 0.6 mm respectively. Following the results from the XRF data, the explanation for such intense signals can be easily given and cannot be misinterpreted. This is an added value of the simultaneous experiment, using several methods. The contour plot along q_y in Figure 74**a**, and the plot along q_z clearly indicates the same position in Figure 74**b**. The along q_z cut in Figure 74**b** was also chosen to be done in the bigger q_y range of -3.2 to -2.4 nm^{-1} to verify the existence of signal in the vertical direction corresponding to the height of small structures.

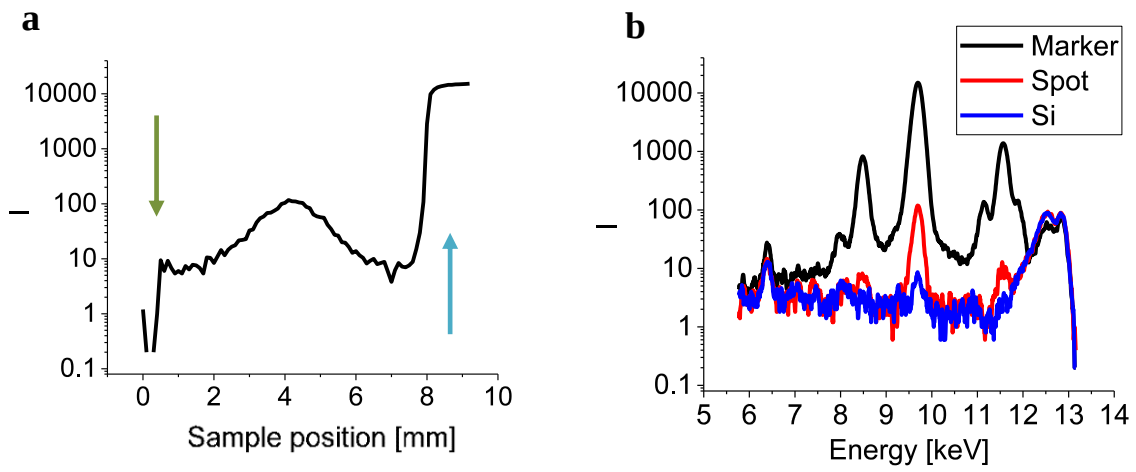

Figure 73: (a) XRF spectra of the sample at the L_α Au line as function of lateral distance on the Si surface. At a distance of 4.3 mm on x-axis is the highest of XRF signal stemming of the Au_{11} spot. Blue arrow-marker, green-outside of sample. (b) XRF spectra of the sample for the Au marker (black), Au_{11} spot (red) and Si (blue).

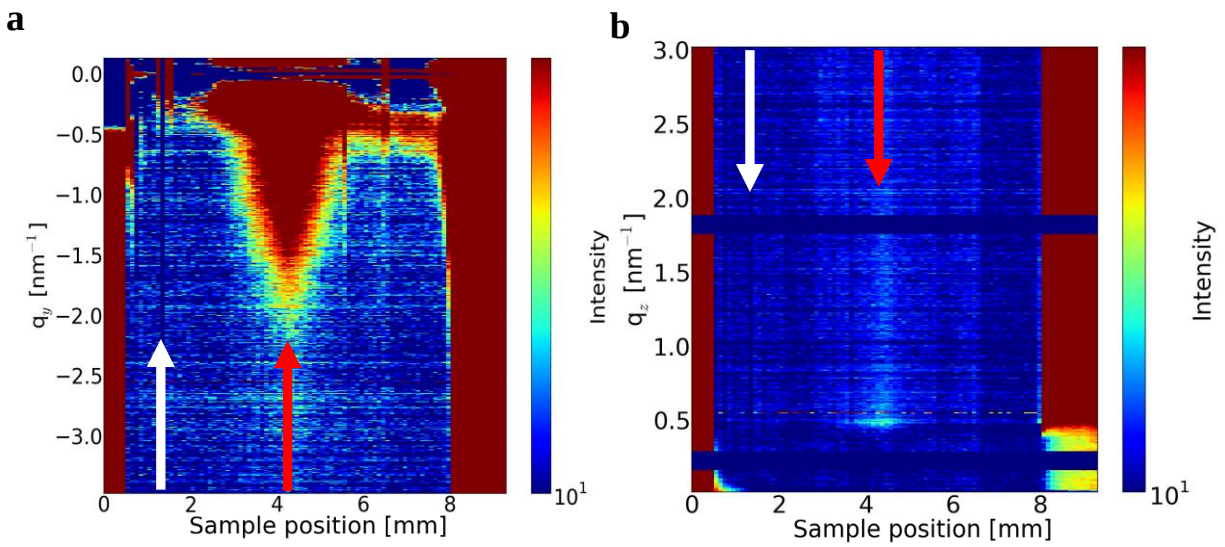

Figure 74: (a) Contour plot of the out-of-plane cuts (along q_y) derived at the Si Yoneda peak (q_z=0.54 nm^{-1}) for different positions on the substrate. The white arrow indicates the subtracted data frame, the red one- the maximum of the Au_{11} spot. (b) GISAXS off-detector (along q_z) line cuts at q_y from -3.2 to -2.3 versus the position on the substrate. The white arrow indicates the subtracted data frame, red circles the maxima of the Au_{11} spot.

The horizontal cuts made at the positions of the 10% ML Au_{11} spot and the Si are shown in Figure 75**a**. The maximum position $q_{y,max}$ was fitted by a Lorentzian and used for the calculations of radius and number of atoms/cluster, and Table 14 contains the results. Afterwards, these obtained radius value and interclusteral distance were used for simulations, in which similar constraints to 5AUSL1, 7AUSL1, 9AUSL1 and 9AUSL2 were applied. The resulting cuts for three models (as in Figure 65) in the vertical direction are shown in Figure 75**b** in comparison with the experimental data (the same sample position as in Figure 75**a** was used). The slope values calculated for each of the vertical cuts are provided in Table 15, a comparison indicate a 3D structure, with the height of 2 – 3 atoms.

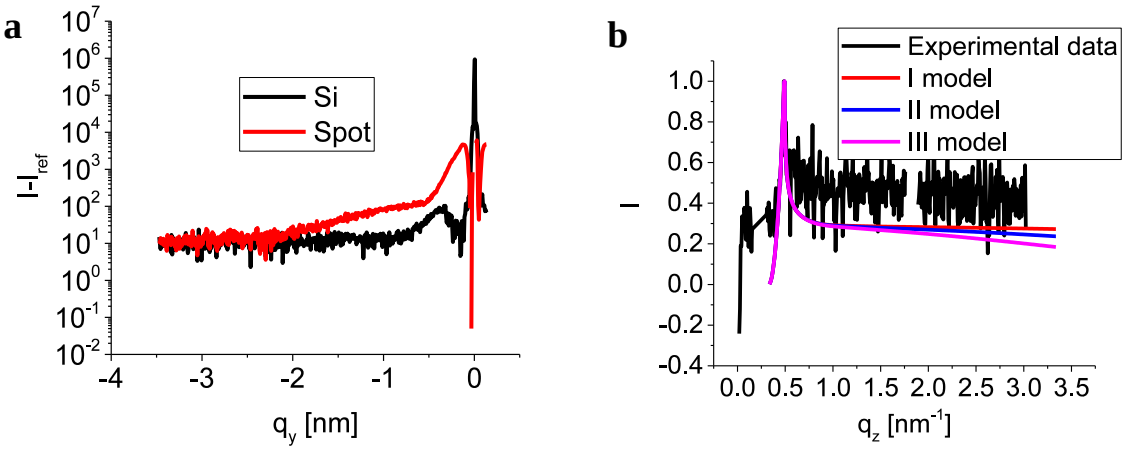

Figure 75: (a) GISAXS out-of-plane (along q_y) line cuts at the position where the maximum amount of material identified from the XRF data and the Si position. Red curve- Au_{11} spot, black curve- Si. (b) GISAXS off-detector (along q_z) line cuts for the simulated shapes and experimental data at the position with the maximum amount of material obtained from the XRF data. Black curve – Au_{11} spot, red curve - hemispheroids with the height of one Au atom, blue curve- hemispheroids with the height of two Au atoms, pink - hemispheroids with the height of three Au atoms.

Name	11AUSL1
q_y [nm^{-1}]	2.76±0.08
R [nm]	0.39±0.02
N [atoms/cluster]	10.3±3.3

Table 14: Calculated structural values for 11AUSL1

Name	Slope of 11AUSL1
I model	-0.007 ± 0.00004
II model	-0.022 ± 0.00008
III model	-0.043 ± 0.00002
Experiment	-0.036 ± 0.013

Table 15: Slopes estimated for the linear fits of simulated data and the experiment for 11AUSL1.

3.2.6. Data analysis using PCA.

In this Section, PCA analysis is presented for the sample 11AU1 (another example is shown in Appendix: Section 5.11). The principles of this method are described in Section 2.2.5. Knowing the position of the $q_{y,max}$ corresponding to the ultrasmall clusters, the aim was to find the maximum variation of the data, which can be expressed only in two dimensions. This could confirm that the spot in that area is on the same sample position, as was shown in XRF data. It would indicate that fitting in the larger q_y area (horizontal cut) was done correctly, despite of the rather low signal intensity.

A small horizontal cut of 100 pixels (q_y=-3.1 – -2.4 nm^{-1}) was made, as $q_{y,max}$ =-2.7 nm^{-1} for 11AU1. It can be seen that there is no significant difference in this cut area from other areas of the detector image (but, this is the detector frame with the highest intensity signal in the area of interest). Then this cut was divided in ten areas, where every 10 pixels were summed. This is shown in Figure 76, where only three areas **a**, **b** and **k** are marked (others are not indicated, but follow the same principle). It should be noted that this was done for every detector image, depending on the sample position. This created a file with 10 features (a – k), shown in Figure 77, which also depend on the sample position. It can be represented by a matrix with 10 columns (features a – b in Figure 77) and with rows- sample positions.

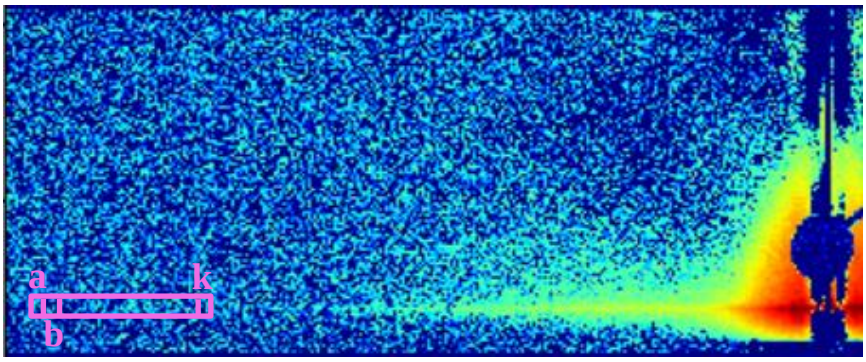

Figure 76: Detector image with an area which was used in PCA analysis.

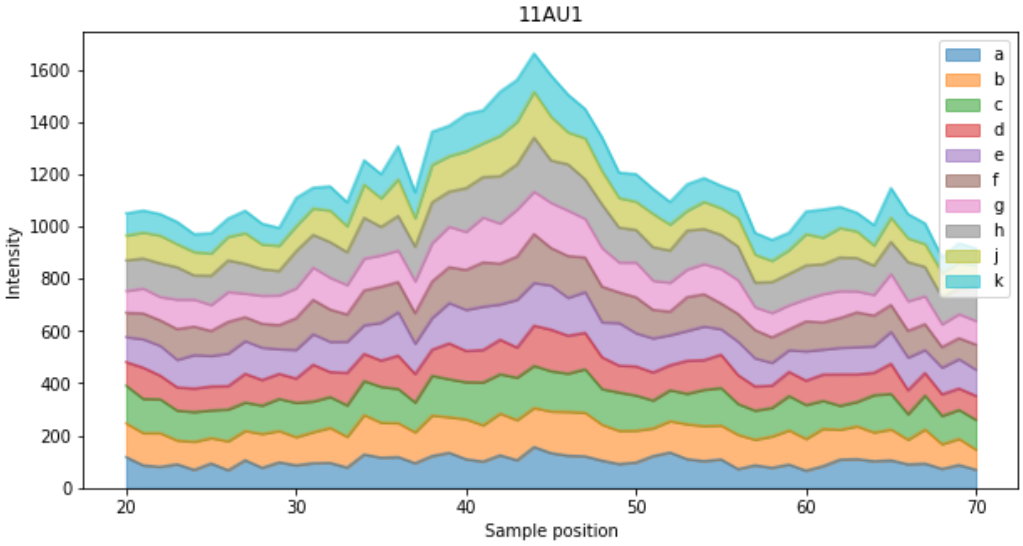

Figure 77: Area graph of features depending on the sample position.

Note: Only sample positions 20 – 70 mm are taken for the analysis, resulting in a date matrix of size 50x10.

Afterwards, two principal components were found using Pandas[147] library in Python for these ten features, which could describe the data the best. By this the data can be presented in two dimensions only, while exhibiting the maximum variance. The data from the spot is marked by a blue ellipsoid in Figure 78. The mechanism of finding these two principal components can be explained by a rotation of the plane created of two vectors (principal components), where the initial cloud of data exhibit the highest variance and hence, exhibit data differences which were hard to see before the rotation.

Now it is evident that there is a signal from the gold spot even in the larger q_y area, as indicated in Figure 79. Principal component 1 shows the maximum variance of the data and the higher intensity signal is at the expected sample position. Although there can be more principal components (their amount should be lower than the amount of features), usually, the first one is the one representing the highest variance and, therefore is sufficient.

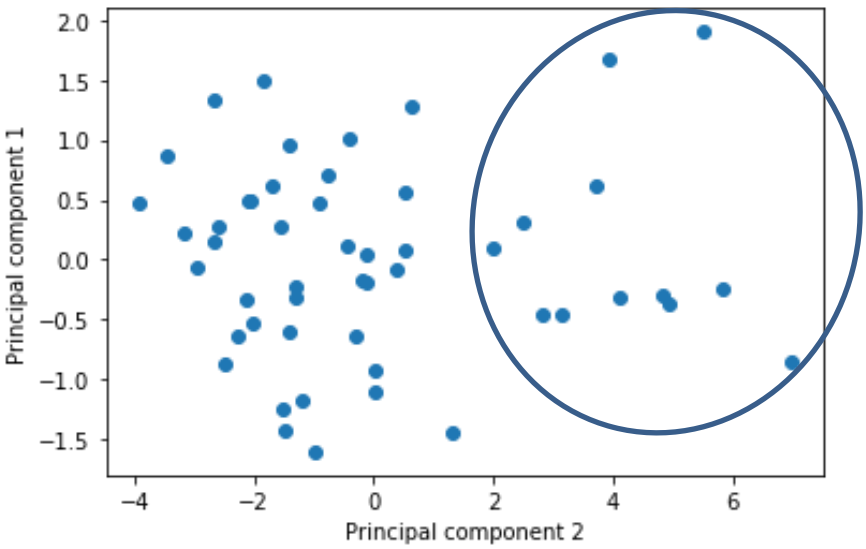

Figure 78: Dependency graph of two principal components.

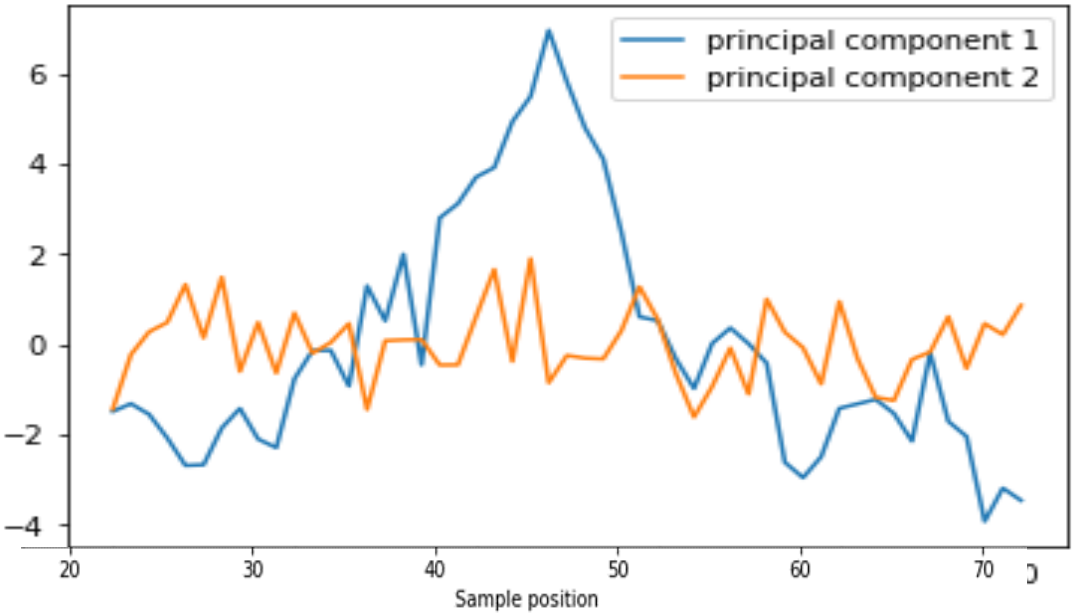

Figure 79: Principal components depending on the sample position.

3.2.7. Aggregation

In this work, during the deposition of ultrasmall size-selected clusters soft-landing[131] scheme was used. Clusters were retarded to have 1eV/atom and the coverage was 10% ML for 1AUSL2, 5AUSL1, 7AUSL1, 9AUSL2 and 11AUSL1, while 1AUSL1 had 50% ML of the deposited material. 1AU1 was neither size-selected nor had a soft landing deposition and deposited particles had and averaged energy around 23.27 eV (calculated for gold sputtering in HASE chamber[160]).

Even in conditions when the amount of soft-landed deposited material was as low as 10%, aggregation can occur. This was proved by the Monte-Carlo simulation, when the limited area had a simulation of randomly "deposited particles". The visualisation of this process is presented in the Figure 80, where the cases of 10% and 50% were tested. The averaged "aggregation" for 10% ML was 6 %, while for 50%ML was 17%. This proved that even in the ideally prepared system it would be difficult to prevent aggregation of the deposited clusters.

Figure 81 shows contour plots of "detector cuts" from the sample position for 5AUSL1, 7AUSL1, 9AUSL2, 11AUSL1. These plots contain information about the height of structures in the system. Since the signal is detected in reciprocal space - the bigger the distance between the peaks (or the minima), the smaller the height in real space. It was expected that such signal might come from larger structures than size-selected clusters, such as their aggregates.

Interestingly, the bigger the cluster size, forming aggregates, the smaller the height. For example in Figure 81 **c,d**, distances between minima are much bigger than in Figure 81 **a,b** (this data has poor statistics, as well as a disturbance in the signal position, so that a reliable quantitative evaluation is not possible). This is understandable, since larger clusters (Au_9 and Au_{11}) are heavier and are likely to have lower cluster mobility. So from these contour plots one can expect that the biggest aggregates are formed by Au_5 and Au_7 (5AUSL1 and 7AUSL1, respectively). This can prove that larger clusters have higher stability, especially deposited with soft-landing.

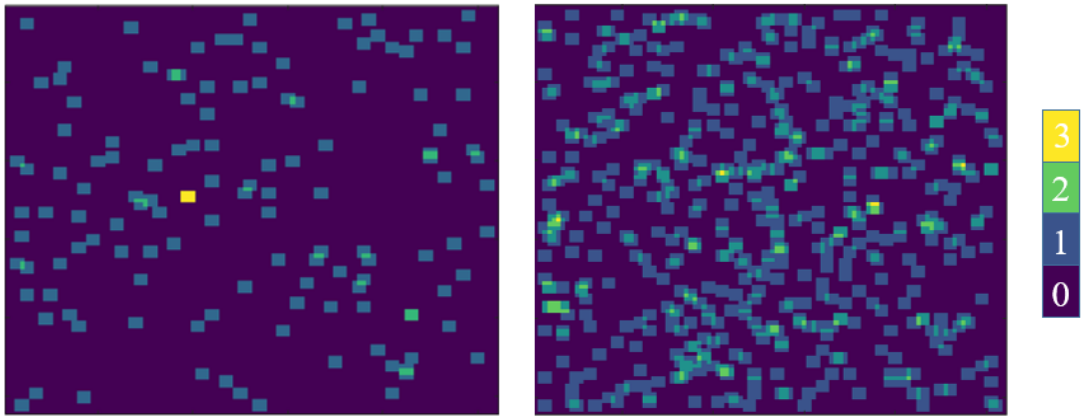

Figure 80: Visualisation of one of the Monte-Carlo simulations. Left- the case of 10% ML. Right- 50% ML. Colour bar shows: zero particles, one particle, two on the same position, three on the same position.

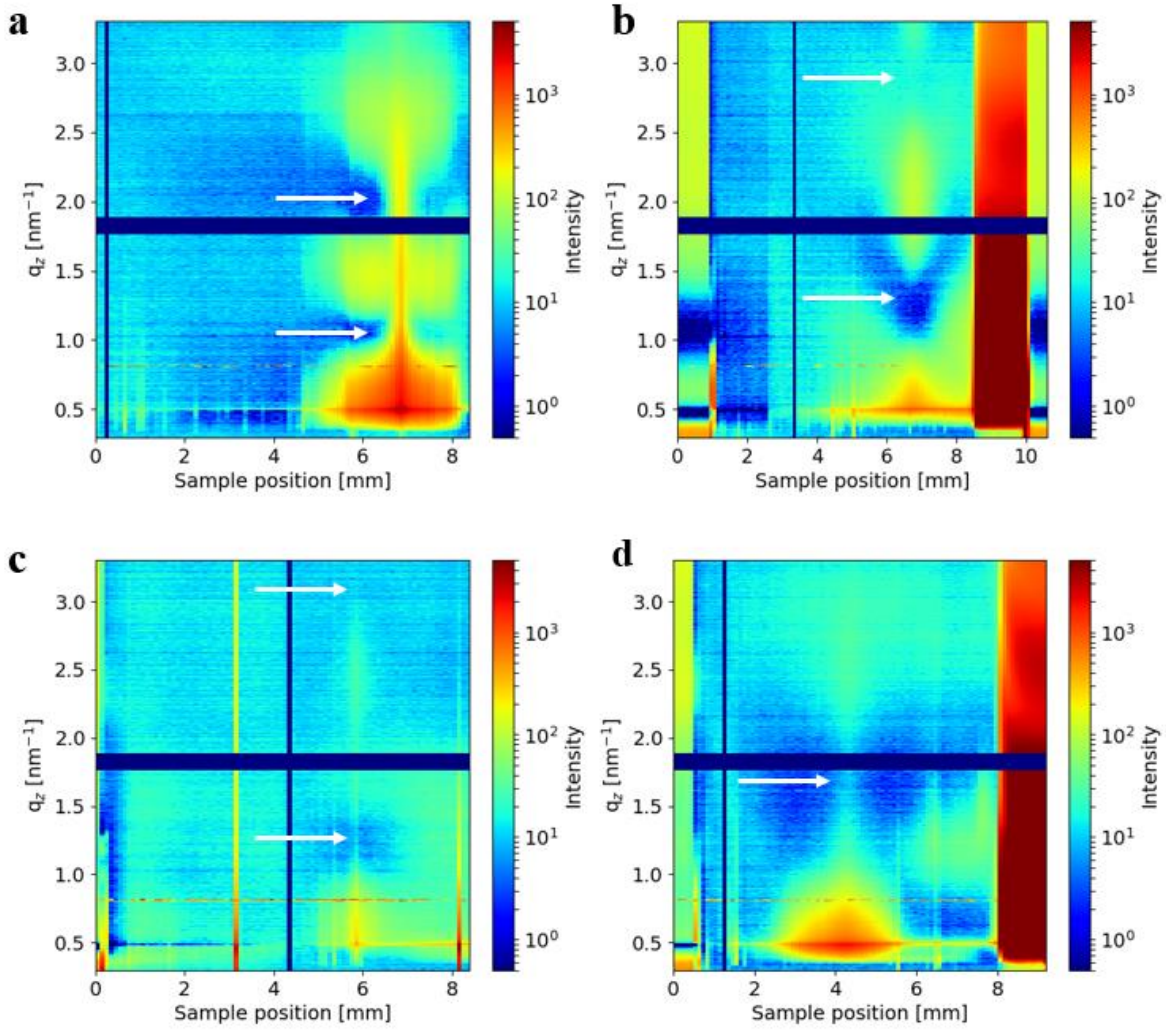

Figure 81: Contour plot of off-detector (along q_z) line cuts at q_y from -0.6 to -0.17 versus the position on the substrate. The white arrow indicates the minima position. a) 5AUSL1; b) 7 AUSL1; c) 9AUSL2; d) 11 AUSL1.

To summarise, even soft-landed deposited clusters with 10% ML coverage can partially aggregate. Aggregated clusters, due to the bigger scattering volume have a significant signal, which is especially noticeable in the area of the smallest q values. The solution for this problem can be to decrease the coverage to 1 – 3% ML, but then the small size-selected clusters would be harder to detect with SAXS. Another option could be to deposit larger clusters which both have a sufficient scattering volume and less likely to aggregate.

3.2.8. Radiation damage

In this Section, one of the very sensitive points of every synchrotron experiment is discussed - radiation induced changes. Whereas for organic samples it is considered extremely important to monitor occurrence of any possible radiation changes, inorganic materials are less likely to be affected. However, since in this work ultrasmall clusters are discussed, during each scan the exposure on one point was restricted to 1s (except for 9AUSL1) and the X-ray scanning was repeated several times. This provided an opportunity to determine if there are any changes caused by radiation and accordingly if only part of the data set should be used for analysis.

In Figure 82 horizontal linear cuts in the form of 2D plots (along q_y) produced at the critical angle of substrate are presented. In this case they depend on the exposure time, which is given as a frame number, where one frame corresponds to 1 s exposure. The first frame in each case was subtracted, so the changes afterwards were more pronounced. In Figure 82 it is clearly visible that the changes occur only in the smaller q range, which indicates that the existing aggregates are not stable and change due to the exposure. In Figure 82 **c,d it** in the frames 63 and 30, respectively, an intensity difference in the whole range of q values can be observed. This difference was caused by beam dumps during scan, which happened while these measurements were performed and the synchrotron beam changed its intensity.

In Figure 83 contour plots similar to the ones in Figure 82 are shown, but the q_y range is chosen according to the expected signal position from the clusters. This was done to confirm that there were no radiation induced changes occurring to the clusters of interest. The optimal exposure time was chosen to be 20 s to have a reasonable signal-to-noise ratio and to account for radiation.

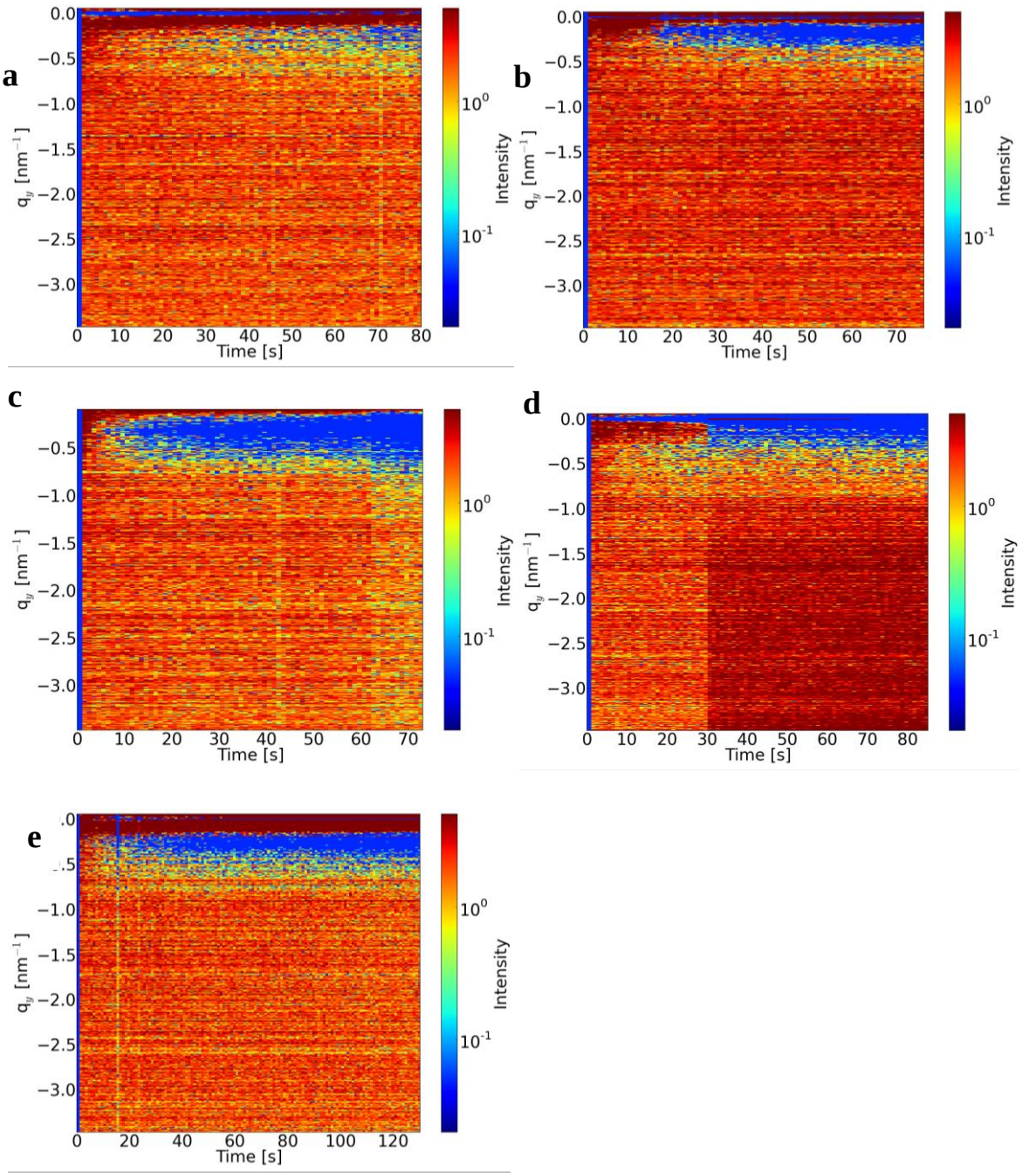

Figure 82: Contour plots of the out-of-plane cuts (along q_y) derived at the Si Yoneda peak (q_z=0.54 nm^{-1}) depending on the exposure time. (a) 1AUSL2. The position of the sample is 4.2 mm, used for the radius estimation of this sample. (b) 5AUSL1 The position of the sample is 7.3 mm, used for the radius estimation of this sample. (c) 7AUSL1 The position of the sample is 6.3 mm, used for the radius estimation of this sample. (d) 9AUSL2 The position of the sample is 6.4 mm, used for the radius estimation of this sample. (a) 11AUSL1 The position of the sample is 4.1 mm, used for the radius estimation of this sample.

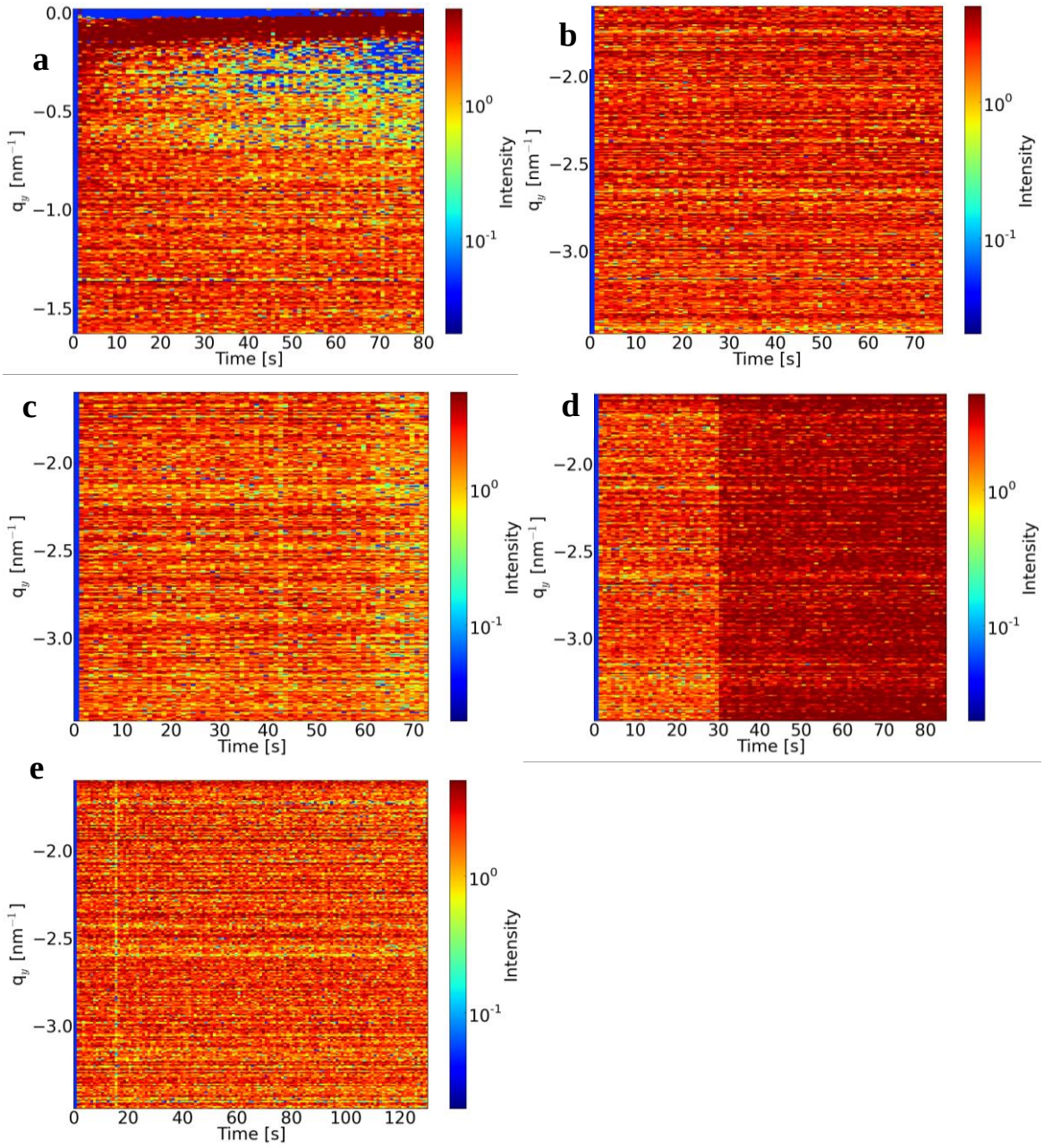

Figure 83: Contour plots of the out-of-plane cuts (along q_y) derived at the Si Yoneda peak (q_z=0.54 nm^{-1}) depending on the exposure time. q_y range is chosen to cover the area, which was used for fitting of the signal of interest in the subchapters above. (a) 1AUSL2 The position of the sample is 4.2 mm, used for the radius estimation of this sample. (b) 5AUSL1 The position of the sample is 7.3 mm, used for the radius estimation of this sample. (c) 7AUSL1 The position of the sample is 6.3 mm, used for the radius estimation of this sample. (d) 9AUSL2 The position of the sample is 6.4 mm, used for the radius estimation of this sample. (a) 11AUSL1 The position of the sample is 4.1 mm, used for the radius estimation of this sample.

To describe what is happening to the aggregated particles when the sample under exposure to X-rays, Figure 84 and Figure 85 are considered. In Figure 84 the range of smaller q_y values is shown. It can be seen that after an exposure time of around 10 s, the scattering intensity in the region -0.2 to -0.5 nm^{-1} decreases strongly, however the scattering intensity in the range of 0 to -0.1 nm^{-1} increases. This can be explained by the growth of aggregated clusters, which is demonstrated in Figure 85. There the position

of $q_{y,max}$ shifts to smaller values with increasing time, until the growing structures are too large to be visible within this experiment. This means that the aggregates move and due to the core excitation the particles gain a lot of energy which might result in a melting of the clusters and a subsequent alloying with the Al capping layer. Hence, from the scattering picture the size of the clusters will increase.

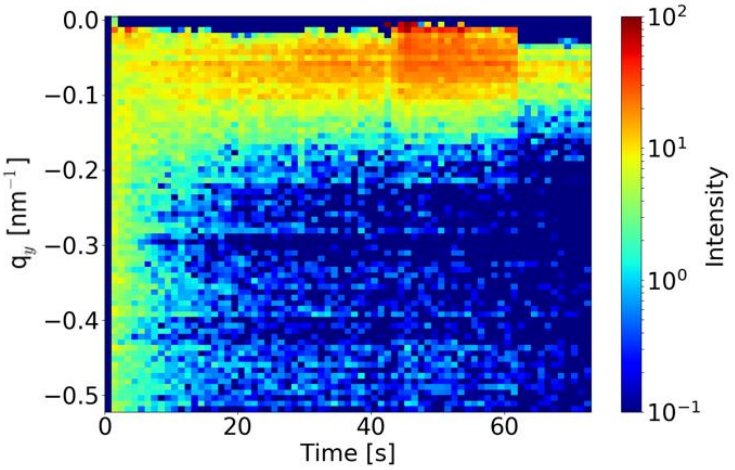

Figure 84: 7AUSL1 Contour plot of the out-of-plane cuts (along q_y) derived at the Si Yoneda peak (q_z=0.54 nm^{-1}) depending on the exposure time.

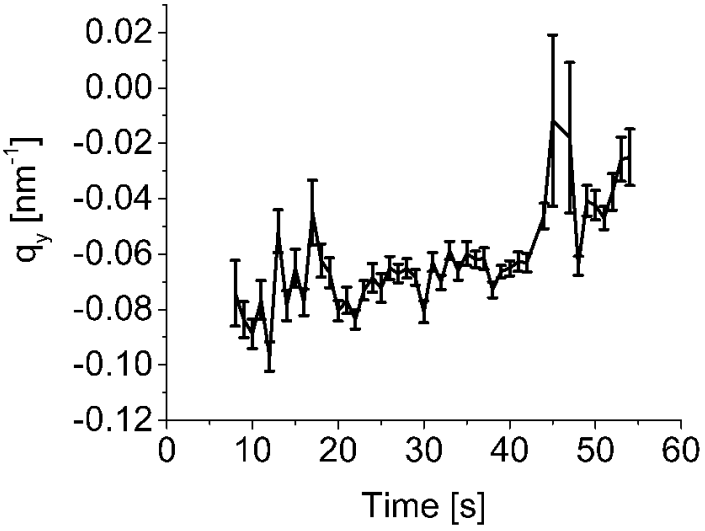

Figure 85: Development of the $q_{y,max}$ position for 7AUSL1 depending on the exposure time.

3.3. Discussion

The main topic of this research was to obtain knowledge about the morphology of two nanosized gold containing systems. In this subchapter, the main findings from both investigated systems are discussed. Firstly, the geometrical structure of small bimetallic AuAg clusters in comparison with pure metals during deposition is provided. Secondly, findings of the geometrical structure for only few atoms in a cluster are presented.

Bimetallic AuAg clusters

As was mentioned in the literature review, bimetallic clusters of Au/Ag are extremely interesting for investigation due to their unique physical and chemical properties, which differ their behaviour from pure metal systems. There is also the possibility to tune the structure and therefore the properties of such systems by varying the ratio of two metals. However, usually, it is done by single alloy target deposition, thus it can increase the control during preparation to use two pure metal targets and vary the deposition rate of each separately. In this work, these kind of structural changes were observed in real time. An initial objective of the project was to determine the cluster radii and shape during the production of bimetallic AuAg sample with equal deposition rate of each metal, but only until the effective thickness reached 10 nm. The first question in this study sought to determine how these characteristics were comparable with pure metal behaviour of the same deposition rate. The second question was to understand if the application of the moderate temperature (lower than the melting temperature of these two metals) could influence the structure. The third question was to observe differences in the optical properties of Au/Ag compared to those of pure metal.

The finding of the pure Au deposition is consistent with the work of Schwartzkopf *et al*.[31] done, using the same sputtering chamber, which claimed that the structure of deposited Au clusters is hemispherical and the percolation threshold happened at 5.5 nm effective thickness. In this work, percolation happened at 6 nm, which can be explained by the difference in the deposition rate. For the samples studied in this work, the hemispherical shape, radius and interclusteral distances at 10 nm effective thickness are in agreement with their study (see Figure 36, Figure 38). The outcome of the investigation of pure Ag does not agree with the work of Santoro *et al.*[30] and Yu *et al.*[161], who also used the HASE deposition chamber. They both measured an Ag percolation threshold occurring around 5 – 6 nm effective thickness. In the present work, it was not reached even at 10 nm effective thickness. Furthermore, there were no appearance that Ag can reach percolation threshold at 5– 6 nm effective thickness, even under an applied temperature of 185° C. This can be clearly seen in Figure 37, where the alternate deposition is presented (AuonAg, AuonAgA) and at 5nm effective thickness there was only pure silver deposited. This significant difference can be explained by high reactivity of Ag and therefore extreme sensitivity to the deposition conditions, since the Ar pressure was slightly different and the sputtering rate much slower. There is an indication that growth of the Ag nanoparticles depend on the growth rate, while it does not

affect Au growth. In accordance with work of Yu *et al.*[161], the change of the initial hemispherical shape occurred and the flattened structure was also predicted in this work, but at 5 nm effective thickness rather than at 7.6 nm.

The most interesting and important finding was that bimetallic clusters AuAg "inherit" from both metals, when at 10 nm effective thickness the flattened structure, influenced by Ag, have the value of the radius and interclusteral distance close to Au (see Figure 38). Another important finding was that percolation threshold happened already at 3.3 nm effective thickness. When heating was applied during the deposition, even as low as 185° C, percolation was not observed for bimetallic AuAgA sample. In this case, final cluster had a hemispherical shape, like pure Au but their radius was closer to Ag. AuAg deposited in room temperature showed very high reflectance in the range of 400 – 800 nm in comparison with pure metals, which shows that such compound structures can be useful for optical applications, but more research with various metal ratios is needed.

Ultrasmall size selected Au_n clusters

In contrast to the study of bimetallic AuAg clusters very little was found in the literature on the experimental investigation of morphology of ultrasmall deposited size-selected Au clusters. While theoretically, some possible structures of ligand-free Au clusters were proposed, e.g. by Schooss *et al.*[80], they only applied for the gas phase configuration. At the same time, Au clusters consisting of only few atoms in a cluster have been found to exhibit significant catalytical properties[83], which are extremely sensitive to the amount of atoms in a cluster, reported by Lim *et al.*[159,162,163,111]. Considering that on this size-scale morphology plays an important role, when "each atom counts"[20], the present study was designed to obtain geometrical structure of size-selected deposited Au clusters of 5,7,9 and 11 atoms in a cluster. This research set out with the aim of assessing the optimal experimental parameters in the sample preparation and investigation; since the challenges of protecting such clusters prior to investigation as well as during had to be addressed. Due to the fact that clusters were deposited only on the part of the substrate and also had only 10% ML coverage, reliable investigation procedure was crucial. The next important challenge was to prove if the soft-landing conditions[131] are imperative for the preparation of mass-selected clusters.

A capping layer of 5 nm Al was applied to protect ultrasmall size-selected Au clusters after deposition in UHV conditions. This layer has proved to be both transparent to X-rays during investigation and efficient in protection of such clusters even after a long storage time outside of vacuum conditions (reported[132]). The used experimental setup, which combines simultaneous GISAXS investigation with XRF method (provided in Figure 23) proved to be effective for investigation of low size-selected atomic sized structures. It was somewhat surprising that ultrasmall clusters, being metallic and protected by a capping layer were prone to radiation induced changes. To solve this issue, instead of a long time exposure per point short exposure in combination with permanent motion was used. Prior to the

summation of signal at each sample position, they were examined for changes. This allowed having the highest possible signal to noise ratio, while remaining unaffected by radiation. To prove that soft-landing preparation scheme was important for the final structure, monoatomic deposition of 50% ML was done applying it and compared with RF-magnetron sputtering. Sputtering produced larger clusters with almost three times bigger interclusteral sizes, which can be a proof that soft-landing is important for deposition.

These precautionary measures made the geometrical investigation of ultrasmall clusters possible. One of the main questions addressed was to understand if such clusters has a tendency to form 2D or 3D structure. Previous studies proposed that deposited clusters of Au_8 on the oxide substrate might form a 3D structure[34], but until now no such experimental results of ligand free deposited Au_9 and Au_{11} were reported. By Sanchez *et al.* it was shown that these clusters have pronounced catalytical properties[34] and hence are promising candidates for investigation. The main experimental result was that both Au_9 and Au_{11} clusters deposited on the Si/SiO_2 substrate have a preferable 3D shape. Another important result was that it was possible to reproduce this result for two different prepared samples of Au_9 and the estimated radii (0.38±0.02 nm and 0.43±0.06 nm) were similar within the error bar. The evaluated number of atoms in a cluster was also in accordance with the expected value. The possible explanation of the small difference between these two Au_9 samples could be that the on with the smaller radius was prepared in one year after the other one. Therefore, the challenges in preparation and investigation were addressed better. For Au_{11}, a radius of 0.39±0.02 nm and the number of atoms in a cluster 10.3±3.3 were obtained, however this evaluation could not be performed for Au_5 and Au_7. The reason for this was the limitation of the detector size and position, which could not be addressed during this work. While the inability to completely characterise Au_5 and Au_7 is disappointing, it opens opportunities for the follow up research to address and solve these issues.

Indeed, this work does not claim that the geometrical structure of the objects discussed, when deposited on a different substrate or having various capping layers will remain the same. The influence of the substrate on both deposited systems can be an important issue for the future research projects. Promising candidates as substrates in the study of the bimetallic systems can be polymers, while for ultrasmall clusters influence of the of other oxide supports on the morphology can be tested.

It was proved that the investigation of ultrasmall gold clusters is possible, using the proposed experimental approach. This could lead to various opportunities of research, starting from promising Au/Ag systems, when the shape of the cluster can be tuned by changing the metal ratio. This showed to be significant even for larger clusters, as reported in the present work, therefore higher control operating only few atoms should be possible. Another interesting object can be a platinum system, as platinum alloys (CoPt or FePt) exhibit magnetic properties and tuning can be done by adding second metal, for example cobalt. Another promising candidate is copper, which can be studied using the exact same experimental setup and investigation approach.

4. Summary and Outlook

The objective of the current study was to determine the geometrical structure of two Au systems deposited on Si/SiO_2: bimetallic Au/Ag clusters and ultrasmall size-selected Au_n clusters and adatoms (n = 5, 7, 9, 11). Real time investigation of bimetallic structures implied comparison with the pure Au and Ag deposition and influence on temperature on the growing Au/Ag clusters was investigated. Ultrasmall size-selected clusters of choice had 5, 7, 9 11 atoms in a cluster, their geometrical sizes were compared between each other, and their possible shapes have been investigated.

In the work main findings of the real-time investigation of Au/Ag are reported. The study has shown that bimetallic Au/Ag (AuAg) clusters differ in shape and cluster size not only from pure metals but also upon heating (AuAgA) to as low as 185 °C. At the final effective thickness of 10 nm AuAg inherit cluster size from Au influence and the ellipsoidal shape from Ag, while heated AuAgA has the biggest size between all and hemispherical shape inherited from Au. At 1 nm effective thickness, their cluster shape is hemispherical and have similar radii, while at 5 nm Ag tends to have an elongated ellipsoidal shape. Another interesting finding is that AuAg reach percolation threshold earlier than all of the other discussed samples. Codeposited Au/Ag also proved to be a promising candidate for optical application, exhibiting high reflectance in the wavelength range 400 – 800 nm than pure metals. Alternately deposited Au on Ag in room temperature and heated also show differences in the resulted cluster sizes, where the heated sample is the largest. These results add knowledge to the rapidly expanding field of compound materials. The insights gained from this study may be of assistance to plan future extensive experiments on the structure of codeposited clusters with different metal ratio. Future development could include the investigation of other physical properties of these AuAg systems in comparison to pure metals. Despite its exploratory nature, this study offers some insight into the area of a higher controllable experiment using co-deposition. It also leads to new questions about the structure of ultrasmall bimetallic clusters. For example, since the shape of clusters consisting of hundreds and thousands of atoms is 3D, is it possible that clusters consisting of less than 10 atoms are also 3D. To address this, a first step would be to investigate ultrasmall clusters of pure Au.

The new type of the morphological investigation of ultrasmall deposited Au clusters is introduced. The sample preparation method was configured to allow sample investigation *ex situ*, using GISAXS. The proposed simultaneous combination of XRF and GISAXS at a synchrotron beamline was tested to prove the advancement of these methods in investigation of low mass selected atomic sized geometrical structures. The most obvious finding to emerge from this study is that Au_9 and Au_{11} have a 3D structure after deposition on Si/SiO_2 and their radii were calculated. This is the first experiment proof of a 3D structure, which has been proposed theoretically for Au_8 on MgO by Sanchez[34]. Another important result is that the structure of ultrasmall clusters of the same sizes is reproducible, which was demonstrated on the example of Au_9. The used Al capping layer also proved to be efficient in cluster protection, when even one year after sample preparation gold can be detected at the same sample position. It was not

possible to determine the radii of Au_5, Au_7 due to the limitations of the experiment. However, the most important limitation lies in the fact that radiation induced changes took place after certain exposure time, which was avoided in the data but decreased the signal to noise ratio. Another complication was the aggregation of these clusters, which was unable to be avoided but was accounted for in the analysis.

This study has been the first attempt to examine the geometrical structure of ligand-free ultrasmall mass selected clusters Au_5, Au_7, Au_9 and Au_{11}. Notwithstanding these limitations, the study shows that it is possible to investigate geometrical structure of ultrasmall deposited clusters with 10% ML coverage using synchrotron GISAXS. One of the possibilities of solving the aggregation issue is to decrease the coverage to 1 – 3%, but then the signal will be not sufficient for the analysis and longer exposure would only lead to radiation induced changes. During these experiments there was always a large footprint from the X-ray beam on the sample and only a prediction for the sample average could be given. Hence, some clusters might have a 2D or other 3D structures on the surface. Therefore, new diffraction limited synchrotron sources, with higher brilliance and smaller beam size will be required to perform experiments on single particles on the surface. Single particle imaging of such ultrasmall objects can be a challenging task to perform. This would require a beam as small as 2 – 3 nm in size, which would then allow detection of one separate cluster. The currently developing PETRA IV synchrotron could address this requirement and therefore the experiments carried out in this work can be an exemplary one for the future source.

Another interesting question to be addressed in the future is the influence of the capping layer, for example which structural differences will ultrasmall clusters have when there is a graphene or polymeric films deposited on top. A further question could be the influence of the substrate, where one can compare Si/SiO_2 with MgO, TiO_2 or even organic films. Moreover, following from this study an important step will be the investigation of such structures *in situ*, where it will be clearly visible if the capping layer affects the structure of the ultrasmall size-selected clusters after the deposition.

5. Appendix

5.1. Sauerbrey equation

To calculate the rate of deposition was used Sauerbrey equation[124].

$$\Delta f = -c_f \Delta m$$

Equation 20

Δf- frequency change [Hz], Δm- mass change [g]. For the Inficon crystal one has a sensitivity factor of the crystal - c_f

$$c_f = \frac{2f_0^2}{A\sqrt{\mu_q \rho_q}} = 0.081 \ \frac{Hz}{ng} cm^2$$

Equation 21

Where f_0 is resonant frequency [Hz], Δf- frequency change [Hz], Δm- mass change [g], A- active crystal area [cm^2], ρ_q- density of quartz (2.648 [g/cm^3]), μ_q- shear modulus of quartz crystal (2.947×10^{11} [$g\ cm^{-1}\ s^{-2}$]). Values were taken from the QCM supplier Inficon (Switzerland)[164].

With this the deposition rate is:

$$\varepsilon = \frac{\Delta m}{\rho_t}$$

Equation 22

ρ_t- density of the target material. Δf value was recorded with QCM and the averaged during 1 min value used.

5.2. XRF calibration

XRF was measured for all the samples in Section 3.2. Prior to the experiment calibration of the detector was done using Americium source with several foils inserted. In Figure 86 the calibration data from one of the beamtimes is provided. Some of the element emission lines are marked. In the K_α line of Rb due to the resolution cannot be separated $K_{\alpha 1}$ (13.39 keV) and $K_{\alpha 2}$ (13.33 keV). The same applies for K_α of Cu ($K_{\alpha 1}$ = 8.05 keV and $K_{\alpha 2}$=8.03 keV). The energy emission values are from the X-ray data booklet[155]. The calibration value (slope keV/channel) of 0.00716 was used for 1AUSL1 and 9AUSL1, while 0.00739 for others.

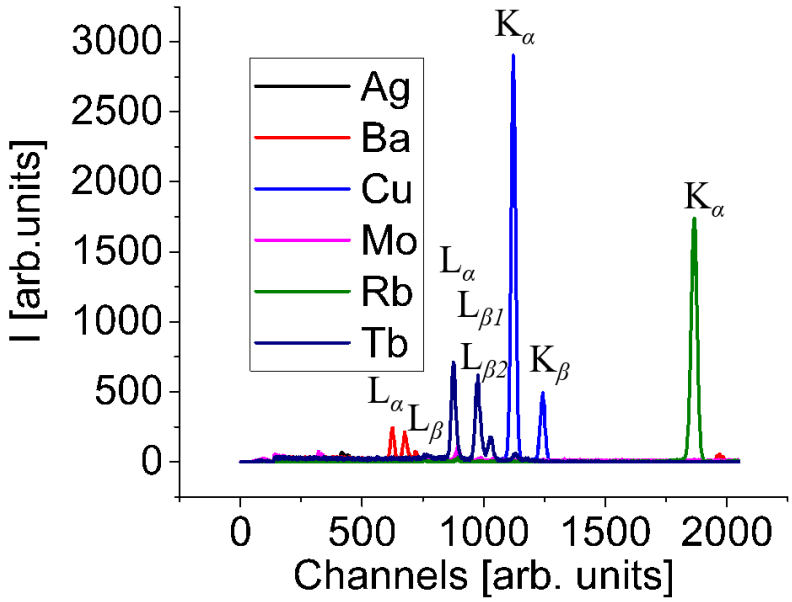

Figure 86: Calibration XRF spectra.

5.3. WAXS data analysis

For 1AUSL1 and 9AUSL1 samples GIWAXS measurements were performed. Description below is also provided in the supplementary information[132].

In GIWAXS data analysis, one usually extracts intensity distributions by radial integration to obtain a diffractogram, where peak positions and shape can give the preferred crystallographic lattice according to Bragg´s law and the crystallite size of the object according to Scherrer´s formula[165,166].

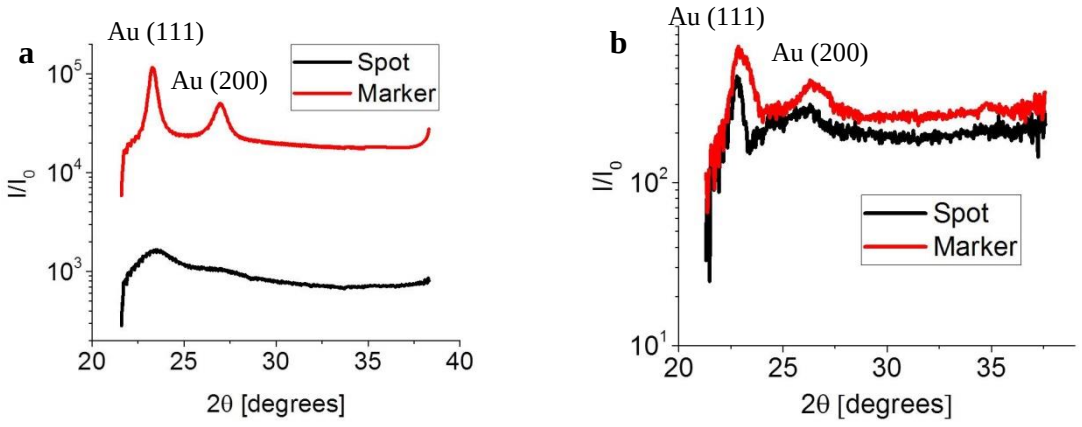

Figure 87: GIWAXS diffractograms. (a) Diffractogram from the 50% ML 1AUSL1 sample for the spot (black) and Au marker (red). (b) Diffractogram from the 10% ML 9AUSL1 sample for the Au_9 spot (black) and Au marker (red).

Figure 87 shows diffraction pattern from the spot and marker for both samples. The areas which were used as background for subtraction were chosen according to the corresponding areas on the XRF plots

taken simultaneously with the scattering measurements. On all this data background is already subtracted and this explains why there is not Si peak or the one from the capping layer visible. The WAXS pattern for 1AUSL1 sample clearly shows diffraction peaks at positions 2θ = 23.3° and 27.0° for the marker. They correspond to Au (111) and (200) lattice planes. The peak belonging to the 1AUSL1 spot is much wider than the one from the marker. This is an expected behaviour of a small structure. In the 9AUSL1 sample case in Figure 87**b** two peaks are also observed on the similar positions. A very sharp peak of 9AUSL1 cluster spot which looks alike the marker one can be explained by a small amount of material with a comparable thickness with the marker. This could happen that on one of the edges perpendicular to the markers the mask wafer shifted and there was a small streak of Au deposited. To quantify the data from GIWAXS measurements particle/crystalline size has been calculated by using Debye-Scherrer formula by[166,167]:

$$\text{Crystalline size} = \frac{0.9\lambda}{B\cos\theta}$$

Equation 23

where $B=\sqrt{(w_{sample}^2 - w_{reference}^2)}$, w_{sample} is the full width at half maximum (FWHM) of object peak (111) and $w_{reference}$ is FWHM from the calibrant measured in same experimental conditions (we used LaB_6). The crystal size for the cluster formed from 1AUSL1 deposition results to 3 nm, the one for 9AUSL1 is 10 nm and for the marker is about 8.5 nm. This estimation proves that the crystalline size cannot belong to 9AUSL1 cluster. In addition, if 50% ML gives such a weak signal in comparison to the marker in Figure 87**b** no significant peak can be expected for only 10% ML.

5.4. Investigation of bare Si/SiO_2 substrate

The description below is also provided in the supplimentay information[132].

Si wafer was cleaned according to the usual procedure, described in the Materials and Methods. Data obtained for the bare substrate is in the Figure 88 and Figure 89. It was investigated using GIWAXS and XPS. In the raw data in Figure 88 spots from SiO_2 (Hexagonal lattice, a=b=0.4912 nm, c=0.5404 nm, α=β=90°, γ=120°) are clearly visible, revealing single crystalline structure. Signals on the positions [002] (2θ=20.3146°) and [022] (2θ=33.131°) are pronounced. In the Figure 89 (calibrated data) Si 2p and SiO_2 2p peaks are visible which proves that the deposition was made on the oxide layer of the substrate.

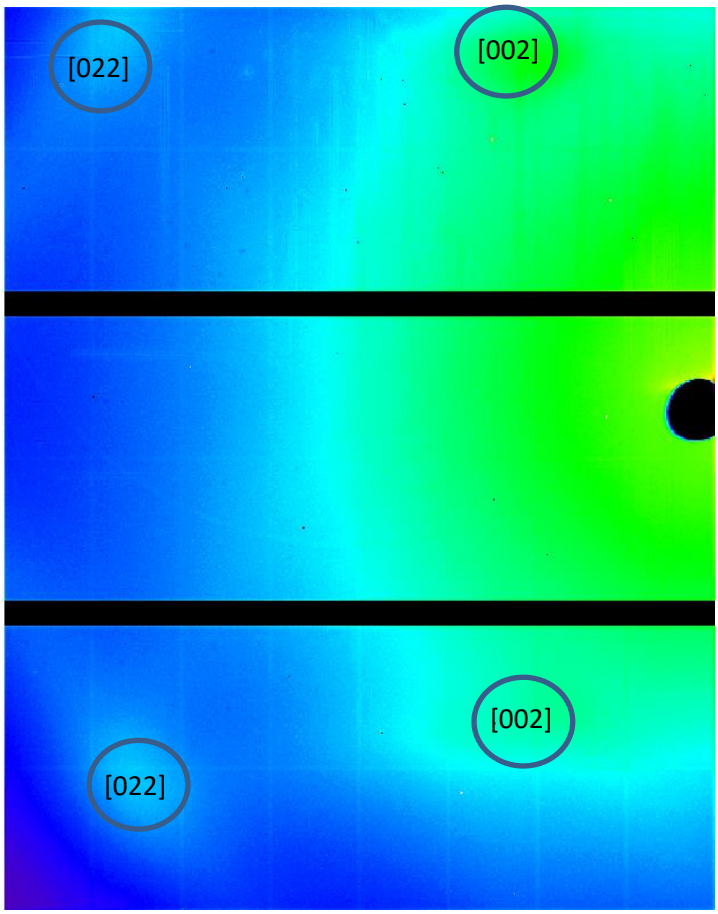

Figure 88: GIWAXS detector image of the bare Si/SiO_2 substrate.

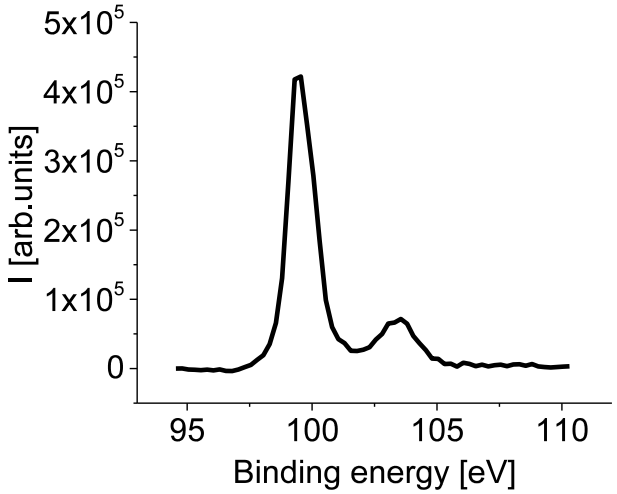

Figure 89: XPS spectra for bare Si/SiO_2 substrate of the Si 2p and SiO_2 2p peaks.

5.5. XRR analysis of bimetallic deposition using GenX and Fewlay

X-ray specular reflectivity is a standard method to characterise the average density, layer thickness and interface roughness of a layer system with a sub-nanometer resolution[168]. However, surfaces with big roughness, varying thickness or small scattering volume can be hard to investigate. Therefore, we used this method only in the analysis of thin layers with sufficient thickness 5 – 10 nm, homogeneously distributed throughout the whole surface. There exist a good number of literature where this method is explained in detail[119,168,169].

Analysis of the final thickness using XRR was done for bimetallic samples (Sections 2.1.2.1 and 3.1). *Ex situ* measurements of sample thickness done with XRR can be used to validate the estimated deposition rate. In Figure 90 are presented XRR curves and fitted curves for the full range of samples, produced by GenX[170]. This data provides information on the resulting effective thickness.

Calculated data from both analysis tools GenX and Fewlay[171] (only numerical values provided here) is in the Table 16. Except for the alternate deposited samples AuonAg and AuonAgA, resulting thickness is in the expected range and in agreement between each other. The problem with finding the perfect fit for them could be caused by an asymmetry of the deposited layers.

a

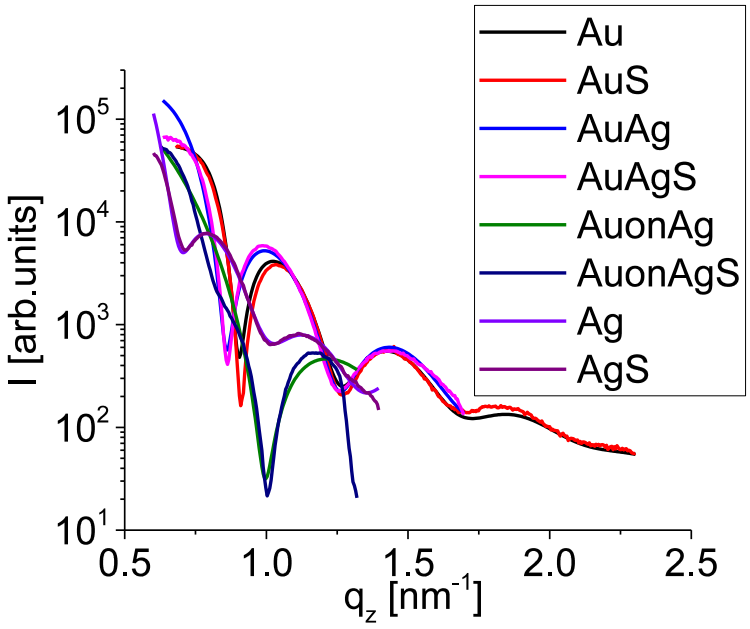

b

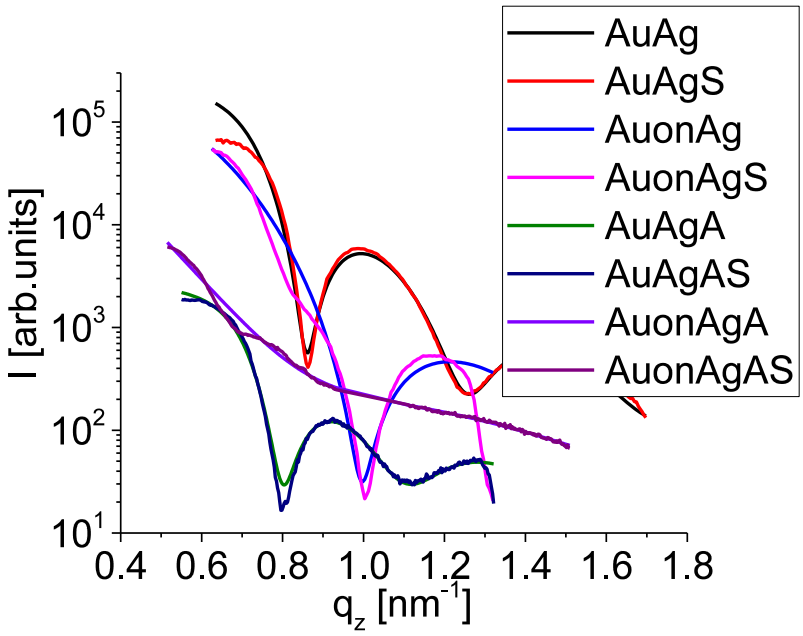

Figure 90: XRR data with fitted curves obtained from GenX. S in the ending stands for 'simulated'. (a) – samples prepared in the room temperature. (b) – bimetallic samples prepared in the room temperature conditions and while heating.

Sample	Thickness (GenX) [Å]	Thickness (Fewlay) [Å]
Au	106.2457	107.846
AuAg	43.6(Ag) +58.2(Au)	54.3548(Ag) +49.5207(Au)
AuonAg	23.259(Au) +42.879(Ag)	71.38(Au) +66.7228(Ag)
Ag	98.0534(Ag) +22.55(Ag_2O)	109.946 (Ag) +24.7137(Ag_2O)
AuAgA	39.11727(Ag) +79.9982(Au)	50.1839 (Ag) +65.7812 (Au)
AuonAgA	50.04456(Ag) +10.0016(Au)	–

Table 16: Thickness values obtained, using GenX and Fewlay.

5.6. Off-detector cuts made for bimetallic samples

Figure 91 shows vertical cuts, which can be used to estimate the height of the deposited nanoclusters/nanolayers. The smaller the distance between the peak minima/maxima, the bigger the structure in the real space.

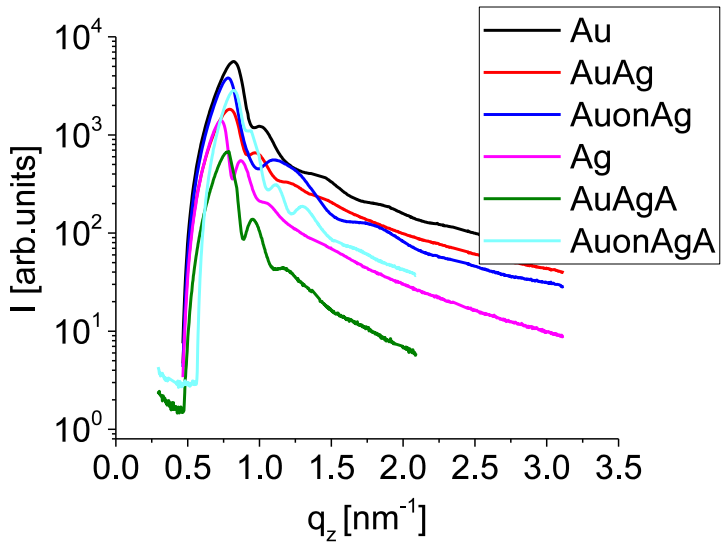

Figure 91: Off-detector cuts made when effective thickness was 10 nm.

5.7. XRR analysis of ultrasmall size-selected samples using GenX

XRR analysis was done for ultrasmall size-selected samples to confirm the thickness of the capping layer to be around 5 nm. The experimental data and the fits obtained using GenX for 9AUSL2 and 11AUSL1 are provided in Figure 92. The capping layer (Al) for 11AUSL1 is 5.75 nm and for 9AUSL2 5.27 nm. On one hand this thickness is low enough to be sensitive for GISAXS analysis of structures underneath, but it also limitates the choice of data for subtraction (each sample should have its own data for subtraction and one cannot be used for all).

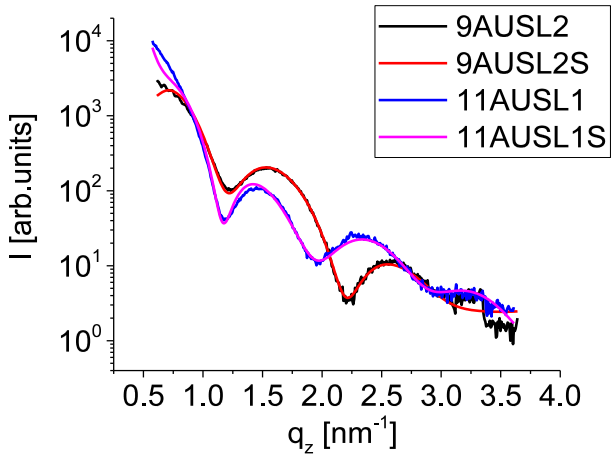

Figure 92: XRR experimental curves and fits for 9AUSL2 and 11AUSL1. S stands for 'simulated'(fits).

5.8. Experimental data of ultrasmall size-selected clusters with fits

Figure 93 contains Yoneda (horizontal) cuts with fits made, using DPDAK for 5AUSL1, 7AUSL1, 9AUSL2 and 11 AUSL1. From these fits q_{ymax} positions were estimated to be used for evaluate interparticle distances and radii.

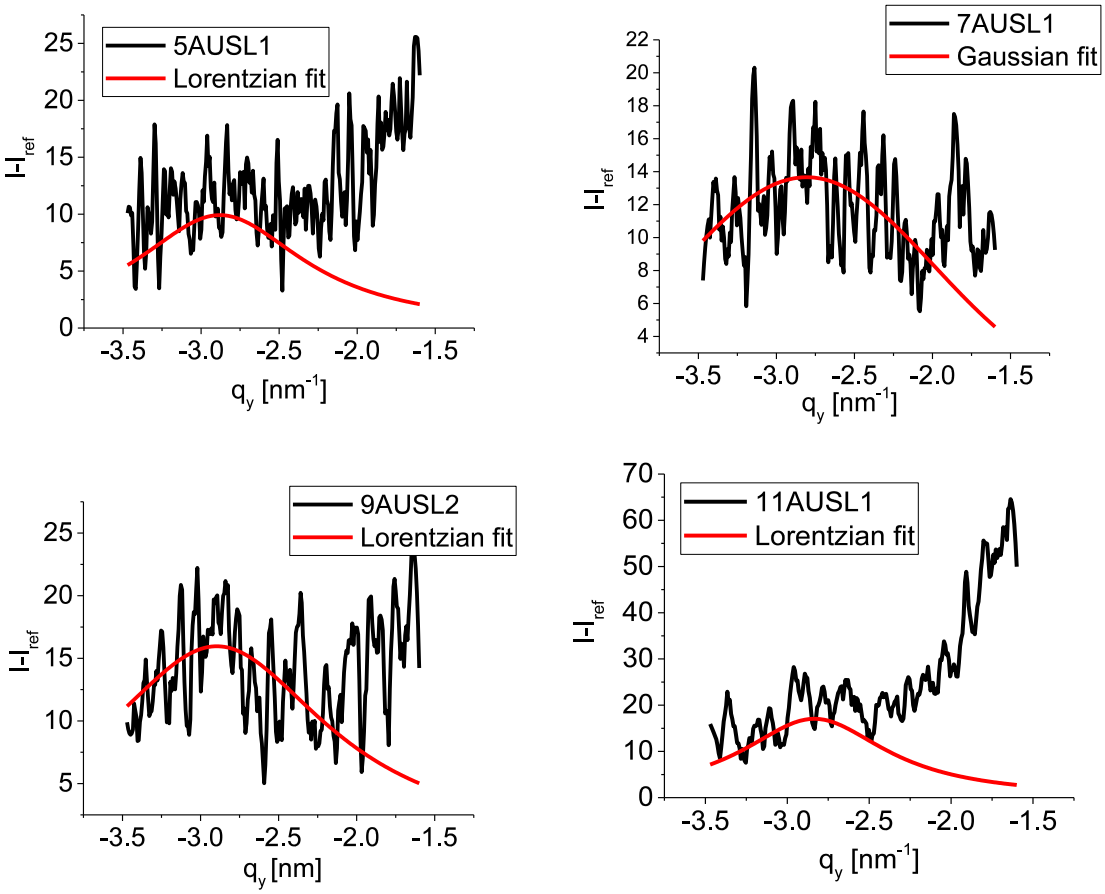

Figure 93: Yoneda cuts and fits made for samples with ultrasmall size-selected clusters.

5.9. Example of the input file for IsGISAXS simulation of AuAgA

```
########################################

#   GISAXS SIMULATIONS : INPUT PARAMETERS

########################################


# Base filename

AuAgannealed_hemisphere_10nm_0001

############################ Framework and beam parameters ############################################

# Framework   Diffuse,  Multilayer, Number of index slices, Polarization

 DWBA     DA        1       7                  ss

# Beam Wavelenght  :  Lambda(nm).  Wl_distribution.  Sigma_Wl/Wl.  Wl_min(nm). Wl_max(nm). nWl.  xWl

                0.0953       none            0.2         0.08        0.12     10    -2

# Beam Alpha_i     : Alpha_i(deg). Ai_distribution. Sigma_Ai(deg). Ai_min(deg). Ai_max(deg). nAi. xAi

                0.42          none         0.05        0.05        0.7    10   -2

# Beam 2Theta_i    :  2Theta_i(deg). Ti_distribution. Sigma_Ti(deg). Ti_min(deg). Ti_max(deg). nTi. XTi

                  0.          none          0.5          -0.5          0.5      10   -2

# Substrate :  n-delta_S.     n-beta_S.   Layer thickness(nm). n-delta_L.   n-beta_L.  RMS roughness(nm)

              2.78138236E-06  2.44526444E-08                1          3.22062056E-06     2.33290436E-08 1.0000E+00

# Particle : n-delta_I.     n-beta_I.     Depth(nm).  n-delta_SH.   n-beta_SH

         1.42334529E-05  1.2788729E-06       1      3.729E-05    3.68100000E-06

################################## Grid parameters ########################################################
```

Ewald mode

T

Output angle (deg) : Two theta min-max, Alphaf min-max, n(1), n(2)

-0.916 0.975 0.00 0.95 800 700

Output q(nm-1) : Qx min-max, Qy min-max, Qz min-max, n(1), n(2), n(3)

-1. 1. -3.7 3.7 1.13 5.18 300 300 1

################################## Particle parameters ##

Number of different particle types

2

Particle type, Probability

aniso_hemi_spheroid 1

cylinder 0

Geometrical parameters : Base angle (deg), Height ratio, Flattening, FS-radii/R

54.7356 0.000001 1.12163E+00 0.8 0.8

54.7356 0.000001 1.12163E+00 0.8 0.8

Shell thicknesses (nm) : dR, dH, dW

0. 0. 0.

0. 0. 0.

H_uncoupled, W_uncoupled

T T

T T

Size of particle : Radius(nm), R_distribution, SigmaR/R, Rmin(nm), Rmax(nm), nR, xR

20.19 none 1.2 0.1 1 50 -1

0.2 none 1.2 50 250 50 -1

Height aspect ratio : Height/R, H_distribution, SigmaH/H, Hmin/R, Hmax/R, nH, xH, rho_H

1 none 0.5 0.1 1 1 2.5 9.53741E-01

1 none 0.05 1 1 20 2.5 9.53741E-01

Width aspect ratio : Width/R, W_distribution, SigmaW/W, Wmin/R, Wmax/R, nW, xW, rho_W

1 none 0.5 1.95 2.05 50 -2. 0.953

1 none 0.5 1 200 50 -2. 0.953

Orientation of particle : Zeta(deg), Z_distribution, SigmaZ(deg), Zmin(deg), Zmax(deg), nZ, xZ

0 none 20. 0 120 30 2

0 none 20. 0 120 30 2

########## Lattice parameters ##########

Particle distribution : type

1ddl

Interference function : Peak position D(nm), w(nm), Statistics, Eta_Voigt, Size-Distance coupling, Cut-off

44.56 11.14 gau 0.5 0 300

Pair correlation function : Density(nm-2), D1(nm), Hard core coverage, CxR

0.007 25 0.3 1.

Lattice parameters : L(1)(nm), L(2)(nm), Angle(deg, Xi_fixed

20 20 60. F

Xi(deg), Xi_distribution, SigmaXi(deg), Ximin(deg), Ximax(deg), nXi, xXi

0 none 20 0. 240. 3 -2

Domain sizes DL(nm), DL_distribution, SigmaDL/DL, DLmin(nm), DLmax(nm), nDL, XDL

50 50 none 0.2 0.2 200 200 20000 20000 10 10 -2 -2

Imperfect lattice : Rod description, Rod shape,

rec_prod_pa cau cau

Correlation lenghts(nm), Rod orientation(deg)

20 20 0 90

Paracrystal : Probability description

prod_pa

Disorder factors w(nm), DL-statistical distribution and rod orientation (deg)

100 100 100 100

cau cau cau cau

0 90 0 90

Pattern : Regular pattern content, Number of particles per pattern

F 2

Positions xp/L, Debye-Waller factors B11/L1 B22/L1 B12/L1

0. 0. 0. 0. 0.

0.869 0.5 0.05 0.05 0.

5.10. Simulation output example (bimetallic clusters)

A series of simulations was created, using IsGISAXS. An example of AuAg (10 nm effective thickness) to illustrate shape influence is provided in Figure 94. For all of them the same conditions were used, radius was considered to be 13.51 nm and interparticle distance 24.44 nm. Figure 94**a** is the final shape the closest to the experiment-ellipsoid with H/R =1.3 and W/R = 0.35. Others are provided to show the shape impact while parameters H/R = W/R = 1. As can be seen, with these conditions the cylinder output (**d**) is the same as ellipsoid (**e**), but cylinder does not allow width variation.

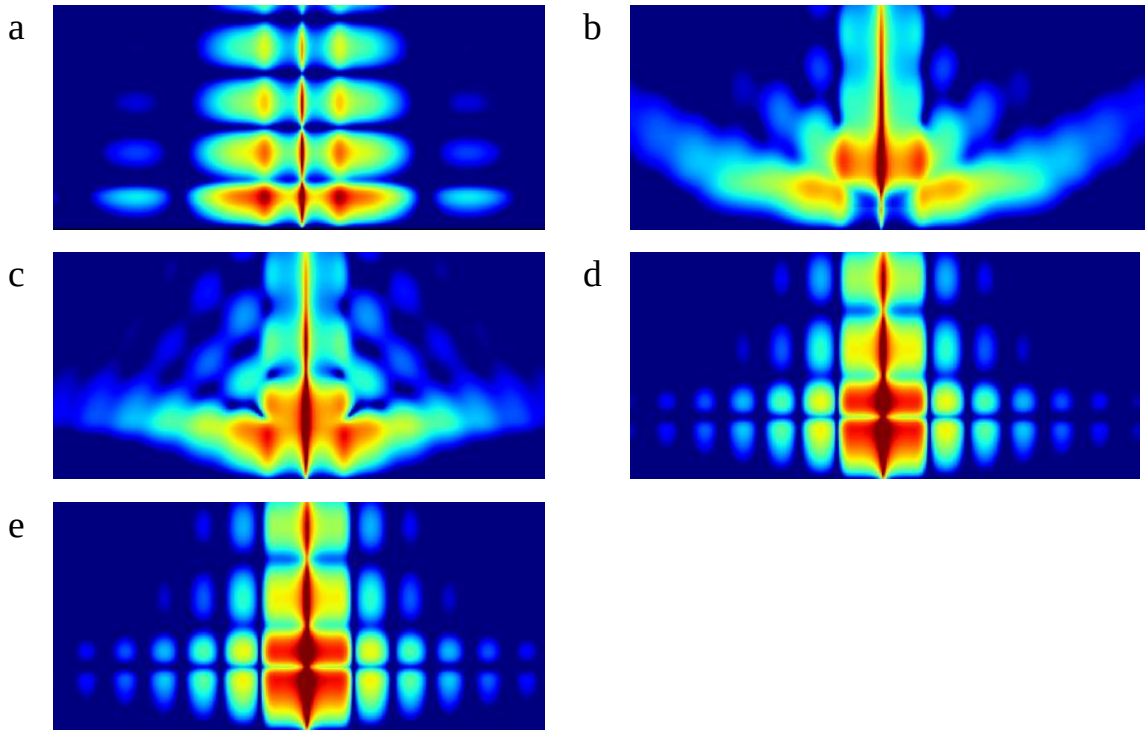

Figure 94: Examples of simulations, using IsGISAXS. (a) –final choice (ellipsoid), (b) – cone, (c)-hemisphere, (d) – cylinder, (e) – ellipsoid.

5.11. PCA example on 7AUSL1.

The same PCA analysis was applied for 7AUSL1 data to demonstrate that it also works for this example and can separate spot position.

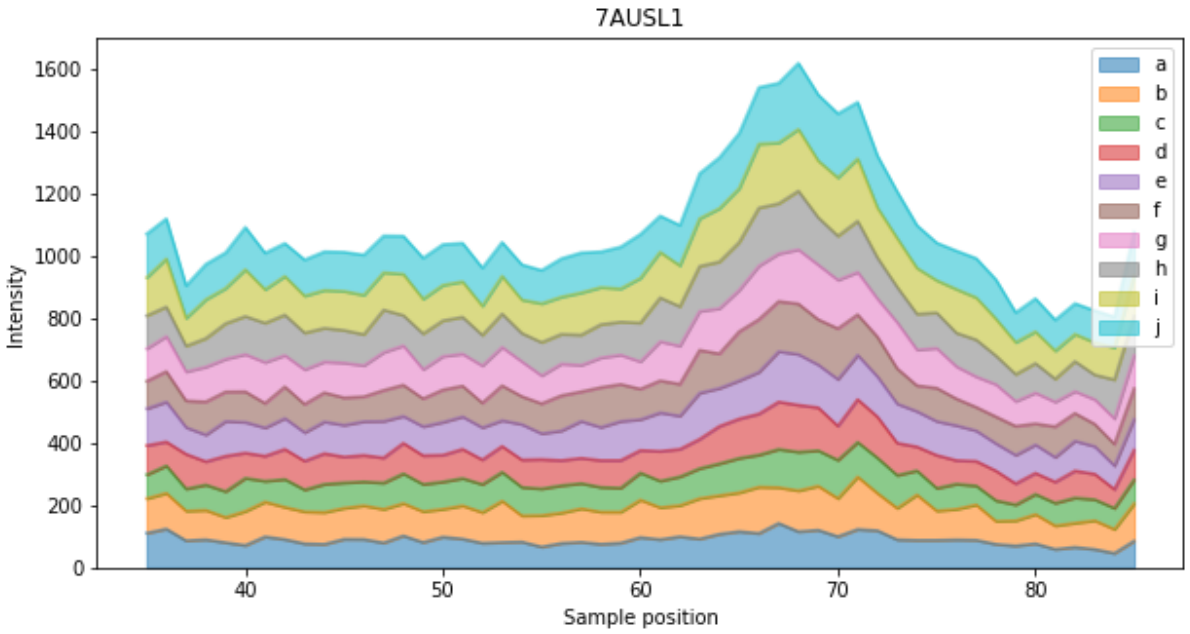

Figure 95: Area graph of features depending on the sample position

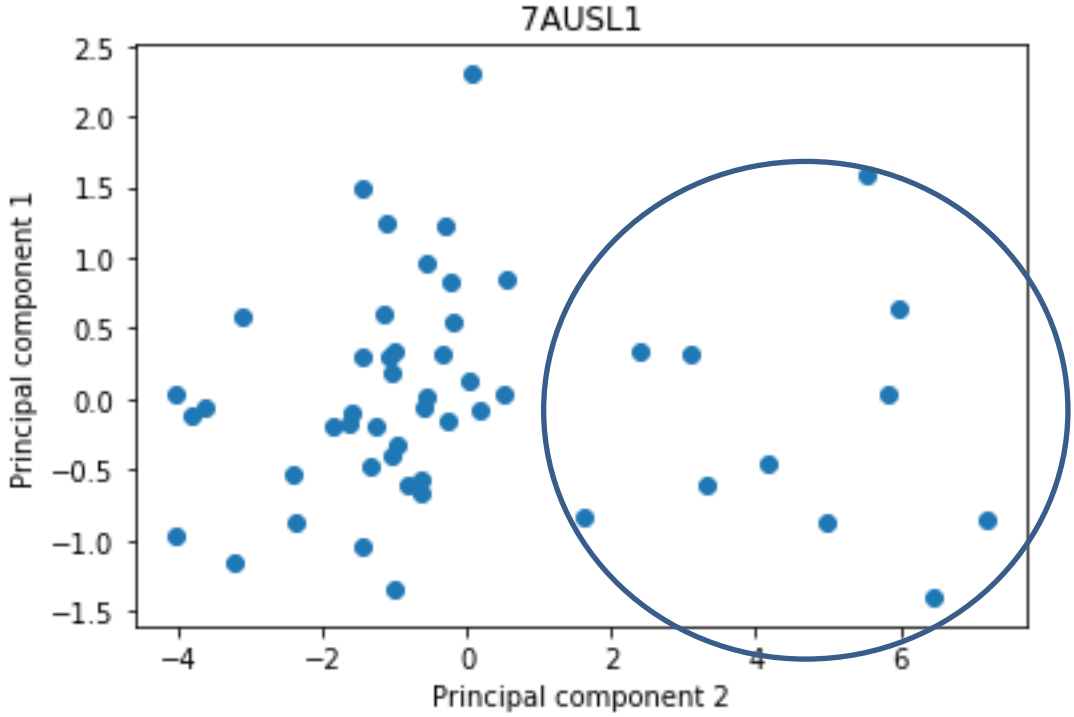

Figure 96: Dependency graph of two principal components.

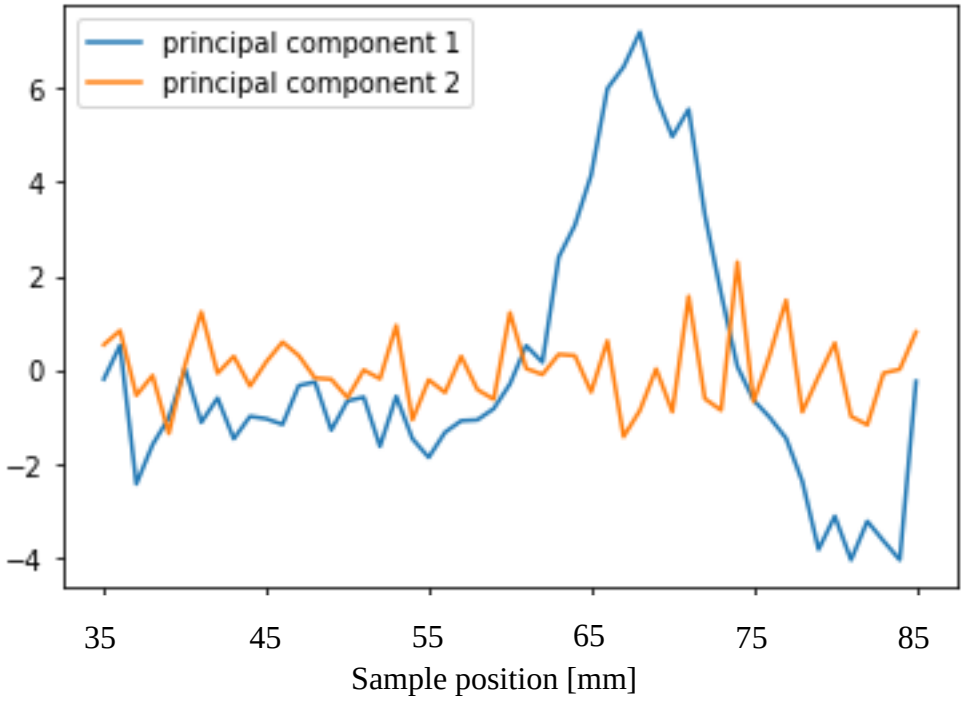

Figure 97: Principal components depending on the sample position.

6. References

1. Alvarez, M. M. *et al.* Emerging Trends in Micro- and Nanoscale Technologies in Medicine: From Basic Discoveries to Translation. *ACS Nano* **11,** 5195–5214 (2017).

2. Rai, S. & Rai, A. Nanotechnology - The secret of fifth industrial revolution and the future of next generation. *Nusant. Biosci.* **7,** 61–66 (2015).

3. EC. Horizon 2020 - Work Programme 2018-2020 – 5.ii. Nanotechnologies, Advanced Materials, Biotechnology and Advanced Manufacturing and Processing. (2017).

4. de Heer, W. a. The physics of simple metal clusters: experimental aspects and simple models. *Rev. Mod. Phys.* **65,** 611–676 (1993).

5. Häkkinen, H., Moseler, M. & Landman, U. Bonding in Cu, Ag, and Au clusters: Relativistic effects, trends, and surprises. *Phys. Rev. Lett.* **89,** 33401 (2002).

6. Fernández, E., Soler, J., Garzón, I. & Balbás, L. Trends in the structure and bonding of noble metal clusters. *Phys. Rev. B* **70,** 1–14 (2004).

7. Jin, R., Zeng, C., Zhou, M. & Chen, Y. Atomically Precise Colloidal Metal Nanoclusters and Nanoparticles: Fundamentals and Opportunities. *Chem. Rev.* **116,** 10346–10413 (2016).

8. Chernousova, S. & Epple, M. Silver as Antibacterial Agent: Ion, Nanoparticle, and Metal. *Angew. Chemie Int. Ed.* **52,** 1636–1653 (2013).

9. Wei, L. *et al.* Silver nanoparticles: synthesis, properties, and therapeutic applications. *Drug Discov. Today* **20,** 595–601 (2015).

10. Zhang, X. F., Liu, Z. G., Shen, W. & Gurunathan, S. Silver nanoparticles: Synthesis, characterization, properties, applications, and therapeutic approaches. *Int. J. Mol. Sci.* **17,** (2016).

11. Matulionyte, M., Dapkute, D., Budenaite, L., Jarockyte, G. & Rotomskis, R. Photoluminescent Gold Nanoclusters in Cancer Cells: Cellular Uptake, Toxicity, and Generation of Reactive Oxygen Species. *Int. J. Mol. Sci.* **18,** 378 (2017).

12. Zhang, X.-D. *et al.* Ultrasmall glutathione-protected gold nanoclusters as next generation radiotherapy sensitizers with high tumor uptake and high renal clearance. *Sci. Rep.* **5,** 8669 (2015).

13. Yadav, B. D. & Kumar, V. Gd@ Au15: A magic magnetic gold cluster for cancer therapy and bioimaging. *Appl. Phys. Lett.* **97,** 2008–2011 (2010).

14. Sun, J. & Jin, Y. Fluorescent Au nanoclusters: recent progress and sensing applications. *J. Mater. Chem. C* **2,** 8000–8011 (2014).

15. Novikov, S. M. *et al.* Highly Stable Monocrystalline Silver Clusters for Plasmonic Applications. *Langmuir* **33,** 6062–6070 (2017).

16. Guisbiers, G. *et al.* Electrum, the gold-silver alloy, from the bulk scale to the nanoscale: Synthesis, properties, and segregation rules. *ACS Nano* **10,** 188–198 (2016).

17. Mazhar, T., Shrivastava, V. & Tomar, R. S. Green Synthesis of Bimetallic Nanoparticles and its Applications : A Review. **9,** 102–110 (2017).

18. Faupel, F., Zaporojtchenko, V., Strunskus, T. & Elbahri, M. Metal-Polymer Nanocomposites for Functional Applications. *Adv. Eng. Mater.* **12,** 1177–1190 (2010).

19. Haruta, M. Size- and support-dependency in the catalysis of gold. *Catal. Today* **36,** 153–166 (1997).

20. Heiz, U., Sanchez, A., Abbet, S. & Schneider, W.-D. Catalytic Oxidation of Carbon Monoxide on Monodispersed Platinum Clusters:~ Each Atom Counts. *J. Am. Chem. Soc.* **121,** 3214–3217 (1999).

21. Zheng, J., Zhang, C. & Dickson, R. M. Highly fluorescent, water-soluble, size-tunable gold quantum

dots. *Phys. Rev. Lett.* **93,** 5–8 (2004).

22. Samanta, A., Dhar, B. B. & Devi, R. N. Ultrasmall Gold Cluster Arrays Encapsulated in Silica Nanospheres: Applications in Fluorescence Imaging and Catalysis. *J. Phys. Chem. C* **116,** 1748–1754 (2012).

23. Dollinger, A. *et al.* Size-selected gold clusters on porous titania as the most 'gold-efficient' heterogeneous catalysts. *Phys. Chem. Chem. Phys.* **16,** 11017 (2014).

24. Wu, Y. Y., Mashayekhi, N. A. & Kung, H. H. Au–metal oxide support interface as catalytic active sites. *Catal. Sci. Technol.* **3,** 2881 (2013).

25. Herzing, A. A., Kiely, C. J., Carley, A. F., Landon, P. & Hutchings, G. J. Identification of Active Gold Nanoclusters on Iron Oxide Supports for CO Oxidation. *Science (80-.).* **321,** 1331–1335 (2008).

26. Binns, C. Nanoclusters deposited on surfaces. *Surf. Sci. Rep.* **44,** 1–49 (2001).

27. Qian, M. *et al.* Cluster-Assembled Materials: Toward Nanomaterials with Precise Control over Properties. *ACS Nano* **4,** 235–240 (2010).

28. Pyykkö, P. Theoretical Chemistry of Gold. *Angew. Chemie Int. Ed.* **43,** 4412–4456 (2004).

29. Schwartzkopf, M. & Roth, S. Investigating Polymer–Metal Interfaces by Grazing Incidence Small-Angle X-Ray Scattering from Gradients to Real-Time Studies. *Nanomaterials* **6,** 239 (2016).

30. Santoro, G. *et al.* Silver substrates for surface enhanced Raman scattering: Correlation between nanostructure and Raman scattering enhancement. *Appl. Phys. Lett.* **104,** (2014).

31. Schwartzkopf, M. *et al.* From atoms to layers: in situ gold cluster growth kinetics during sputter deposition. *Nanoscale* **5,** 5053 (2013).

32. Schwartzkopf, M. *et al.* Real-Time Monitoring of Morphology and Optical Properties during Sputter Deposition for Tailoring Metal–Polymer Interfaces. *ACS Appl. Mater. Interfaces* **7,** 13547–13556 (2015).

33. Martins, M. & Wurth, W. Magnetic properties of supported metal atoms and clusters. *J. Phys. Condens. Matter* **28,** 503002 (2016).

34. Sanchez, A. *et al.* When Gold Is Not Noble: Nanoscale Gold Catalysts. *J. Phys. Chem. A* **103,** 9573–9578 (1999).

35. Müller-Buschbaum, P. A Basic Introduction to Grazing Incidence Small-Angle X-Ray Scattering. in *Lect. Notes Phys. 776* 61–89 (2009). doi:10.1007/978-3-540-95968-7_3

36. Santoro, G. & Yu, S. Grazing Incidence Small Angle X-Ray Scattering as a Tool for In- Situ Time-Resolved Studies. in *X-ray Scattering* 1–34 (InTech, 2017). doi:10.5772/64877

37. Milton, O. *The materials science of thin films*. (1992).

38. Jensen, P. Growth of nanostructures by cluster deposition : a review. **71,** 1695–1735 (1999).

39. G.V., F. *Synchrotron radiation. Methods for substance structure investigation (in Russian: 'Sinkhrotronnoe izluchenie. Metody issledovaniya struktury veschestv').* (Fizmatlit, 2007).

40. Feigin, L. A. & Svergun, D. I. *Structure Analysis by Small-Angle X-Ray and Neutron Scattering*. (Springer US, 1987). doi:10.1007/978-1-4757-6624-0

41. P., F. R. There's (still) plenty of room at the bottom. *Caltech Engineering and Science* **23:5,** 22–36 (1960).

42. Palmer, R. E. Welcome to Clusterworld. *New Sci.* 38–41 (1997).

43. Schmid, G. *et al.* Current and future applications of nanoclusters. *Chem Soc Rev* **28,** 179–185 (1999).

44. Kurashige, W., Niihori, Y., Sharma, S. & Negishi, Y. Precise synthesis, functionalization and application of thiolate-protected gold clusters. *Coord. Chem. Rev.* **320–321,** 238–250 (2016).

45. Qu, X. *et al.* Fluorescent gold nanoclusters: Synthesis and recent biological application. *J. Nanomater.* **2015,** (2015).

46. Schmid, G. & Corain, B. Nanoparticulated Gold: Syntheses, Structures, Electronics, and Reactivities. *Eur. J. Inorg. Chem.* **2003,** 3081–3098 (2003).

47. Faraday, M. The Bakerian Lecture: Experimental Relations of Gold (and Other Metals) to Light. *Philos. Trans. R. Soc. London* **147,** 145–181 (1857).

48. Herzog, R. O. Grundriß der Kolloidchemie. Von Dr. Wo. Ostwald. Verlag von Th. Steinkopff. Dresden 1909. 525 Seiten. Preis brosch. 12 Mk., geb. 13,50 Mk. *J. Am. Chem. Soc.* **15,** 948 (1909).

49. Castro, T., Reifenberger, R., Choi, E. & Andres, R. P. Size-dependent melting temperature of individual nanometer-sized metallic clusters. *Phys. Rev. B* **42,** 8548–8556 (1990).

50. Schwerdtfeger, P. Relativistic effects in properties of gold. *Heteroat. Chem.* **13,** 578–584 (2002).

51. Schwerdtfeger, P. Gold Goes Nano—From Small Clusters to Low-Dimensional Assemblies. *Angew. Chemie Int. Ed.* **42,** 1892–1895 (2003).

52. Hornyak, G. *et al.* Gold clusters and colloids in alumina nanotubes. *Chem. - A Eur. J.* **3,** 1951–1956 (1997).

53. Syafiuddin, A. *et al.* A Review of Silver Nanoparticles: Research Trends, Global Consumption, Synthesis, Properties, and Future Challenges. *J. Chinese Chem. Soc.* **64,** 732–756 (2017).

54. Wang, D. & Li, Y. Bimetallic Nanocrystals: Liquid-Phase Synthesis and Catalytic Applications. *Adv. Mater.* **23,** 1044–1060 (2011).

55. Ferrando, R., Jellinek, J. & Johnston, R. L. Nanoalloys: From Theory to Applications of Alloy Clusters and Nanoparticles. *Chem. Rev.* **108,** 845–910 (2008).

56. Chen, J., Javaheri, H., Al-Chikh Sulaiman, B. & Dahman, Y. Synthesis, characterization and applications of nanoparticles. in *Fabrication and Self-Assembly of Nanobiomaterials* 1–27 (Elsevier, 2016). doi:10.1016/B978-0-323-41533-0.00001-5

57. Palagin, D. & Doye, J. P. K. DNA-stabilized Ag–Au bimetallic clusters: the effects of alloying and embedding on optical properties. *Phys. Chem. Chem. Phys.* **18,** 22311–22322 (2016).

58. Lu, J. *et al.* Toward atomically-precise synthesis of supported bimetallic nanoparticles using atomic layer deposition. *Nat. Commun.* **5,** 1–9 (2014).

59. Intartaglia, R. *et al.* Laser synthesis of ligand-free bimetallic nanoparticles for plasmonic applications. *Phys. Chem. Chem. Phys.* **15,** 3075–3082 (2013).

60. Liao, T.-W. *et al.* Unravelling the nucleation mechanism of bimetallic nanoparticles with composition-tunable core–shell arrangement. *Nanoscale* **10,** 6684–6694 (2018).

61. Wei, J. *et al.* Optically Active Ultrafine Au–Ag Alloy Nanoparticles Used for Colorimetric Chiral Recognition and Circular Dichroism Sensing of Enantiomers. *Anal. Chem.* **89,** 9781–9787 (2017).

62. Vahl, A. *et al.* Single target sputter deposition of alloy nanoparticles with adjustable composition via a gas aggregation cluster source. *Nanotechnology* **28,** 175703 (2017).

63. Liu, J., Chen, C., Yang, G., Chen, Y. & Yang, C. F. Effect of the Fabrication Parameters of the Nanosphere Lithography Method on the Properties of the Deposited Au-Ag Nanoparticle Arrays. *Materials (Basel).* **10,** (2017).

64. Dong, J. *et al.* Preparation of Ag/Au bimetallic nanostructures and their application in surface-enhanced fluorescence. *Luminescence* **30,** 1090–1093 (2015).

65. Yao, M. *et al.* Performance Improvement of Polymer Solar Cells by Surface-Energy-Induced Dual Plasmon Resonance. *ACS Appl. Mater. Interfaces* **8,** 6183–6189 (2016).

66. Nishijima, Y. & Akiyama, S. Unusual optical properties of the Au/Ag alloy at the matching mole fraction. *Opt. Mater. Express* **2,** 1226 (2012).

67. Hong, L. *et al.* Atomic structures and electronic properties of small Au-Ag binary clusters: Effects of size and composition. *Comput. Theor. Chem.* **993,** 36–44 (2012).

68. Smelova, E. M., Klavsyuk, A. L., Tsysar', K. M. & Saletskii, A. M. Investigation of the mechanical and electronic properties of Ag-Au and Co-Au nanocontacts by the method of first-principle molecular dynamics. *Moscow Univ. Phys. Bull.* **68,** 92–95 (2013).

69. Fan, F. *et al.* Epitaxial Growth of Heterogeneous Metal Nanocrystals: From Gold Nano-octahedra to Palladium and Silver Nanocubes. *J. Am. Chem. Soc.* **130,** 6949–6951 (2008).

70. Belić, D., Chantry, R. L., Li, Z. Y. & Brown, S. A. Ag-Au nanoclusters: Structure and phase segregation. *Appl. Phys. Lett.* **99,** (2011).

71. Li, Z. Y., Yuan, J., Chen, Y., Palmer, R. E. & Wilcoxon, J. P. Direct imaging of core-shell structure in silver-gold bimetallic nanoparticles. *Appl. Phys. Lett.* **87,** 1–3 (2005).

72. Tsai, C.-H., Chen, S.-Y., Song, J.-M., Haruta, M. & Kurata, H. Effect of Ag Templates on the Formation of Au-Ag Hollow/Core-Shell Nanostructures. *Nanoscale Res. Lett.* **10,** 438 (2015).

73. Bai, T. *et al.* Controllable Preparation of Core–Shell Au–Ag Nanoshuttles with Improved Refractive Index Sensitivity and SERS Activity. *ACS Appl. Mater. Interfaces* **6,** 3331–3340 (2014).

74. Tan, S. F. *et al.* Real-Time Imaging of the Formation of Au-Ag Core-Shell Nanoparticles. *J. Am. Chem. Soc.* **138,** 5190–5193 (2016).

75. Song, Y. & Chen, S. Janus nanoparticles: Preparation, characterization, and applications. *Chem. - An Asian J.* **9,** 418–430 (2014).

76. Hubenthal, F., Borg, N. & Träger, F. Optical properties and ultrafast electron dynamics in gold–silver alloy and core–shell nanoparticles. *Appl. Phys. B* **93,** 39–45 (2008).

77. Verma, S. *et al.* Surface plasmon resonances of Ag-Au alloy nanoparticle films grown by sequential pulsed laser deposition at different compositions and temperatures. *J. Appl. Phys.* **117,** (2015).

78. Döhrmann, R. *et al.* A new highly automated sputter equipment for in situ investigation of deposition processes with synchrotron radiation. *Rev. Sci. Instrum.* **84,** (2013).

79. Hvolbæk, B. *et al.* Catalytic activity of Au nanoparticles. *Nano Today* **2,** 14–18 (2007).

80. Schooss, D., Weis, P., Hampe, O. & Kappes, M. M. Determining the size-dependent structure of ligand-free gold-cluster ions. *Philos Trans A Math Phys Eng Sci* **368,** 1211–1243 (2010).

81. Niu, Y. *et al.* Reduced sintering of mass-selected Au clusters on SiO 2 by alloying with Ti: an aberration-corrected STEM and computational study. *Nanoscale* **10,** 2363–2370 (2018).

82. Amendola, V., Pilot, R., Frasconi, M., Maragò, O. M. & Iatì, A. M. Surface plasmon resonance in gold nanoparticles: A review. *J. Phys. Condens. Matter* **29,** 203002 (2017).

83. Coquet, R., Howard, K. L. & Willock, D. J. Theory and simulation in heterogeneous gold catalysis. *Chem. Soc. Rev.* **37,** 2046 (2008).

84. Li, M., Yang, D.-P., Wang, X., Lu, J. & Cui, D. Mixed protein-templated luminescent metal clusters (Au and Pt) for H2O2 sensing. *Nanoscale Res. Lett.* **8,** 182 (2013).

85. Errico, V. *et al.* Chromium inhibition and size-selected Au nanocluster catalysis for the solution growth of low-density ZnO nanowires. *Sci. Rep.* **5,** 12336 (2015).

86. Bosch-Navarro, C. *et al.* Covalently Binding Atomically Designed Au 9~{C}lusters to Chemically

Modified Graphene. *Angew. Chemie Int. Ed.* **54,** 9560–9563 (2015).

87. Al Qahtani, H. S. *et al.* Atomically resolved structure of ligand-protected Au 9 clusters on TiO 2 nanosheets using aberration-corrected STEM. *J. Chem. Phys.* **144,** 114703 (2016).

88. Kunz, S. *et al.* Size-selected clusters as heterogeneous model catalysts under applied reaction conditions. *Phys. Chem. Chem. Phys.* **12,** 10288 (2010).

89. Yoon, B., Häkkinen, H. & Landman, U. Interaction of O2 with Gold Clusters: Molecular and Dissociative Adsorption. *J. Phys. Chem. A* **107,** 4066–4071 (2003).

90. Zhang, S.-S. *et al.* Diphosphine-protected ultrasmall gold nanoclusters: opened icosahedral Au 13 and heart-shaped Au 8 clusters. *Chem. Sci.* **00,** 1–8 (2018).

91. Shichibu, Y., Zhang, M., Kamei, Y. & Konishi, K. [Au7]3+: A missing link in the four-electron gold cluster family. *J. Am. Chem. Soc.* **136,** 12892–12895 (2014).

92. Wen, F., Englert, U., Gutrath, B. & Simon, U. Crystal Structure, Electrochemical and Optical Properties of [Au9(PPh3)8](NO3)3. *Eur. J. Inorg. Chem.* **2008,** 106–111 (2008).

93. Johnson, G. E. & Laskin, J. Understanding ligand effects in gold clusters using mass spectrometry. *Analyst* **141,** 3573–3589 (2016).

94. Andersson, G. G. *et al.* Phosphine-stabilised Au9 clusters interacting with titania and silica surfaces: The first evidence for the density of states signature of the support-immobilised cluster. *J. Chem. Phys.* **141,** 14702 (2014).

95. Lau, J. T. *et al.* Ultrahigh vacuum cluster deposition source for spectroscopy with synchrotron radiation. *Rev. Sci. Instrum.* **76,** 63902 (2005).

96. Pratontep, S. *et al.* Scaling relations for implantation of size-selected Au, Ag, and Si clusters into graphite. *Phys. Rev. Lett.* **90,** 055503 (2003).

97. von Issendorff, B. & Palmer, R. E. A new high transmission infinite range mass selector for cluster and nanoparticle beams. *Rev. Sci. Instrum.* **70,** 4497 (1999).

98. Glaser, L. *et al.* Magnetic properties of small size-selected Co and CoPt clusters on Ni. *Phys. Rev. B - Condens. Matter Mater. Phys.* **86,** 1–5 (2012).

99. Furche, F. *et al.* The structures of small gold cluster anions as determined by a combination of ion mobility measurements and density functional calculations. *J. Chem. Phys.* **117,** 6982–6990 (2002).

100. Jain, P. K. A DFT-based study of the low-energy electronic structures and properties of small gold clusters. *Struct. Chem.* **16,** 421–426 (2005).

101. Li, Z. *et al.* Experimental and DFT studies of gold nanoparticles supported on MgO(111) nano-sheets and their catalytic activity. *Phys Chem Chem Phys* **13,** 2582–2589 (2011).

102. Wu, X., Chen, S., Sun, Y. & Chen, Y. Geometrical structures of gold clusters on Gupta and Sutton-Chen potentials. *Comput. Theor. Chem.* **1002,** 43–48 (2012).

103. Xiao, L., Tollberg, B., Hu, X. & Wang, L. Structural study of gold clusters. *J. Chem. Phys.* **124,** (2006).

104. Woodham, A. P. & Fielicke, A. Gold Clusters in the Gas Phase. in *Structure and Bonding* 243–278 (2013). doi:10.1007/430_2013_136

105. Weis, P., Bierweiler, T., Vollmer, E. & Kappes, M. M. Au9+: Rapid isomerization reactions at 140 K. *J. Chem. Phys.* **117,** 9293–9297 (2002).

106. Liz-Marzán, L. M. Nanometals. *Mater. Today* **7,** 26–31 (2004).

107. Das, V. L. *et al.* Extracellular synthesis of silver nanoparticles by the Bacillus strain CS 11 isolated from industrialized area. *3 Biotech* **4,** 121–126 (2014).

108. Westwood, W. D. Sputter Deposition Processes. *MRS Bull.* **13,** 46–51 (1988).

109. Ghosh Chaudhuri, R. & Paria, S. Core/Shell Nanoparticles: Classes, Properties, Synthesis Mechanisms, Characterization, and Applications. *Chem. Rev.* **112,** 2373–2433 (2012).

110. Amendola, V., Meneghetti, M., Amendola, V. & Meneghetti, M. Size evaluation of gold nanoparticles by UV-VISs spectroscopy size evaluation of gold nanoparticles by UV-VIS spectroscopy. *J. Phys. Chem. C* **113,** 4277–4285 (2009).

111. Lim, D. C., Dietsche, R., Bubek, M., Ganteför, G. & Kim, Y. D. Oxidation and Reduction of Mass-Selected Au Clusters on SiO2/Si. *ChemPhysChem* **7,** 1909–1911 (2006).

112. Li, T., Senesi, A. J. & Lee, B. Small Angle X-ray Scattering for Nanoparticle Research. *Chem. Rev.* **116,** 11128–11180 (2016).

113. Steven H. Simon. *The Oxford Solid State Basics*. (Oxford University Press, 2013).

114. Guinier, A. *Theorie et technique de la Radiocristallographie (translation to russian)*. (GIFML, 1961).

115. Sinha, S. K., Sirota, E. B., Garoff, S. & Stanley, H. B. X-ray and neutron scattering from rough surfaces. *Phys. Rev. B* **38,** 2297–2311 (1988).

116. Vineyard, G. H. Grazing-incidence diffraction and the distorted-wave approximation for the study of surfaces. *Phys. Rev. B* **26,** 4146–4159 (1982).

117. Renaud, G., Lazzari, R. & Leroy, F. Probing surface and interface morphology with Grazing Incidence Small Angle X-Ray Scattering. *Surf. Sci. Rep.* **64,** 255–380 (2009).

118. Lazzari, R., Leroy, F. & Renaud, G. Grazing-incidence small-angle x-ray scattering from dense packing of islands on surfaces: Development of distorted wave Born approximation and correlation between particle sizes and spacing. *Phys. Rev. B - Condens. Matter Mater. Phys.* **76,** 1–14 (2007).

119. Daillant, J. & Gibaud, A. *X-ray and Neutron Reflectivity*. **770,** (Springer Berlin Heidelberg, 2009).

120. Yoneda, Y. Anomalous Surface Reflection of X Rays. *Phys. Rev.* **131,** 2010–2013 (1963).

121. Schwartzkopf, M. In situ µGISAXS Untersuchungen der Wachstumskinetik von Goldclustern. *Dissertation, Fachbereich Chemie, Universität Hamburg* (Universität Hamburg, 2013).

122. Bruker. X-Ray Fluorescence - The Basic Process. (2018).

123. Pandit, P., Banerjee, M., Pandey, K. K., Sharma, S. M. & Gupta, A. Role of substrate in melting behavior of Langmuir-Blodgett films. *Colloids Surfaces A Physicochem. Eng. Asp.* **471,** 159–163 (2015).

124. Sauerbrey, G. Verwendung von Schwingquarzen zur Waegung duenner Schichten und zur Mikrowaegung. *Zeitschrift fuer Phys.* **155,** 206–222 (1959).

125. Ehrke, H.-U. Monumerische Metallcluster:Erzeugung und Röntgenspektroskopische Messungen. (Technischen Universitpät München, 2000).

126. Staudt, C., Heinrich, R. & Wucher, A. Formation of large clusters during sputtering of silver. *Nucl. Instruments Methods Phys. Res. Sect. B Beam Interact. with Mater. Atoms* **164,** 677–686 (2000).

127. Campana, J. E. Cluster ions. I. Methods. *Mass Spectrom. Rev.* **6,** 395–442 (1987).

128. Wucher, A., Wahl, M. & Oechsner, H. The mass distribution of sputtered metal clusters. I. Experiment. *Nucl. Inst. Methods Phys. Res. B* **83,** 73–78 (1993).

129. Beeck, T. Small, Size-Selected and Deposited Clusters on Magnetic and Non-Magnetic 3d Transition Metal Surfaces. (Hamburg University, 2015).

130. Cheng, H.-P. & Landman, U. Controlled Deposition And Glassification Of Copper Nanoclusters. *J. Phys. Chem.* **98,** 3527–3537 (1994).

131. Cheng, H.-P. & Landman, U. Controlled Deposition, Soft Landing, and Glass Formation in Nanocluster-Surface Collisions. *Science (80-.).* **260,** 1304–1307 (1993).

132. Chekrygina, D. *et al.* Towards the geometric structure of small supported Au9 clusters on Si. *Sci. Rep.* **8,** 12371 (2018).

133. Martins, M., Reif, M., Glaser, L. & Wurth, W. Magnetic properties of deposited gadolinium atoms, dimers and their monoxides. *Eur. Phys. J. D* **45,** 539–546 (2007).

134. Buffet, A. *et al.* P03, the microfocus and nanofocus X-ray scattering (MiNaXS) beamline of the PETRA III storage ring: The microfocus endstation. *J. Synchrotron Radiat.* **19,** 647–653 (2012).

135. Snigirev, A., Kohn, V., Snigireva, I., Souvorov, A. & Lengeler, B. Focusing high-energy x rays by compound refractive lenses. *Appl. Opt.* **37,** 653 (1998).

136. Döhrmann, R. *et al.* A new highly automated sputter equipment for in situ investigation of deposition processes with synchrotron radiation. *Rev. Sci. Instrum.* **84,** (2013).

137. Broennimann, C. *et al.* The PILATUS 1M detector. *J. Synchrotron Radiat.* **13,** 120–130 (2006).

138. HITACHI. Vortex-EM. Available at: https://www.hitachi-hightech.com/hhs-us/product_detail/?pn=ana-vortex-em.

139. Benecke, G. *et al.* A customizable software for fast reduction and analysis of large X-ray scattering data sets: applications of the new DPDAK package to small-angle X-ray scattering and grazing-incidence small-angle X-ray scattering. *J. Appl. Crystallogr.* **47,** 1797–1803 (2014).

140. Lazzari, Â. IsGISAXS : a program for grazing-incidence small- angle X-ray scattering analysis of supported islands research papers. *Interfaces (Providence).* 406–421 (2002). doi:10.1107/S0021889802006088

141. Zhang, X. *et al.* Radiation damage in nanostructured materials. *Prog. Mater. Sci.* **96,** 217–321 (2018).

142. Pearson, K. On lines and planes of closest fit to systems of points in space. *Philos. Mag. Ser. 6* **2,** 559–572 (1901).

143. Jolliffe, I. T. & Cadima, J. Principal component analysis: a review and recent developments. *Philos. Trans. R. Soc. A Math. Phys. Eng. Sci.* **374,** 20150202 (2016).

144. Jolliffe, I. T. Principal Component Analysis, Second Edition. *Encycl. Stat. Behav. Sci.* **30,** 487 (2002).

145. University, S. Machine learning. Available at: https://www.coursera.org/learn/machine-learning.

146. Wes McKinney. Data Structures for Statistical Computing in Python. in *Proceedings of the 9th Python in Science Conference* 51–56 (2010).

147. pandas: powerful Python data analysis toolkit. Available at: https://pandas.pydata.org/pandas-docs/stable/index.html.

148. Fabian Pedregosa, Gaël Varoquaux, Alexandre Gramfort, Vincent Michel, Bertrand Thirion, Olivier Grisel, Mathieu Blondel, Peter Prettenhofer, Ron Weiss, Vincent Dubourg, Jake Vanderplas, Alexandre Passos, David Cournapeau, Matthieu Brucher, Matthieu Perrot, É. D., Pedregosa, F., Weiss, R. & Brucher, M. Scikit-learn: Machine Learning in Python. *J. Mach. Learn. Res.* **12,** 2825–2830 (2011).

149. scikit-learn. Available at: http://scikit-learn.org/stable/about.html.

150. Smelova, E. M., Klavsyuk, A. L., Tsysar', K. M. & Saletskii, A. M. Investigation of the mechanical and electronic properties of Ag-Au and Co-Au nanocontacts by the method of first-principle molecular dynamics. *Moscow Univ. Phys. Bull.* **68,** 92–93 (2013).

151. Liz-Marzán, L. M. Tailoring Surface Plasmons through the Morphology and Assembly of Metal Nanoparticles. *Langmuir* **22,** 32–41 (2006).

152. Yu, S. *et al.* Following the island growth in real time: Ag nanocluster layer on Alq3 thin film. *J. Phys.*

Chem. C **119,** 4406–4413 (2015).

153. B.L. Henke, E.M. Gullikson, and J. C. D. X-ray interactions: photoabsorption, scattering, transmission, and reflection at E=50-30000 eV, Z=1-92. in *Atomic Data and Nuclear Data Tables Vol. 54 (no.2)* 181–342 (1993).

154. Revenant, C., Leroy, F., Lazzari, R., Renaud, G. & Henry, C. R. Quantitative analysis of grazing incidence small-angle x-ray scattering: Pd/MgO(001) growth. *Phys. Rev. B - Condens. Matter Mater. Phys.* **69,** 1–17 (2004).

155. Thompson Albert, Attwood David, GUllikson Eric, Howells Malcolm, Kim Kwang-Je, Kirz Janos, Kortright Jeffrey, LIndau Ingolf, Liu Yanwei, Pianetta Piero, Robinson James, Underwood James , Williams Gwyn, W. H. *X-ray data booklet. Lawrence Berkeley National Laboratory* **8,** (2009).

156. Levine, J. R., Cohen, J. B. & Chung, Y. W. Thin film island growth kinetics: a grazing incidence small angle X-ray scattering study of gold on glass. *Surf. Sci.* **248,** 215–224 (1991).

157. Jia, C.-J., Liu, Y., Bongard, H. & Schüth, F. Very Low Temperature CO Oxidation over Colloidally Deposited Gold Nanoparticles on Mg(OH) 2 and MgO. *J. Am. Chem. Soc.* **132,** 1520–1522 (2010).

158. Babenkov, S. V. *et al.* A new dynamic-XPS end-station for beamline P04 at PETRA III/DESY. *Nucl. Instruments Methods Phys. Res. Sect. A Accel. Spectrometers, Detect. Assoc. Equip.* **777,** 189–193 (2015).

159. Lim, D. C., Dietsche, R., Ganteför, G. & Kim, Y. D. Size-selected Au clusters deposited on SiO2/Si: Stability of clusters under ambient pressure and elevated temperatures. *Appl. Surf. Sci.* **256,** 1148–1151 (2009).

160. Brett, C. Sputter Deposition of Gold on Polymer Thin Films 1 Kurzfassung. (University of Hamburg, 2014).

161. Yu, S. *et al.* Formation of Al Nanostructures on Alq3: An in Situ Grazing Incidence Small Angle X-ray Scattering Study during Radio Frequency Sputter Deposition. *J. Phys. Chem. Lett.* **4,** 3170–3175 (2013).

162. Lim, D. C., Dietsche, R., Ganteför, G. & Kim, Y. D. Oxidation of deposited Aun (n = 2-13) on SiO2/Si: Influence of the NaOH(aq) treatment. *Chem. Phys.* **359,** 161–165 (2009).

163. Lim, D.-C., Hwang, C.-C., Ganteför, G. & Kim, Y. D. Model catalysts of supported Au nanoparticles and mass-selected clusters. *Phys. Chem. Chem. Phys.* **12,** 15172–80 (2010).

164. Inficon. https://www.inficon.com/de/. (2018). Available at: https://www.inficon.com/de/.

165. Begum, P., Bhattacharjee, D., Mishra, B. K. & Deka, R. C. Density functional study on structures, stabilities, and electronic properties of size-selected Pd n Si q (n = 1–7 and q = 0, +1, −1) clusters. *Theor. Chem. Acc.* **133,** 1418 (2013).

166. Langford, J. I. & Wilson, A. J. C. Scherrer after sixty years: A survey and some new results in the determination of crystallite size. *J. Appl. Crystallogr.* **11,** 102–113 (1978).

167. Vinila, V. S., Jacob, R., Mony, A., Nair, H. G. & Issac, S. XRD Studies on Nano Crystalline Ceramic Superconductor PbSrCaCuO at Different Treating Temperatures. *Cryst. Struct. Theory Appl.* **3,** 1–9 (2014).

168. Stierle, A. & Vlieg, E. Surface-Sensitive X-Ray Diffraction Methods. in *Modern Diffraction Methods* 221–257 (Wiley-VCH Verlag GmbH & Co. KGaA, 2013). doi:10.1002/9783527649884.ch8

169. Deutsch, M. & Ocko, B. M. X-ray and Neutron Reflectivity. in *digital Encyclopedia of Applied Physics* (WILEY-VCH Verlag GmbH & Co KGaA, 2003). doi:10.1002/3527600434.eap571

170. Björck, M. & Andersson, G. GenX : an extensible X-ray reflectivity refinement program utilizing differential evolution. *J. Appl. Crystallogr.* **40,** 1174–1178 (2007).

171. Stierle, A., Keller, T. F., Noei, H., Vonk, V. & Roehlsberger, R. DESY NanoLab. *J. large-scale Res. Facil. JLSRF* **2,** A76 (2016).

Eidesstattliche Versicherung / Declaration on oath

Hiermit versichere ich an Eides statt, die vorliegende Dissertationsschrift selbst verfasst und keine anderen als die angegebenen Hilfsmittel und Quellen benutzt zu haben.

Die eingereichte schriftliche Fassung entspricht der auf dem elektronischen Speichermedium.

Die Dissertation wurde in der vorgelegten oder einer ähnlichen Form nicht schon einmal in einem früheren Promotionsverfahren angenommen oder als ungenügend beurteilt.

Hamburg, den _____

Unterschrift der Doktorandin / des Doktoranden